LBL-5305
c.1

DETERMINATION OF THE AXIAL-VECTOR FORM FACTOR IN THE RADIATIVE DECAY OF THE PION

Douglas Alan Ortendahl
(Ph. D. thesis)

December 1976

Prepared for the U. S. Energy Research and
Development Administration under Contract W-7405-ENG-48

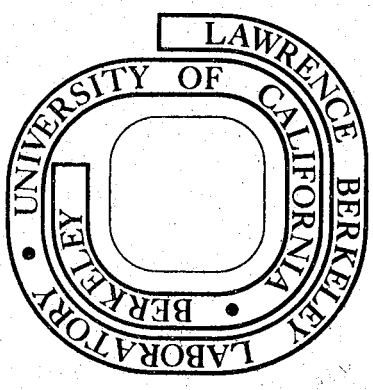

LBL-5305
c.1

Determination of the Axial-Vector Form Factor in the Radiative Decay of the Pion

Douglas Alan Ortendahl

Lawrence Berkeley Laboratory
University of California
Berkeley, CA 94720

Abstract

The branching ratio for the decay $\pi \to e\nu\gamma$ has been measured in a counter experiment in which the e^+ was detected in a magnetic spectrometer and the γ-ray in a lead glass hodoscope. The number of observed events is 226.2 ± 22.4. The branching ratio into the phase space with electron momentum above 56 Mev/c and the electron/photon opening angle greater than 132° is found to be $(5.6 \pm 0.7) \times 10^{-8}$. From the measured branching ratio we determine γ, the ratio of the axial vector to vector form factor. The vector form factor is computed using CVC and the π° lifetime. For $T_\pi{}^\circ = 0.828 \times 10^{-16}$ sec, $\gamma = 0.44 \pm 0.12$ or $\gamma = -2.36 \pm 0.12$ is obtained. A comparison between the measured values of γ, and various theories is made.

TABLE OF CONTENTS

I. INTRODUCTION

The radiative decay of the pion $\pi \to e\nu\gamma$ has been of interest for a long time. It first drew attention 20 years ago when Steinberger reported the most sensitive measurement to that time on the rare decay modes of the pion.[1] He was searching for evidence of the decays $\pi \to e\nu$ and $\pi \to e\nu\gamma$. Finding no examples of either he was able to place upper limits for the branching ratios of 5×10^{-5} for the decay $\pi \to e\nu$ and 2×10^{-5} for the decay $\pi \to e\nu\gamma$. The results of this measurement caused considerable difficulty for theorists working in the days before V-A theory. Using the Universal Fermi interaction they calculated that the branching ratio for the electron mode should be about 10^{-4}, in agreement with present day V-A theory but not Steinberger's experiment. They were able to get reasonable agreement with Steinberger's results by putting in a little pseudoscalar coupling which provided some cancellation.

Radiative decay, however, caused them real problems.[2] Conservation of angular momentum precludes a tensor contribution to the decays $\pi \to \mu\nu$, $\pi \to e\nu$, but such a contribution is not forbidden for radiative decay because of the presence of the photon. If they assumed that the Gamow-Teller contribution to beta-decay was a tensor interaction, then they found that the tensor coupling constant was fairly large. Using this value in their calculations for radiative decay, they found branching ratios of the order of 0.02, in gross disagreement with experiment. The amount of pseudoscalar coupling was fixed by the electron mode and they were unable to produce cancellation by other

couplings. The problem remained until V-A theory explained the Gamow-Teller transition without a tensor interaction, and a correct measurement of the $\pi \to e\nu$ branching ratio was performed. It was then realized that radiative decay was indeed a very rare process.

Radiative decay became of interest again in the late 1950's when it was shown that the amplitude could be expressed in terms of two form factors for the vector and axial-vector currents.[3] More importantly, the new Conserved Vector Current theory[4] allowed the calculation of the vector form factor from the "known" value of the π^o lifetime.[5] "Known" is in quotes because the π^o lifetime has changed considerably over the years and the uncertainty in T_{π^o} is still an important contribution to the error on the determination of the axial vector form factor. At the same time calculations were made relating the branching ratio for radiative decay to the mass of the intermediate vector boson.[6] These models were rather unsatisfactory since they introduced a third form factor while only one was determined independently, namely the vector form factor from CVC.

Radiative decay was first measured at CERN by Depommier et al.[7] as a means of studying the mass of the W-boson. The results on the mass of the W were inconclusive, but they did obtain 140 events and a determination of the axial vector form factor. Since it was soon learned that the mass of the W must be very large, the emphasis has now shifted to determining the axial vector form factor in the decay.

Since Gell-Mann first proposed that the SU(3) octet of axial vector currents should obey the same equal time commutation relations

as the octet of vector currents,[8] the tools of current algebra have become an important means of studying the interactions of elementary particles. Subsequently, Adler used these methods to show that a value for the axial vector coupling constant for neutron beta decay could be derived (in excellent agreement with experiment) by assuming the axial vector current is conserved in the limit that the pion mass is considered small. This assumption is known as Partial Conservation of Axial Vector Currents (PCAC).[9] If chiral symmetry was exact then one would expect an octet of 1^+ mesons with the same mass as the 1^- mesons. Such an octet does not exist, but since current algebra works, the symmetry must be only partially broken. Using this idea Weinberg derived sum rules which related the properties of the ρ to its supposed chiral partner, the A_1.[10] He found that $\frac{M_{A_1}}{M_\rho} = \sqrt{2}$ which was in extraordinary agreement with the then measured value of $\frac{M_{A_1}}{M_\rho}$ $= 1.41 \pm 0.01$. The present day measured value is $1.40 \pm .04$.[11]

This success led to the study of the ρ, A_1, π system. Using the above techniques, it was found that radiative decay of the pion could be related to the masses and widths of the ρ and A_1. The form of the matrix elements for radiative decay was similar to those in the decays $\rho \to \pi\pi$ and $A_1 \to \rho\pi$. In particular, the axial vector form factor could be related to the masses of the ρ and A_1, to the $\pi^+ - \pi^0$ mass difference, and to the charged radius of the pion. Several different predictions for the axial vector form factor were obtained which could be checked with experiment.

There have also been many developments in quark theory since Gell-Mann first proposed the "eight-fold way."[12] As far as radiative decay is concerned there have been predictions for the axial vector form factor from both the non-relativistic and relativistic quark models. The static non-relativistic model makes the very interesting prediction that the axial vector coupling should exactly vanish.[13]

Since the original experiment there has been only one attempt to measure radiative decay and it produced only 11 events.[14] In view of this and the theoretical predictions, it was decided that another measurement of radiative decay would be valuable.

II. THEORY

1. Matrix elements

The matrix elements for radiative decay have been discussed by many authors.[15] Here we will briefly follow the discussion of reference 16, with the mathematical details relegated to Appendix A.1. It is possible to express the radiative decay amplitude in terms of the five Feynman diagrams shown in Fig. 1. The momenta are defined by:

$$\pi(p) \rightarrow e(q) + \nu(Q) + \gamma(k) \tag{1}$$

Diagrams (1a) and (1b) represent the bremsstrahlung terms. They may be calculated by a straightforward application of quantum electrodynamics to the π eν vertex. The expressions involve only known quantities and in this sense nothing new is learned. It should be noted that since the weak vertex is simply the one for $\pi \rightarrow e\nu$ decay, only the axial vector part of the weak hadronic current will contribute to the amplitude.

The presence of the photon allows the strong interaction to generate a new set of intermediate states not present in the ordinary decay $\pi \rightarrow e\nu$ which will allow both vector and axial vector weak hadronic currents to contribute. We are not privileged to know these states explicitly but can express them in terms of form factors. Diagram (1c) is then expressed in terms of $\underline{a}$, the vector form factor and (1d) in terms of $\underline{b}$, the axial vector form factor. These form factors are functions of the momentum transfer $s = -(p - k)^2$. Diagram (1e) is a contact term which arises from the requirement that the total

axial vector part of the amplitude be gauge invariant and is expressed in terms of known quantities.

Because the contact term is not a function of the form factors, it is customary in the literature to include it with diagrams (1a) and (1b) and call the resultant expression inner bremsstrahlung (IB). Diagrams (1c) and (1d) are then considered to be the structure dependent (SD) terms.

The T-matrix element between the initial state i and the final state f is given by

$$T_{fi} = i < f \mid \int L(x)\, d^4x \mid i >$$

where L(x) is the Lagrangian density. For convenience we introduce the reduced T-matrix element $\tilde{T}$ defined by

$$T_{fi} = (2\pi)^4\, i\, \delta^4 (P_i - P_f)\ \tilde{T}_{fi}$$

where P_i and P_f are the 4-momenta of the initial and final states respectively. The reduced T-matrix element for radiative decay can be written

$$\tilde{T} = \tilde{T}_{IB} + \tilde{T}_{SD} \qquad (2)$$

$$T_{IB} = \frac{eG}{\sqrt{2}} \left(\frac{1}{2\pi}\right)^6 \left(\frac{M_e M_\nu}{4k_o q_o Q_o p_o}\right)^{1/2} M_e f_\pi F_{\lambda\nu}(k)$$

$$\times\ \bar{\mu}(q) \left[\frac{\sigma_{\lambda\nu}}{4(q - k)} - \frac{i\, q_\lambda\, p_\nu}{(k - q)\ (k - p)}\right]$$

$$\times\ (1 + \gamma_5)\ \nu(Q) \qquad (3)$$

$$\tilde{T}_{SD} = \frac{eG \cos\phi}{\sqrt{2}} \left(\frac{1}{2\pi}\right)^6 \left(\frac{M_e M_\nu}{4k_o q_o Q_o p_o}\right)^{1/2}$$
$$\times \left[\underline{a}(s)\, \tilde{F}_{\lambda\rho}(k) + \underline{b}(s)\, F_{\lambda\rho}(k)\right] p_\rho$$
$$\times \bar{\mu}(q)\, \gamma_\lambda (1 + \gamma_5)\, \nu(Q) \qquad (4)$$

where e is the charge of the proton, G is the weak interaction coupling constant, the subscript o refers to the time component of the appropriate 4-vector, $\mu(q)$ and $\nu(Q)$ are the electron and neutrino spinors respectively, m_e is the mass of the electron, m_ν is the mass of the neutrino, f_π is the pion decay constant, ϕ is the Cabibbo angle, $F_{\lambda\rho}(k) = \varepsilon_\lambda(k) k_\rho - \varepsilon_\rho(k) k_\lambda$, $\tilde{F}_{\lambda\rho}(k) = \frac{1}{2}\varepsilon_{\lambda\rho\alpha\beta} F_{\alpha\beta}(k)$, and $\varepsilon_\lambda(k)$ is the polarization of the photon. The mass of the neutrino will cancel at a later stage in the calculation of the transition rate. The pion decay contant f_π is defined by the relation

$$(2\pi)^{3/2} (2p_o)^{1/2} \langle 0 \mid J_\lambda^o \mid \pi^-(p) \rangle$$
$$= (2\pi)^{3/2} (2p_o)^{1/2} \langle 0 \mid A_\lambda^o \mid \bar{\pi}(p) \rangle = i f_\pi p_\lambda .$$

If we use meson dominance and assume that $\underline{a}$ is dominated by a ρ pole and $\underline{b}$ by an A_1 pole (see sections II.3 and II.4), then $\underline{a}(s)$ is proportional to $1/(s - m_\rho^2)$ and $\underline{b}(s)$ is proportional to $1/(s - m_{A_1}^2)$. Since the momentum transfer is small ($s < m_\pi^2$), it is a good approximation to take the form factors to be constant, evaluated at $s = 0$. It is customary to express the SD amplitude in terms of $\underline{a}(0)$ and $\gamma \equiv \underline{b}(0)/\underline{a}(0)$. We emphasize that the quantity of interest here is $\underline{b}$; γ is introduced

only as a convenience (it avoids the problems of convention in defining the form factors) and to be consistent with the literature.

2. Decay rate

If the pion decays at rest then there are three observables: the electron momentum, p, the photon momentum, k, and the opening angle between the photon and the electron, θ. For a complete kinematic description it is sufficient to measure two of the above observables because they are related by the expression

$$\cos\theta = \frac{1 + 2(1 - (x + y))}{xy} \tag{5}$$

where $x = 2k/m_\pi$ and $y = 2p/m_\pi$. Although p and θ were measured in this experiment, the theoretical rates are most conveniently expressed in terms of p and k.

The transition probability per unit time dW is related to the T-matrix element by

$$dW = (2\pi)^4\ \delta^4\left(p - (q + k + Q)\right) |\ \tilde{T}\ |^2\ \frac{d^3q}{(2\pi)^3}\ \frac{d^3k}{(2\pi)^3}\ \frac{d^3Q}{(2\pi)^3}$$

Integrating over the neutrino momentum we find

$$\frac{d^2W}{dxdy} = \frac{d^2W_{IB}}{dxdy} + \frac{d^2W_{SD}}{dxdy} + \frac{d^2W_{INT}}{dxdy} \tag{6}$$

$$\frac{d^2W_{IB}}{dxdy} = \frac{\alpha W_{e\nu}}{2\pi}\ \left(\frac{1 - y}{x^2}\right)\ \left(\frac{(x - 1)^2 + 1}{x + y - 1}\right) \tag{7}$$

$$\frac{d^2W_{SD}}{dxdy} = (G\cos\phi)^2\ \alpha m_\pi^7\ |\ \underline{a}\ (0)\ |^2 \times \left\{D(1 + \gamma)^2 + E(1 - \gamma)^2\right\} \tag{8}$$

$$\frac{d^2W_{INT}}{dxdy} = \frac{2G\ (\cos\phi)\ \alpha\ W_{e\nu}^{1/2}\ M_e\ M_\pi^{9/2}\ |\ \underline{a}\ (0)\ |}{(2\pi)^{1/2}}$$

$$\times \left(\frac{y - 1}{x}\right) \left\{(1 + \gamma)\ (1 - x) + (1 - \gamma)\ (x^2 + x - 1)\right\} \tag{9}$$

where $\alpha = 1/137$, $W_{e\nu}$ = rate of $\pi \to e\nu$, $D = (1 - x)\ (x + y - 1)$, $E = (1 - x)\ (1 - y)^2$ and the rest mass of the electron has been set equal to zero. The interference term, W_{INT}, between the structure dependent and inner bremsstrahlung amplitudes is small with respect to the SD and IB rates and was neglected in subsequent analysis (it contributes only .14% to the branching ratio observed by this experiment). It is important to note that since the expression for the rate is quadratic in γ, there will be two solutions for γ.

3. The vector form factor

In order to determine the axial vector form factor $\underline{b}(0)$, or equivalently γ, we must obtain $\underline{a}(0)$ from some external source. The conserved vector current theory (CVC) allows us to relate the strangeness conserving weak vector hadronic current to the isovector part of the electromagnetic current as an isotriplet vector. It has been shown that this can be used to determine the vector part of $\pi \to e\nu\gamma$ from $\pi \to \gamma\gamma$ where one of the photons is replaced by a lepton pair.[17] We obtain

$$|\ \underline{a}(0)\ | = \frac{2}{\left(\pi M_\pi^3\ T_{\pi^0}\right)^{1/2}} = (0.0261 \pm .0009)\ M_\pi^{-1}$$

where T_{π^0} is the π^0 lifetime, $T_{\pi^0} = (0.828 \pm 0.057) \times 10^{-16}$ sec.[18]

The ρ-dominance hypothesis gives another result for $\underline{a}$ which is independent of the π^0 lifetime.[19] We assume the vector part of the amplitude goes by the diagram in Fig. 2. If the ρ-meson is the dominate intermediate state, we find

$$| \underline{a}(s) | = \frac{f_\rho \, f_{\rho\pi\gamma}}{s - m_\rho^2}$$

where f_ρ is the coupling constant at the ρ-lepton vertex and $f_{\rho\pi\gamma}$ is the coupling constant at the other vertex. We obtain

$$| \underline{a}(0) | = (0.035 \pm 0.0025) \, m_\pi^{-1}$$

where the value of f_ρ is obtained from the KSRF relation[20] and $f_{\rho\pi\gamma}$ is determined from the decay $\omega^0 \to \pi^0 \gamma$ using SU(3) symmetry. Another estimate for the product $f_\rho \; f_{\rho\pi\gamma}$ may be obtained by assuming that the vector ultra-violet divergences of the radiative corrections to pion beta decay are cancelled by the corresponding axial divergences.[21] This leads to a sum rule which when saturated by the ρ-meson gives $f_\rho \, f_{\rho\pi\gamma} = -f_\pi$, which in turn yields $| \underline{a}(0) | = .0313 \, m_\pi^{-1}$ (no error quoted). Neither result agrees with the CVC value. Because of the success of the CVC theory over a number of years (pion beta decay is but one example) we shall use the value of $| \underline{a}(0) |$ determined by CVC unless otherwise stated.

Neither CVC nor ρ-dominance predicts the sign of $\underline{a}$. However, $\underline{a}$ can be shown to be positive if one assumes that the process can be described by a quark triangle diagram.[22]

4. The axial vector form factor

The more interesting case is the calculation of b. Both current algebra and the quark model give predictions for b. The current algebra models are similar to the ρ-dominance model used to calculate a, but the situation is complicated by the probable need of a subtraction in the dispersion relations which yields another constant to be determined. Both the non-relativistic and relativistic quark models offer values for b. The predictions of these models as presented in this section and summarized in Table I will be compared with the experimental results in the concluding section.

One approach is to follow the meson-dominance calculation of a with the ρ replaced by its chiral partner, the A_1. If we assume an unsubtracted dispersion relation we find $b(0) = \frac{2f_\pi}{M_{A_1}^2} = \frac{f_\pi}{M_\rho^2}$ using $M_{A_1}^2 = \sqrt{2}\, M_\rho^2$.[10] This gives $|\gamma| = 1.2$. However, if unsubtracted dispersion relations are used to calculate the matrix elements for A_1 and ρ decay,[23] $\langle \pi^o | V_\mu | A_1^- \rangle$ and $\langle \pi^o | A_\mu | \rho^- \rangle$ (V_μ and A_μ are vector and axial vector currents respectively), one finds $\Gamma(\rho \to \pi\pi) = 36$ MeV and $\Gamma(A_1 \to \rho\pi) = 605$ MeV in gross disagreement with the experimental values of 152 Mev and 300 Mev respectively.[18]

Schnitzer and Weinberg[24] have used current algebra and Ward identities to do a "hard-pion" evaluation of the 3-point functions which appear in their matrix elements. They introduce a subtraction constant δ which can be related to the widths of the ρ and A_1 and the

charge radius of the π. Using these techniques one finds

$$\underline{b}(0) = \frac{-\delta f_\pi}{2M_\rho^2} \quad .$$ [25]

Using current algebra and soft-pion techniques, Das, Mathur, and Okubo have found

$$\underline{b}(0) = \frac{-f_\pi}{2M_\rho^2} \quad .$$ [26]

Brown and West[27] have shown that soft-pion techniques are equivalent to the hard-pion techniques of Schnitzer and Weinberg if one takes care to include the singularities in all variables. The results of these calculations are summarized in Table I. The value $\delta = -1$ corresponds to no subtraction in the pion form factor F_+. The results of references 25 and 26 are identical if one notices that Das et al. assume an unsubtracted dispersion relation for F_+. The value $\delta = -1/2$ comes from a fit to the experimental widths of the ρ and A_1 which at that time were $\Gamma(\rho) = 128$ Mev and $\Gamma(A_1) = 30$ Mev. Inasmuch as the presently accepted values are considerably different, it has no special significance today. The choice $\delta = 0$ has the merit that, in the soft-pion limit, the logarithmic divergence from the A_1 contribution to the $\pi^+ - \pi^0$ mass difference cancels out.[28] $\delta = -3.6$ [29] results from using the experimental value[30] of the charge radius of the π^+, $r_\pi = (.80 \pm .1)$f to fix the subtraction constant. Another current algebra approach has been taken by Gregor.[22] He has developed a phenomenological Lagrangian for the π, A_1 and ρ mesons with minimally broken chiral symmetry. The results are expressed in terms of five free parameters which are determined by

Table I. Values of γ predicted by various theories and the relationship to other physical parameters.

$\lvert\gamma\rvert$	δ	Γ $(A_1 \to \rho\pi)$ (Mev)	Γ $(\rho \to \pi\pi)$ (Mev)	Pion charge radius (Fermi)	Reference
Experimental Values		300	152 ± 3	.8 ± .1	18,30
0.59[a]	-1	61	140	0.63	26
0.35[a]	-1/2	116	107	0.59	25
0.[a]	0	190	79	0.55	28
1.2[b]	NA	605	36	NA	16
.65[c]	NA	79	146	0.67	22
0.[d]	NA	NA	NA	NA	13,37
1.[e]	NA	NA	NA	NA	37
.4[f]	NA	NA	NA	NA	37
2.14[g]	-3.6	80	3.2	.8	29

NA-The model in question does not offer a prediction for this quantity.

a-Current algebra, subtracted dispersion relation.

b-Current algebra, unsubtracted dispersion relation.

c-Current algebra, phenomenological Lagrangian, sign is positive.

d-Static quark model and Gell-Mann-Levy sigma model.

e-Relativistic quark model (Gell-Mann-Zweig, Han-Nambu, and colored quark models).

f-Relativistic quark model (nucleon-antinucleon model).

g-Current algebra, subtracted dispersion relation, based on the experimental value of the pion charge radius.

$$M_\rho,\ M_{A_1},\ \Gamma\ (\rho \to \pi\pi),\ \Gamma\ (\rho \to e^+e^-) \text{ and } f_\pi.$$

He finds $\gamma = +0.65$. The sign of γ is taken to be positive from the quark triangle diagram calculations.

There is considerable controversy about whether the A_1 is a bona fide resonance.[31] It is argued that the A_1 is a dynamical enhancement, the "Deck effect."[32] In particular, no phase variation is observed for the scattering amplitude.[33] However, it has been recently shown that this absence of phase variation is an automatic consequence of a simple dynamical model which predicts an A_1 resonance pole at 1160 MeV with $\Gamma = 180$ MeV.[34]

An alternative method to study the axial vector form factor is provided by the quark model. The positive pion is considered as a bound state of a p-quark and a n-quark, and one must calculate the so-called quark triangle diagrams. In the non-relativistic quark model it is found that the axial vector contribution yields the bremsstrahlung contributions of Fig. 1a and 1b and the contact term of Fig. 1e; all other contributions vanish, i.e., $\gamma = 0$.[13] This result is independent of the free parameters that often appear in quark models and may be taken as a "theorem" of the static quark model or SU(6). Scheck and Wullschleger[35] criticize the unrealistic aspects of this model: in particular the assumption that the binding is weak. This means that quarks and antiquarks in intermediate states between the vertices should not interact, which implies that such quark-antiquark states as π, ρ, and A_1 should have the same mass.

The static quark model also contradicts the Adler theorem (triangle anomaly)[36] which says that for π^0 decay and radiative decay in the soft-pion limit the vector part of the quark-photon coupling is given completely by γ_μ and not by an anomalous magnetic coupling as required by the static model.

A different result is obtained from a relativistic quark model of Moreno and Pestieau.[37] Here one is not restricted to the infinite quark mass of the static model and the quark mass is a parameter in the calculation. Unlike the previous models we have discussed this is an explicit calculation of γ not just the axial vector form factor b. In the infinite quark mass limit both the vector and axial vector form factors vanish, but their ratio remains finite. For an infinite quark mass the Gell-Mann-Zweig, the Han-Nambu and the colored quark models predict $\gamma = -1$ with γ rising to -.55 at the minimum acceptable quark mass of $M_\pi/2$. The nucleon-antinucleon model gives $\gamma = -.4$ for $M = \infty$ and $\gamma = -.27$ for $M = M_\pi/2$. The main flaw in this model is that it does not fulfill the requirements of current algebra and does not contain PCAC as an operator identity. Moreno and Pestieau have also studied this process using the σ-model of Gell-Mann and Levy,[38] which satisfies renormalizability, current algebra and PCAC. With this model they find $\gamma = 0$ in the soft-pion limit.

III. EXPERIMENTAL DESIGN

1. General method

The experimental layout is shown in Fig. 3. A beam of π^+'s was stopped in the central hodoscope of scintillation counters, S_{1-6}. The positron was detected by scintillators E_{1-3}, and its momentum measured by the magnet-spark chamber spectrometer.

The position of the photon was determined by the lead-glass Cherenkov counter hodoscope to obtain the opening angle θ. The configuration of the spectrometer and the orientation of the lead-glass counter were motivated by the desire to maximize the sensitivity to γ by working in a kinematic region where the structure dependent term was large with respect to the inner bremsstrahlung contribution and the background was low. Figures 4a and 4b show the decay rates of the bremsstrahlung term and the structure dependent term (for different values of γ) as a function of positron momentum and opening angle. It can be seen that for $\gamma = 0$ or 1 the structure dependent term peaks at high positron momentum and large opening angle, while the bremsstrahlung term peaks at high momentum but drops sharply as the opening angle increases. The apparatus was designed to detect with maximum efficiency events with positron momentum above 56 Mev/c and opening angle greater than 120°. This momentum region also avoids the overwhelming background of positrons from muon decay. Since the photon energy was not measured there was no redundant kinematic information. The background was identified by relying on the fact that for radiative decay, pulses in the photon and positron counters are in time coincidence.

2. Beam

The pions were obtained from an auxillary pion channel of the LBL 184" synchrocyclotron. The 735 MeV external proton beam was incident on a copper target. The pions were taken off at 90^{o} with a momentum 120 ± 10 Mev/c. The particle flux was about 10^{6}/sec with a composition of 60% e^{+}, 35% π^{+}, and 5% μ^{+}.

3. Magnet spectrometer

The magnet was a large C-magnet with a 24" gap and pole pieces 24" × 36". A 2" thick steel shield, with a window to allow positrons to enter the magnet, was used to provide a flux return path, reduce the stray field in the region of the stopping hodoscope and the photon counter, and improve the field uniformity inside the magnet. The nominal field strength was 3000 gauss.

Four magnetostrictive spark chambers[39] were used. Chambers 1 and 2 each had a single gap with an active area 7" × 15"; chambers 3 and 4 had an area of 15" × 24" with two gaps. The orientation of the magnetostrictive delay lines (referred to as wands), the high voltage polarity to each gap, and the polarity of the pulses to the chamber fiducials were carefully selected to allow the chambers to operate successfully in the high magnetic field.

4. Photon hodoscope

The photon counter was a Cherenkov hodoscope of 24 6-inch cubes of lead glass each with its own 5" photomultiplier tube. The cubes were arranged in a closed-packed array 4 blocks high by 6 blocks wide. The thickness of each block was 5.18 radiation lengths. The counter subtended a solid angle of 2.2 steradians, measured from the center of the stopping hodoscope. A complete description of the construction, operation and calibration of this counter will be found in Appendix B.

5. Counters and electronics

The beam was monitored by 3 plastic scintillators B_{1-3}. The stopping hodoscope consisted of 6 scintillators S_{1-6}, each 1/4" × 2" × 7". The hodoscope was slanted in order to increase the thickness relative to the beam and to minimize the energy loss of the outgoing positron. Immediately behind the hodoscope was counter A_1 which acted as veto for non-stopping particles. For optical isolation and to minimize the material between the counters, the individual S counters and A_1 were wrapped in a single layer of 1/4 mil aluminized mylar. Counter A_2 was added to correct for a 2% leakage of particles passing through S_6 but missing A_1. The positron was detected by 3 scintillators E_{1-3}. E_3 was designed to detect particles traversing E_1 near the downstream edge but missing E_2. The size of counter E_1 provided a solid angle of .53 steradians for positrons generated at the center of the stopping hodoscope. Scintillators V_1 and V_2 acted as vetos for charged particles entering the lead glass counters.

A simplified electronics diagram is shown in Fig. 5. The master trigger which fired the spark chambers and strobed the other electronics required the presence of a stopped pion and pulses in the positron counters and the Cherenkov counter. The stopping signature was $B \cdot S \cdot \bar{A}$ where $B \equiv (B1 \cdot B2 \cdot B3)$, $A \equiv (A_1 \text{ or } A_2)$, and S was any of the 6 stopping counters. A valid stop opened a 150 ns wide gate (ON) which was timed to allow for 120 ns of pion decay and 30 ns of time before the stop for background study. The RF frequency of the cyclotron at extraction was 20 MHz; if a stop was detected in either of the 2 beam buckets following a valid stop the ON gate was updated (extended 150 ns). The update rate was about 6% of the stopping rate. The master trigger signature was $ON \cdot (E_1 \cdot (E_2 \text{ or } E_3)) \cdot (C \cdot \overline{(V_1 \text{ or } V_2)})$ where C and V are the Cherenkov and veto counter signals respectively.

The spark locations were digitized by a scaler which allowed up to 4 sparks per wand. In addition, 13 analog signals were digitized: ET, the time elapsed between the π stop and the event detection; ΔT, the relative time difference between the positron counter pulse and the Cherenkov pulse; gamma sum, the sum of the pulse heights in each of the 24 tubes in the photon counter; and 10 signals corresponding to the pulse heights in each of the 4 rows and 6 columns in the photon hodoscope. Coincidence registers were used to record which stopping element fired and the presence of an ON gate update. The data was written to magnetic tape by a hard-wired data buffer. A typewriter was available to give an octal listing of the data.

All data was taken at maximum cyclotron beam intensity which produced about 2×10^5 stopping π's per second. Over the course of the

experiment 300,000 master triggers were collected, about 400 per hour. The radiative decay event rate turned out to be about 1 event per 1300 master triggers. The data was taken in groups of runs; each run was approximately 3 hours in length.

IV. DATA ANALYSIS AND CORRECTIONS

1. General

In order to extract γ from the data we cast equation (6) in a different form:

$$\frac{d^2N_{RD}}{dpd\theta} = \beta N_\pi \left(\frac{d^2W'_{IB}(p,\theta)}{dpd\theta} + |\underline{a}(0)|^2 \left\{ \frac{d^2F'(p,\theta)}{dpd\theta} (1+\gamma)^2 + \frac{d^2H'(p,\theta)}{dpd\theta} (1-\gamma)^2 \right\} \right) \tag{10}$$

where N_{RD} is the number of radiative decay events observed in the interval dp and $d\theta$, N_π is the number of "stops" (directly from the $B\cdot S\cdot\bar{A}$ scaler),

$$F = \frac{(G\cos\phi)^2 \alpha m_\pi^7}{64\pi^2} D, \quad H = \frac{(G\cos\phi)^2 \alpha m_\pi^7}{64\pi^2} E,$$

and β is a factor which corrects the stopping flux for the various efficiencies in the experiment which are independent of the decay kinematics. There are several contributions to β, $\beta \equiv \beta_f \beta_c \beta_s$ (see Sections IV.6a and IV.6b). The independent variables have been changed from p and k to p and θ. The primes on W_{IB}, F and H indicate that the functions W_{IB}, F and H have been folded with the energy loss of the positron, the photon detection efficiency, the acceptance, and the momentum and angular resolution. We measured p and θ, which was sufficient to uniquely determine radiative decay but did not provide any redundant kinematic information to help separate the events from the background. For this we relied on the fact that for radiative decay

a signal in the positron counter would be correlated in time with a signal in the photon counter. As discussed earlier, the time difference (ΔT) between these two signals was recorded for each event. We expected the ΔT spectrum to contain a peak corresponding to the radiative decay events above a flat background. By extrapolating this background under the peak and subtracting we would easily determine the number of radiative decay events.

The data analysis was done in three stages. The large amount of expected background made this desirable since some of the background could be eliminated at each stage. The first stage, "Data Summary Program," found the positron tracks through the magnet; the second stage, "Winnow Program," reconstructed the radiative decay events and applied other cuts to the data; and the third stage used equation (10) to solve for γ.

2. Data summary program

The data summary program used a general spark chamber data acquisition routine[40] to convert the magnetostrictive wand information into possible spark locations, up to a maximum of 10 sparks per chamber. Chambers 1 and 2 were single gap, hence there was no degeneracy to eliminate spurious combinations of the wand data. This also implies that the determination of the spark location required at least one signal on each of the 2 wands in the chamber. Chambers 3 and 4 were double gap with the wires in the second gap rotated with respect to the first gap to provide a redundant determination of the spark location. This

allowed spurious combinations of the wand data to be eliminated. Data on 3 of the 4 wands in the chamber was sufficient to determine the location of a spark.

A fourth order Adams-Bashforth method[41] was used to integrate the equations of motion through the magnet (called orbiting). Since orbiting was the most time-consuming part of the program, a two-stage process was used to reconstruct particle trajectories from the spark chamber data. A set of polynomials was generated which predicted momentum, x position in chamber 1, the starting position and angle in terms of the x component in 3 of the 4 chambers. The values of these polynomials were used to select those combinations of sparks which were likely candidates for particle trajectories. Those spark combinations passing this first stage were orbited using a least-squares fit to the spark chamber coordinates with a Newton-Raphson iteration scheme to determine the momentum, starting position and direction cosines of the track. The values obtained from the 4 polynomials were used as initial estimates of the parameters. No cut on the χ^2 obtained for the fit was applied at this time. The only way a candidate could fail to be orbited successfully was for the track to cross one of the boundaries set within the program. The boundaries were set larger than the active area of the chambers so that a good track was not rejected because the first few iterations had the track outside one of the chambers. Since there were often multiple interpretations of the spark chamber data the successful candidate was considered a subevent (up to 10 subevents were allowed per master trigger). If the master trigger had any acceptable tracks,

the fixed data associated with the master trigger and all subevents were written to a data summary tape. One third of the master triggers had acceptable positron tracks. More detail on the polynomials and the momentum determination algorithm is provided in Appendix D.

3. Event reconstruction

The second step of data analysis, kinematic reconstruction and signal enhancement by selection, was done by a program "WINNOW" which took its input from the data summary tape. The program KIOWA[42] was used to produce histograms and scatter plots of the data. The position of the photon shower was determined by a straightforward averaging of the energy deposited in each row and column. Usually the shower did not appear perfectly centered in a row or column; rather it looked like a sharing between adjacent rows or columns. Some of this was true sharing of the shower between 2 blocks. It was found for the radiative decay events that 15% of the time at least 10% of the total shower energy was shared between 2 blocks. But much of the apparent sharing was actually due to noise in non-adjacent rows or columns. In order to eliminate some of this noise it was required that the energy deposited in these 2 adjacent rows be $\geqslant$81% of the total row signal and the same for the columns.

Each event had up to 10 possible positron tracks (the subevents); WINNOW chose the one for which the track reconstruction gave the minimum χ^2. For each event the intersection between this positron track and the stopping hodoscope was found, and this point was used as

the vertex of the decay in order to compute the opening angle. In addition to the above cuts on the adjacent row and column energy in the photon counter, several other cuts were applied to the data. The value of χ^2 was required to be less than 4. Because of the high background due to positrons from muon decay a lower limit on the positron momentum was set at 56 Mev/c; the upper limit was 75 MeV/c. For events that were not updated the elapsed time (ET) was required to be greater than zero. However, for updated events elapsed time was not a meaningful quantity and no requirement on ET could be made. Other requirements on the data were: opening angle above 132°, decay vertex within .25 inch of an S counter which fired, and the positron track must have crossed counter E_1. Fig. 6 shows the resultant ΔT spectrum after all these cuts have been made. The number of radiative decay events is calculated by $N_{RDE} = N_{IT} - (R)\ N_{OT}$ where N_{IT} and N_{OT} are the number of in-time and out of time events respectively and R is the ratio of the timing intervals. Fig. 7 shows the number of radiative decay events included as a function of the width of the in-time window. The number of events increases monotonically from $|\ \Delta T\ | = 0$ to $|\ \Delta T\ | = 2$, and levels off at $|\ \Delta T\ | = 2$. The position of the in-time region is chosen to be $|\ \Delta T\ | = 2.5$ ns because this is .2 ns beyond the point at which the number of events obtained actually decreased as the timing interval was increased .1 ns. The behavior of Fig. 7 for large $|\ \Delta T\ |$ is consistent with a statistical fluctuation of a flat background.

After all cuts discussed previously are applied, 226.2 ± 22.4 radiative decay events are found. The error is statistical and is

given by $\sigma = (N_{IT} + (R)\ N_{OT})^{1/2}$. Table IIa shows the effects of the cuts on the data when applied in sequence. Table IIb shows what happens when all cuts but one are applied. Since the efficiency of the cut on χ^2 (see Section IV.6b) indicates that 4 radiative decay events should be expected to have a value of χ^2 greater than 4, the difference, shown in Table IIb, between before and after the χ^2 cut is applied is consistent with zero. The negative difference observed for the ET cut is of no concern since no radiative decay events are lost. The other differences are all consistent with zero.

To get an idea of the quality of the data, the elapsed time spectrum for the in-time events with background subtracted is plotted in Fig. 8a. The smooth curve is the π decay curve fitted to the data. The χ^2 per degree of freedom is .69 with 19 degrees of freedom. Fig. 8b shows the elapsed time distribution of the out-of-time events with the same cuts applied.

We investigated the possibility that the procedure of selecting only the best χ^2 per event might be biased. The data was reanalyzed looking for events with subevents having χ^2 less than 4 and momentum between 58 and 75 MeV/c which had previously been rejected because the subevent with the best χ^2 did not have momentum in this range. We found 76 in-time events and 351 out-of-time events which gave 5.8 ± 12 radiative decay events. The choice of the subevent with the smallest χ^2 is thus justified.

Table IIa. Number of events left after each cut is applied in sequence.

Cut	In-time Events	Out-of-time Events	Radiative Decay Events
$56<p<75$ Mev/c	629	1435	251.4 ± 31.7
$\chi^2<4$ (for momentum fit)	465	1065	236.7 ± 27.3
Row and Column Energy	495	1012	228.7 ± 27.6
Position in Stopper	403	667	227.5 ± 24.0
Hits E_1	398	640	229.6 ± 23.8
Elapsed Time (ET)	390	588	235.3 ± 23.3
$\theta>132^\circ$	363	520	226.2 ± 22.4

Table IIb. Number of events left if all cuts but one are applied, Δ is the difference in the number of radiative decay events predicted before and after applying the cut.

Cut	In-time Events	Out-of-time Events	Radiative Decay Events	Δ
χ^2	415	682	235.5 ± 24.4	9.4 ± 9.7
Row and Column Energy	371	548	226.8 ± 22.7	0.6 ± 3.9
Position in Stopper	431	767	229.2 ± 25.2	3.0 ± 11.5
Hits E_1	366	539	224.2 ± 22.5	-2.0 ± 2.8
Elapsed Time (ET)	368	569	218.3 ± 22.8	-7.9 ± 4.2

4. Momentum calibration

The momentum scale was fixed and the spectrometer resolution measured by fitting the high energy end of the muon decay spectrum. The theoretical μ-decay spectrum was folded with the energy loss in the S counters assuming that the depth distribution in the stopper was uniform. Thus the energy loss varied from 0 to 1.35 Mev. The observed momentum spectrum was then given by:

$$\frac{dN}{dp}(p) = A\left(\frac{2}{\pi\sigma}\right)^{1/2} \int_0^\infty f(kp')\, e^{-(p - p')^2/2\sigma^2}\, dp'$$

where dN/dp is the observed spectrum, p and p' are the momenta as measured by the spectrometer before calibration, f is the theoretical muon decay spectrum folded with the energy loss in the stopper, A is an overall normalization factor, k is the momentum calibration constant, and σ is the momentum resolution. The observed spectrum was fit to this function with A, k, and σ as free parameters. Fig. 9 shows the results of such a fit. For this particular plot the momentum calibration constant was found to be 1.03 ± 0.009 with σ = 2.25 ± 0.11 Mev/c, with a probability of exceeding the observed χ^2 of $P_\chi(\chi^2, \nu)$ = P_χ (118, 137) = .9 where ν is the number of degrees of freedom. Such a fit was done for each block of data, typically several days worth. In all there were 25 blocks. For the total data sample the momentum calibration constant was found to average 1.016 ± 0.014. However, the momentum was corrected on a block by block basis with a typical error in the calibration constant of 0.01, or 0.5 Mev/c. The analysis program used the overall resolution which was 2.15 ± 0.19 Mev/c.

5. ΔT calibration

For radiative decay events the photon and positron will strike their respective detectors with a relative time difference determined solely by the difference in path length. The signals from all of the Pb-glass blocks were adjusted to be coincident to within 1 ns, but the difference in transit time for hits at different parts of the counter E_1 could be as much as 6 ns. Using a Sr^{90} source the transit time was measured as a function of position in E_1, and this data was fit to a polynomial function for use by the analysis programs.

The γ-rays from π^o decay were used to determine the absolute zero position in the ΔT spectrum. The absorber upstream from B_3 was removed to increase the probability of charge exchange in the stopper. A scintillator to veto charged particles and a 1/16 inch sheet of lead to convert the γ-rays were placed between the S counters and the spark chambers. The ON gate was shortened to 10 ns to reduce the background. 250 π^o events were seen.

6. Detection efficiencies

This is a branching ratio experiment normalized solely by the observed number of stopping pions. It is thus essential to know the various detection efficiencies.

a. Flux normalization

The normalized flux is that fraction of the $B \cdot S \cdot \bar{A} \cdot$ coincidences which represents true pion stops. There are four parts to this question: anti-efficiency, accidentals, multiple pion stops, and muon fraction. The efficiency of the anti-counter for electrons was measured to be 100% with negligible error. Randoms in the S counters could fake a pion stop (there was a high background in the S counters due to muon decay). The effect of these randoms was estimated by scaling several combinations of B,S,A and $\bar{A}$ in delayed coincidence and was found to be negligible in almost all cases and of the order of 1% for a few runs.

It was also possible for more than 1 pion to stop in the same beam bucket. This was determined by measuring the probability of 2 S counters firing in coincidence with a stop signal and correcting for the probability of 2 pions stopping in the same S counter. This effect was also found to be less than 1% in most cases.

Lastly, the fraction of the real particle stops that were in fact muons instead of pions was also determined. The range of a 120 MeV/c muon is $3 gm/cm^2$ longer than that of a 120 MeV/c pi, so muons produced upstream in the channel would not stop. However, pions decaying after traversing the channel could produce muons of the proper momenta to stop. To measure this, the Cherenkov counter in coincidence with V_1 and V_2 was used to detect electrons from muon decay. The number of electrons detected was plotted as a function of elapsed time after the

stop. The resultant spectrum is shown in Fig. 10. The time dependence is characteristic of a parent-daughter decay of the form

$$\begin{array}{l} \pi^+ \rightarrow \mu^+\nu_\mu \\ \qquad \llcorner\!\!\longrightarrow e^+\bar{\nu}_\mu\nu_e \end{array}$$

The peak in the spectrum at ET = 0 was due to beam electrons which scattered from the stopper into the Cherenkov counter.

With the area near the peak omitted, a fit was performed to the function

$$\begin{aligned} N(t) &= A(1 - re^{-t/t_\pi})\, e^{-t/t_\mu} + B \qquad && t > 0 \qquad (11) \\ &= B && t < 0 \end{aligned}$$

with A, B, and r as parameters. The variable r is the fraction of stopping particles that are π's. On the average r was found to be .957 ± .03. The μ/π fraction was quite constant throughout the experiment, and for this reason these muon fraction spectrums were taken infrequently. To monitor the π-flux on a run by run basis, a discriminator was set to count the pulses in the stopping hodoscope produced by the 4.4 Mev muon from $\pi \rightarrow \mu\nu$ decay. The ratio of these π-μ decays to observed stops was used to calculate the μ/π ratio. After correcting for this run by run it was found that $\beta_f \equiv r = 0.958 \pm 0.03$.

It was also necessary to correct for events that were lost due to a random count in the veto counters. This correction was made on a run by run basis by scaling C·V where the veto counter signal was delayed 1 RF period. Averaging over all runs it was found that $\beta_c = .924$.

b. Spark chamber efficiency

The efficiency of the spark chambers was determined by searching for cases where the sparks in 3 chambers gave an acceptable fit to a trajectory, but no acceptable fit was possible when all 4 chambers were required to be part of the fit. Since the bulk of the trajectories were due to positrons from muon decay, these tracks were used for the efficiency determination. Master triggers which did not produce an acceptable 4 chamber fit during the Data Summary stage of the analysis were searched for 3 chamber fits with 1 chamber deleted. Because of the large amount of track bending between chambers 3 and 4, it was possible to obtain reasonable fits only by deleting chambers 1, 2, or 3. The order in which the chambers were deleted was chosen by random number generator to avoid any possible bias due to the deletion sequence. Once an acceptable track was found the process was terminated. This procedure tested both the mechanical efficiency of the spark chambers (the presence of a spark) and the reconstruction efficiency (the efficiency of the polynomial cuts). Acceptable 3 chamber fits were required to have a value of χ^2 less than 20 while 4 chamber fits were required to have χ^2 less than 4 (the same value as the cut in the WINNOW program). The results were insensitive to the choice of the value for the cut on χ^2 for the 3 chamber fits once the cut was above $\chi^2 = 4$.

Thirty master triggers were sampled in every fourth run. This produced a total of 780 trajectories. The efficiencies for chambers 1-3 respectively were found to be .90 ± .01, .89 ± .01, .962 ± .006.

It was found that about two-thirds of the inefficiency was due to the absence of a spark. The efficiency of chambers 1 and 2 was unusually low because the discriminators for the magnetostrictive wands had a tendency to multiple pulse. Since the wand scalers allowed only 4 sparks per wand, a wand pulse with 3 spurious after pulses would fill up all available scalers. A second real spark, whose signal would be received by the wand discriminator after the first spark (and its associated after pulses), would be missed. Since the rates in chambers 1 and 2 were very high (by being so close to the stopping hodoscope) and the chambers were single gap (requiring information on both wands), this was an important effect. The effect was much less for chambers 3 and 4 since they were less busy and were double gap which meant signals from 3 wands were sufficient to define a spark.

By turning the C magnet off and removing the Cherenkov counter from the master trigger, it was possible to examine straight tracks through the spark chambers. Again by looking at 3 and 4 chamber fits to a straight line it was possible to measure the efficiency of the chambers. The efficiency for straight tracks was .924 ± .01, .958 ± .01, .979 ± .016, .985 ± .006 for chambers 1-4 respectively. This straight tracks procedure tested only the mechanical efficiency of the chambers including the multiple pulsing effect. The reconstruction efficiency was corrected for by checking the 3 chamber fits for correlated sparks in the missing chamber. Realizing that about one-third of the efficiency observed for the magnet on data was due to reconstruction efficiency, it is seen that the magnetic field had only a small effect

on chambers 1 and 3. The effect for chamber 2 occurred because with the magnet off chamber 2 was not as sensitive to the multiple pulsing problem as was chamber 1. With the magnet on the multiple pulsing was comparable for the two chambers.

Chamber 4 was identical to chamber 3 and was found to have about the same efficiency as number 3 for straight tracks. For this reason the efficiency of chamber 4 was taken to be .975 ± .01 after correcting chamber 3 for the reconstruction efficiency. The overall chamber efficiency was then .748 ± .015.

It is also necessary to determine the efficiency of the cut on trajectory reconstruction at $\chi^2 = 4$. By using the positrons from muon decay it was found that the efficiency of this cut was .985 ± .01. The distribution of χ^2 for the radiative decay events is shown in Fig. 11. An overall efficiency for the spark chambers can be defined, $\beta_s = (.985)\ (.748) = .737$.

c. Photon detection efficiency

In order to facilitate the measurement of the photon detection efficiency, the gain of each of the tubes in the lead-glass hodoscope was set to the same value. This was accomplished by using a constant amplitude light source which could be moved from block to block. This source consisted of ^{207}Bi embedded in a small piece of plastic scintillator. In addition a fiber-optic light pulser system which transmitted the light from a common light pulser to each of the tubes was available for monitoring the gain of each tube on a continual basis.

A detection efficiency of about 50% at 20 Mev was desired in order to keep the background rate as low as possible yet still maintain good sensitivity to the structure dependent term of the amplitude. The information necessary to set such a threshold was obtained by measuring the pulse height in the counter of a 50 Mev electron. This pulse height was determined relative to cosmic rays which would be readily available throughout the experiment for subsequent recalibration.

The efficiency was measured using a positron annihilation beam from the 200 Mev Linac at Lawrence Livermore Laboratory. This provided a measurement for 20 and 25 Mev. The high energy points and the shape of the efficiency curve were determined by using a shower Monte Carlo program[43] to give the amount of Cherenkov light produced in lead-glass as a function of photon energy. This information was then fitted to an efficiency curve using both the annihilation beam data and the 50 Mev electron data. The resulting efficiency curve is shown in Fig. 12. The outer lines represent the error. Details of this calibration are given in Appendix B.

d. Acceptance

The acceptance was determined by a Monte Carlo technique. For radiative decay we find the acceptance of the apparatus to be .017. It was not possible to test the whole Monte Carlo program against any known process, but the acceptance of the spectrometer alone was tested with the muon decay spectrum. Fig. 13 shows the results. The Monte Carlo results are normalized to the total number of data events in the plot. Good agreement in shape is observed.

Using the Monte Carlo program we computed A_{ij} which is the probability that a radiative decay event in the i^{th} momentum bin and j^{th} angle bin will be accepted. This was done for each bin in the kinematic region to a statistical precision of 2% per bin. Thus, the statistical error in the Monte Carlo calculation is negligible compared to the statistical error of the data. The only important source of uncertainty is the variation of the spatial distribution of stopping pions in the hodoscope over the course of the experiment. This distribution is determined from a sample of the data and is used as input to the Monte Carlo program. This results in an error in the acceptance of ± 1%. The Monte Carlo program is discussed more fully in Appendix E.

7. Background

The keystone to this experiment is the assumption that the background can be completely identified from the ΔT spectrum; i.e., all sources of background consist of random hits in the positron and photon counters. This assumption would be violated by a π^o decay in which one could observe a photon converted in or before the first spark chamber or by a Dalitz decay of a π^o in which the positron passed through the spectrometer.

There are two sources of π^o's. The first would be charge exchange in the stopping hodoscope. This would produce an anomalous peak at ET = 0 which is not seen in Fig. 8a. One cannot completely rule out the possibility that as many as 4 or 5 of these prompt events may reside in Fig. 7a. But this seems unlikely, and since the possible

number of π^o events is much less than the statistical error for this experiment, this source of background is neglected. Pion beta decay, $\pi^+ \rightarrow \pi^o e^+ \nu$, would have the same elapsed time distribution as radiative decay. The branching ratio for this decay is 1.02×10^{-8}. By considering, in addition, the branching ratio for Dalitz decay and the probability of photon conversion before the first spark chamber, it is estimated that this process should contribute less than 1% to the observed event rate. This source is also neglected.

The momentum distribution for the out of time background is shown in Fig. 14. This sample was produced using the same cuts described in Table II. The background near 56 Mev/c is due to electrons from muon decay which scattered in such a way as to give an apparent momentum much larger than the actual decay momentum. The peak near 70 Mev/c comes from the two-body decay $\pi \rightarrow e\nu$. The angular distribution of the background is shown in Fig. 15. A linear correlation coefficient of -.026 for 520 events shows that for the background p and θ are uncorrelated.

8. Solution for γ

For the purposes of solving for γ, the kinematic region was divided into bins, 1 Mev/c in momentum and 4^o in angle. The theoretical distributions were then integrated bin by bin. Putting in all corrections except resolution and energy loss, equation (10) yields

$$N_{ij}^{IT} = \beta N_\pi \left(W_{IB_{ij}} + | \underline{a}(0) |^2 (F_{ij} (1 + \gamma)^2 + H_{ij} (1 - \gamma)^2) \right) \times A_{ij} E_{ij} + B_{ij} \qquad (13)$$

where N^{IT} is the number of events in the in-time part of the spectrum, B is the background, A is the acceptance, E is the photon detection efficiency, and $\beta = \beta_c\beta_f\beta_s$.

Positron energy loss in the stopping-counters was handled in the same way as for the muon decay spectrum. The momentum resolution has been discussed previously and was folded into the rate equation in a straightforward way. The angular resolution of the lead-glass counter could not be determined analytically, so it was calculated by a Monte Carlo program. The shower sharing between the blocks was assumed to be minimal, i.e., all hits were referred to the center of the block. Roughly the resolution was $\pm 6^\circ$ at 140° and $^{-8^\circ}_{+4^\circ}$ at 172°.

The following equation thus remains to be solved:

$$N_{ij}^{IT} = \beta N_\pi \left(W'_{IB_{ij}} + |\, \underline{a}(0)\,|^2 \, (F'_{ij}\,(1+\gamma)^2 + H'_{ij}\,(1-\gamma)^2) \right) + B_{ij} \,. \tag{14}$$

There are 2 ways to determine γ. The first method is to sum over i and j and solve the resultant quadratic equation for γ. The second technique is to do a two-dimensional maximum likelihood fit with γ as a parameter assuming Poisson statistics since the number of counts per bin is small. For the second technique, the shape of the background becomes important. Since the background distributions of momentum and angle are uncorrelated (as shown in Section IV.7), a back-projection method was used to determine B_{ij}. Let $P_i = \Sigma_j N_{ij}^{OT}$ be the momentum projection of the out-of-time region and $T_j = \Sigma_i N_{ij}^{OT}$ be the angle

projection. Then $B_{ij} = \frac{RP_i T_j}{N_B}$ where N_B is the total number of out-of-time events and R is the ratio of the in-time and out-of-time intervals of the ΔT spectrum.

V. RESULTS

The quadratic equation to be solved is:

$$N^{IT} = \beta N_{\pi} \left(W'_{IB} + | \underline{a}(0) |^2 (F' (1 + \gamma)^2 + H' (1 - \gamma)^2 \right) + B$$

where $N^{IT} = 363$, $\beta = .651$, $N_{\pi} = 4.365 \times 10^{11}$, $W'_{FB} = 9.685 \times 10^{-11}$, $| \underline{a}(0) | = 0.0261 M_{\pi}^{-1}$, $F' = 4.916 \times 10^{-7} M_{\pi}^2$, $H' = 1.035 \times 10^{-8} M_{\pi}^2$, $B = R N^{OT} = \frac{5}{19}(520) = 136.8$. The solution is

$$\gamma = .44 \pm .12 \text{ or } \gamma = -2.36 \pm .12$$

The contributions to the error are shown in Table III. As can be seen, the large sources of error are the photon detection efficiency, statistics, and the π^o lifetime.

Using the maximum likelihood fit we find $\gamma = .44$ or -2.38. The errors are the same as before. The momentum and angular projections are shown in Figs. 16 and 17 respectively. The solid curve corresponds to the positive solution, while the dashed line is due to the negative root. Plots of the likelihood functions as a function of γ are shown in Figs. 18a and 18b. The ratio of the peak value of the likelihood function for the positive root to that of the negative root is 0.72. While this suggests that the negative root is preferred, more information is needed before a definitive statement can be made. Two questions need to be answered. First, is the fit reasonable? Second, how certain is the separation of the roots? The answer to these questions requires a knowledge of the probability distribution of the likelihood function itself. One method of obtaining this information is by a Monte Carlo

Table III. Uncertainties contributing to error on γ.

Quantity	Error	Error on γ
Photon detection efficiency	a	± .044
Statistics on number of events	226.2 ± 22.4	± .085
π^0 lifetime	$(.828 \pm .057) \times 10^{-16}$ sec.	± .05
Flux normalization (π/total ratio)	R = .958 ± .03	± .026
Momentum calibration scale factor	± .01	± .023
Spark chamber efficiency	.748 ± .015	± .017
Acceptance	± 1.0%	± .009
Cherenkov counter path length	b	± .01
Total error		± .12

[a]Error taken from outer curves of Fig. 12.

[b]See Appendix B.

computation.[44] A number of experiments having the same physical parameters as this one were generated. The mean number of radiative decay events and background events were chosen to be the values obtained for the data. By comparing the values of the likelihood function obtained from the Monte Carlo experiments and the data, it was found that there is a (20. ± 6.0)% chance of obtaining a value of the likelihood function as low or lower than the data value. Thus, the fit is reasonable. The Monte Carlo data for the ratio of the likelihood functions for the two solutions was also examined. It was found that the value of the ratio of 0.72 implies that the negative root is favored by a probability of 3 to 1. Such a probability is certainly not a conclusive separation of the solutions, especially considering the low (but not improbable) confidence value obtained for the fit itself. For this reason no claim of separation is made. Details of the maximum likelihood method are provided in Appendix C.

In Table IV we summarize our results, including the values of γ and $\underline{b}$ calculated using the other possible values of the vector form factor. The sign of $\underline{b}$ is obtained by assuming that $\underline{a}$ is positive. Depommier *et al.*,[7] on the basis of 141 events, found γ = .4 or -2.1 (no error quoted) using $T_{\pi^0} = 1.05 \times 10^{-16}$ sec. If we use their data to recompute γ with the present value of the π^0 lifetime we find γ = +.26 or -1.98 in good agreement with our results. On the basis of 11 events Boothe *et al.*[13] found $\gamma = 1.6 \pm .7$ or $-3.1 \pm .7$ using $T_{\pi^0} = 1.8 \times 10^{-16}$. They did not provide enough information to recompute γ with the present value of the lifetime. But if we recompute our data with their value of the lifetime

Table IV. Values of $\underline{b}(0)$ and γ obtained from the experimental solutions and the values of $\underline{a}(0)$. The sign $\underline{b}(0)$ is determined under the separate assumption that $\underline{a}(0)$ is positive from quark triangle diagrams.

Method	$\underline{a}(0) \times m_\pi^{-1}$	γ (upper solution)	$\underline{b}(0) \times m_\pi^{-1}$	γ (lower solution)	$\underline{b}(0) \times m_\pi^{-1}$
Quadratic equation	.0261 ± .0009 (CVC)	.44 ± .12	.011 ± .003	-2.36 ± .12	-.062 ± .004
Likelihood fit	.0261	.44 ± .12	.011 ± .003	-2.38 ± .12	-.062 ± .004
Quadratic equation	.035 ± .0025 (ρ-dominance)	.07 ± .13	.002 ± .005	-1.99 ± .13	-.069 ± .005
Likelihood fit	.035	.07 ± .13	.002 ± .005	-2.01 ± .13	-.069 ± .005
Quadratic equation	.031 (ρ-dominance)[a]	.21	.006	-2.13	-.066
Likelihood fit	.031	.21	.006	-2.15	-.067

[a]No error is quoted for this value of $\underline{a}$, so we give no error on γ or $\underline{b}$.

we find $\gamma = 1.13 \pm .013$ or $-3.01 \pm .013$. Again their results are consistent with ours.

The Particle Data Group[18] gives a current value for the branching ratio of 3.0×10^{-8} based on Depommier et al. where the photon and electron energies were required to be above 48 Mev. This is not a convenient cut for us to make since we do not measure photon energy. But if we use our value of γ in the equations of Depommier et al. then we obtain a branching ratio of 3.7×10^{-8}. Defining the branching ratio in a way most suitable to this experiment (electron momentum > 56 Mev/c and opening angle > 132^{o}) yields a value of $(5.6 \pm .7) \times 10^{-8}$.

One contribution to this result over which we have no control is the value of the π^{o} lifetime. The Particle Data Group warns that their result should be used with some caution because the experiments are not consistent, although the error on the lifetime has improved considerably in the last year. We must ask how our results and their agreement with theory will vary as a function of $T_{\pi o}$. The purpose of this experiment is to measure b, the axial vector form factor; the output of the theoretical calculations we have considered is b, but it is very convenient to use the parameter $\gamma = b/a$. Unfortunately the dependence of the vector form factor (as calculated by CVC theory) on the lifetime makes the theoretical predictions for γ functions of $T_{\pi o}$. The one exception to this is the relativistic quark model which makes a prediction for γ independent of a.

Suppose we introduce a new quantity

$$\gamma'(T_{\pi o}) \equiv \gamma(T_o)\left(\frac{T_o}{T_{\pi o}}\right)^{1/2} = \frac{b}{2}\left(\pi M_\pi^3 T_o\right)^{1/2}$$

where T_0 is chosen to be $.828 \times 10^{-16}$ sec. Theoretical predictions for γ' are independent of T_{π^0}, and since the predictions for γ previously discussed were evaluated at $T_{\pi^0} = T_0$, they were in fact predictions for γ'. This does not eliminate all the dependence on T_{π^0}. Determination of γ' from the data still requires a knowledge of the vector contribution to the branching ratio. In Figs. 19a and 19b we have plotted the values for γ' obtained from our data as a function of T_{π^0}. We have included the recent measurements of the π^0 lifetime given by the Particle Data Group. The vertical error bars are our errors not including the certainty on T_{π^0}. The horizontal error bars are those assigned by the original experimenters.

VI. CONCLUSIONS

1. Comparison with theory

It is clear that the uncertainty in the experimental determination of γ is far less than the theoretical spread in values. Our value of $\gamma = -2.36$ is in agreement in magnitude with the result $|\gamma| = 2.14$ of reference 29. We have already pointed out that this model requires the use of current algebra to determine $\underline{b}$ from the charged radius of the π^+ while ignoring the relationship of r_{π^+} to the masses and widths of the ρ and A_1 mesons. The rest of our discussion will be directed toward the smaller magnitude root, which is more interesting from a theoretical point of view. We take the position that since all the other models under study predict $|\gamma| \leq 1$ they should be compared with our value $\gamma = 0.44$.

From Table I, we see that in the framework of current algebra we are in agreement with the results $|\gamma| = .59$[26] and $|\gamma| + .35$.[25] The subtraction constant δ should be in the range -.5 to -1. The choice $\delta = -1$ gives $\Gamma(\rho \to \pi\pi) = 140$ Mev which is reasonably consistent with the experimental value of 153 ± 3 Mev,[18] but $\delta = -.5$ predicts a width of 107 Mev which is in definite disagreement with experiment. Both models make predictions for the pion charge radius which are almost 2 standard deviations away from the experimental value.[30] Also, their predictions for the A_1 width are too low, but considering the controversy surrounding the A_1 at this time, it is difficult to say too much about this. The agreement with the ρ width indicates that the preferred value of γ should be closer to .59 than to .35.

Of more interest is that we are consistent with the result $\gamma = .65$,[22] both in magnitude and sign. This model gives a good result for the ρ width of 146 Mev, and a value for the pion charge radius of .67 f which is in agreement with the experimental result, $(.8 \pm .1)$ f.[30] Again the A_1 width results are questionable. Our results give support to this phenomenological Lagrangian approach.

As far as quarks are concerned, we differ in sign with the relativistic model. If we speak only of magnitude we can be considered compatible with nucleon-antinucleon model. Taking the model seriously our value of γ predicts a quark mass of the order of the pion mass. We do not agree with Pestieau's calculations when using the Gell-Mann-Zweig, the Han-Nambu, or the Colored quark models. We are also not consistent with the predictions $\gamma = 0$ using the non-relativistic quark model or the sigma model. Currently the sigma model is getting the most attention; it is appealing because it includes PCAC. Attempts are being made to impose quark confinement on the model. Preliminary results indicate that as confinement is applied, the value of γ moves away from zero in a positive direction.[37] The work is continuing and it will be some time before it is known how large a value of γ will result.

If we use ρ-dominance instead of CVC to determine the vector form factor we find that γ is consistent with 0. However, the CVC value must be considered preferred; ρ-dominance is included only for completeness. In the last year the error on the world average of the π^0 lifetime has gone down a factor of 2. It is unlikely that the lifetime could

change sufficiently to have any effect on the conclusions one draws about the status of the different theories.

Another important contribution of this experiment is the conclusive proof that there is axial vector coupling in radiative decay. This coupling is either about one half or twice the vector coupling depending on which solution is chosen. Hopefully these new results should invite renewed theoretical interest in this problem.

2. Suggestions for future study

Since this experiment and the previous one agree to a precision far better than the uncertainty on the theoretical predictions, an additional experiment to measure the two solutions of γ would not be called for at this time. However, a conclusive separation of the roots would be of interest. As discussed in Appendix C, such an experiment would require substantially more than 500 events so that the probability of obtaining a distribution of events which does not show a clearly preferred root is small. Obtaining this number of events would require a different experimental design. A higher beam intensity would not be the answer because the pile-up of muons in the stopping counter would overwhelm the radiative decay events with background. An accurate determination of both photon energy and opening angle would make the selection of the radiative decay events easier, although the trigger rate would still be very high relative to the number of radiative decay events. Such a measurement of photon energy would require NaI. With such a high background rate, the dead-time of the NaI would be a problem.

Another method would be to observe the decay in flight. This would eliminate the problem of the muon pile-up and would make the electron momentum region below 56 Mev/c accessible. This would be an advantage since the two roots separate well in this region. A large pion flux would be required. Because of the duty factor TRIUMF would be preferred over Los Alamos.

APPENDICES

A. Derivation of the Matrix Elements

In the text we described briefly the diagrams which contribute to the radiative decay amplitude. In this appendix we will provide more detail. The mathematical expressions become rather complicated. Our purpose is not to prove the correctness of the algebra, but to show (1) how it comes to be that the decay can be expressed in terms of only two form factors, and (2) the restrictions placed on the decay by the fact that ordinary $\pi \to e\nu$ decay involves only an axial-vector hadronic current.

A calculation of the T-matrix element for diagram (a) of Fig. 1 is a straightforward application of Feynman rules[45] involving a $\pi e\nu$ vertex, an electron propagator, and a photon-electron vertex. Thus

$$\tilde{T}_a = \frac{-eG}{\sqrt{2}} \varepsilon_\nu(k) A f_\pi \bar{\mu}(q) \gamma_\nu \left\{ \frac{-i\gamma \cdot (q + k) + M_e}{(q + k)^2 + M_e^2} \right\} \times i\gamma \cdot p(1 + \gamma_5) \nu(Q) \tag{A1}$$

where

$$A = \left(\frac{1}{2\pi}\right)^6 \left(\frac{M_e M_\nu}{4 k_o q_o Q_o p_o}\right)$$

The mass of the neutrino will cancel at a later step in the calculation of the decay rate.

The matrix element for diagram (b), the one-pion intermediate state (Born term), is similar, except here one has a spin-zero meson-photon vertex and a meson propagator.

$$\tilde{T}_b = \frac{eGA\varepsilon_\nu(k)}{\sqrt{2}} \; f_\pi \; (p - k)_\lambda \frac{(-2p + k)_\lambda}{(p - k)^2 + M_\pi^2} \times \bar{\mu}(q)\gamma_\lambda \; (1 + \gamma_5) \; \nu(Q) \tag{A2}$$

The remaining three diagrams describe the more complicated case where all 3 decay particles leave from the same vertex. We include all 3 diagrams into a matrix element T given by,

$$\tilde{T} = \frac{iG\cos\phi}{\sqrt{2}} \; < 0\gamma \mid J_\lambda{}^o(0) \mid 0\pi > \frac{1}{(2\pi)^3} \cdot \sqrt{\frac{M_e M_\nu}{q_o Q_o}}$$

$$\times \bar{\mu}(q)\gamma_\lambda \; (1 + \gamma_5) \; \nu(Q) \tag{A3}$$

where $J_\lambda{}^o(0)$ is the weak hadronic current, the notation $<0\gamma|$ means there are 0 pions and 1 photon in the final state, and $|0\pi>$ means there is 1 pion and no photon in the initial state.

Now we use the LSZ reduction formalism[46] to simplify the problem.

$$(2\pi)^{3/2} \sqrt{2k_o} < 0\gamma \mid J_\lambda{}^o(0) \mid 0\pi > = ie\varepsilon_\nu(k)$$

$$\times \left[\int d^4x e^{-ik\cdot x} < 0 \mid T \; (j_\nu^{em}(x) \; J_\lambda{}^o(0) \mid \pi > \right]. \tag{A4}$$

We have dropped the so-called "seagull" term. Using this result in equation (A3), we are left with

$$\tilde{T} = \frac{iG\cos\phi}{\sqrt{2}} \; \frac{\varepsilon_\nu(k)}{(2\pi)^{3/2}} \; \frac{M_e M_\nu}{2q_o Q_o k_o}$$

$$\left[ie \times \int d^4x e^{-ik\cdot x} < 0 \mid \; T \; (j_\nu^{em}(x) \; J_\lambda{}^o(0) \mid \pi > \right] \bar{\mu}(q)\gamma_\lambda \; (1 + \gamma_5) \; \nu(Q) \; . \tag{A5}$$

Where before we had a matrix element of the hadronic current between states with photons and pions, we now have the matrix element between

the more familiar states of 0 and 1 pions respectively. We have also introduced the electromagnetic current.

We now try to write a general expression for $\tilde{T}$ as

$$\tilde{T} = \tilde{T}_V + \tilde{T}_A \tag{A6}$$

where the two terms are the vector and axial vector parts of $J_\lambda^{\,o}$.

For $\tilde{T}_V$ we must form the most general expression for the vector part of the weak hadronic current out of the available Lorentz invariants, the four-vectors ε, p, and k. Since the pion is pseudoscalar there is a parity change between initial and final states which means we must actually construct an axial vector.

We then have

$$\tilde{T}_V = \frac{eG\cos\phi}{\sqrt{2}}\ A\ \underline{a}(s)\ \varepsilon_{\lambda\nu\rho\sigma}\ \varepsilon_\nu(k)\ p_\rho\ k_\sigma\ \bar{\mu}(q)\gamma_\lambda\ \ (1+\gamma_5)\ \nu(Q). \tag{A7}$$

This is diagram 1c.

For the most general expression for the axial vector current contribution we have

$$\tilde{T}_A = \frac{ieG\cos\phi}{\sqrt{2}}\ A(2\pi)^{3/2}\ \varepsilon_\nu(k)\ M_{\nu\lambda}\ \bar{\mu}(q)\gamma_\lambda\ (1+\gamma_5)\ \nu(Q) \tag{A8}$$

$$M_{\lambda\nu} = \frac{-i}{(2\pi)^{3/2}\ \sqrt{2p_o}}\ \left[H_1\ \delta_{\lambda\nu} + H_2 k_\lambda p_\nu + H_3 p_\lambda p_\nu + H_4 p_\lambda k_\nu + H_5 k_\lambda k_\nu\right] \tag{A9}$$

where H_i (i = 1,5) are form factors and functions of s. Because the photon is transverse ($\varepsilon \cdot k = 0$) H_4 and H_5 do not contribute.

We require that the total amplitude be gauge invariant, i.e., that the matrix element be invariant under the transformation $\varepsilon_\nu \to \varepsilon_\nu + \lambda k_\nu$. $\tilde{T}_V$ is manifestly gauge invariant because of the tensor $\varepsilon_{\lambda\nu\rho\sigma}$. Thus we require that $\tilde{T}_a + \tilde{T}_b + \tilde{T}_A$ be gauge invariant. Imposing this yields the relations:

$$H_1 + H_2\ (p\cdot k) = f_\pi \tag{A10}$$

$$H_3 = 0\ . \tag{A11}$$

If $p\cdot k = 0$ we have

$$H_1\ (p\cdot k=0) = f_\pi \quad \text{or} \quad H_1\ (s=m_\pi^2) = f_\pi\ . \tag{A12}$$

Then with the definition $\underline{b}(s) \equiv -H_2(s)$, we have

$$H_1 = f_\pi + \frac{s - m_\pi^2}{2}\ \underline{b}(s)\ . \tag{A13}$$

Note that there is now only one unknown left in $M_{\lambda\nu}$, $\underline{b}(s)$, the axial vector form factor.

We can then write

$$\tilde{T}_A = \tilde{T}_d + \tilde{T}_e \tag{A14}$$

where $\tilde{T}_d$ is that part which depends on the form factor $\underline{b}$ and $\tilde{T}_e$ is the contact term. They correspond exactly to diagrams 1d and 1e in the text.

$$\tilde{T}_d = \frac{eG\cos\phi}{\sqrt{2}}\ A\ \underline{b}(s)\ \left(\varepsilon_\lambda(k)k_\rho - \varepsilon_\rho(k)k_\lambda\right) p_\rho \times \bar{\mu}(q)\gamma_\lambda\ (1 + \gamma_5)\ \nu(Q) \tag{A15}$$

$$\tilde{T}_e = \frac{eG\cos\phi}{\sqrt{2}}\ A\ \Big\{f_\pi\varepsilon_\lambda(k)\ \bar{\mu}(q)\gamma_\lambda\ (1 + \gamma_5)\ \nu(Q) + i\ M_e f_\pi\ \frac{\varepsilon(k)\cdot p}{k\cdot p}\ \bar{\mu}(q)\ (1 + \gamma_5)\ \nu(Q)\Big\}\ . \tag{A16}$$

We can then write

$$\tilde{T}_{IB} = \tilde{T}_a + \tilde{T}_b + \tilde{T}_e \tag{A17}$$

and

$$\tilde{T}_{SD} = \tilde{T}_c + \tilde{T}_d \ . \tag{A18}$$

Performing the algebra yields equations 3 and 4.

1. The determination of b

We are now in a position to elaborate on the connection between $\underline{b}$ and the ρ and A_1 mesons. Das et al.[23] write matrix elements for ρ and A_1 decay in the same form as our expression for $\tilde{T}_A$, equation (A8). The question is whether the form factor which multiplies the invariant $\delta_{\lambda\nu}$ should have a subtraction in its dispersion relation.

If we assume an unsubtracted dispersion relation for $H_1(s)$ dominated by an A_1 pole (in analogy to the procedure followed for the vector form factor in Section II.3), then we obtain

$$H_1(s) = \frac{F_{A_1} F_{A_1\pi\gamma}}{-s + M_{A_1}^2} \tag{A19}$$

Using the condition (A12), we find

$$f_\pi = \frac{F_{A_1} F_{A_1\pi\gamma}}{M_{A_1}^2 - M_\pi^2} \tag{A20}$$

which leads to

$$\underline{b}(s) = \frac{2F_{A_1} F_{A_1\pi\gamma}}{(-s + M_{A_1}^2)(M_{A_1}^2 - M_\pi^2)} \tag{A21}$$

We now have

$$\underline{b}(0) = \frac{2f_\pi}{M_{A_1}^2} = \frac{f_\pi}{M_\rho^2} \tag{A22}$$

where we have used the Weinberg rule $M_{A_1} = \sqrt{2}\, m_\rho$.[10] This yields the result $|\gamma| = 1.2$ discussed in the main text; the widths of the ρ and A_1 are 36 MeV and 605 Mev respectively.

If a subtraction is used for the form factor multiplying the covariant $\delta_{\lambda\nu}$ in the matrix elements for ρ and A_1 decay, the widths become more reasonable (see Table I). It is then natural to write a subtracted dispersion relation for $H_1(s)$. Selecting the subtraction point at $s = m_\pi^2$ we have

$$H_1(s) = f_\pi + \frac{s - M_\pi^2}{\pi} \int \frac{\text{Im}\, H_1(s')\, ds'}{(s' - M_\pi^2)\,(s' - s)} \quad . \tag{A23}$$

If we assume the dispersion integral is dominated by the A_1 pole, we have

$$\underline{b}(s) = \frac{2F_{A_1} F_{A_1\pi\gamma}}{(-s + M_{A_1}^2)\,(M_{A_1}^2 - M_\pi^2)} \quad . \tag{A24}$$

This is the same as equation (A21), but we now do not have expression (A20) to help us evaluate the product $F_{A_1} F_{A_1\pi\gamma}$.

By assuming that the $A_1\pi\gamma$ vertex proceeds via ρ-dominance, the coupling constant $F_{A_1\pi\gamma}$ can be related to G_S and G_D, the S and D wave coupling constants for the decay $A_1 \to \rho\pi$. G_S and G_D can in turn be related to the parameter δ described in the text.[23] This is the method of

reference.[16] Vaishya[25] starts with the expression for $M_{\lambda\nu}$ (equation A9), and by assuming chiral SU(2) × SU(2) symmetry, current algebra, PCAC, meson dominance, and smoothness of proper vertices derives a relationship between $\underline{b}$ and δ. Weinberg's first sum rule is also used,[10]

$$\frac{F_{A_1}^2}{M_{A_1}^2} + f_\pi^2 = \frac{f_\rho^2}{M_\rho^2} \quad . \tag{A25}$$

The calculation of Das et al.[26] is equivalent except they require $\delta = -1$ by assuming an unsubtracted dispersion relation for the pion electromagnetic form factor F_+. Brown and West[27] take a more general approach by starting with the 3-point functions and using Ward identities to find the relationship between $\underline{b}$ and δ. It should be stressed that all these calculations are equivalent and yield the same relation between $\underline{b}$ and δ.

B. Construction and Calibration of the Lead-glass Hodoscope

The construction of the lead-glass hodoscope is shown in Fig. 20. The blocks were 6 inch cubes of Bourns PEMG2 lead-glass with a radiation length of 1.15 inches. They were optically isolated by 1/4 mil aluminized mylar and were supported at their corners by 1/16" plastic spacers. The 5" photomultiplier tubes were rigidly attached to the blocks with a transparent silicone rubber.[47] This joint proved to be very strong with good light transmission. For safety the tube was also supported by a concentric ring attached to the spacers at the block corners by springs, although the joints would probably have held through the course of the experiment with no support.

A Monte Carlo calculation showed that the light collection efficiency would be best without a lucite light pipe. This was verified using light produced by both a light pulser and a 50 Mev electron beam, comparing an arrangement with no light pipe to that with light pipes 2" and 6" long. It should be noted that the test was performed using an optical grease instead of the silicone rubber. We did not believe that given the geometrical constraints of our apparatus, we could make a grease joint stable over a long period of time. Also grease would not have worked with the 58 AVP's which had curved surfaces.

Since the counter had to operate in the vicinity of our C-magnet, care was taken to provide magnetic shielding. The box was constructed of 1/2" steel. An additional 1/4" of silicon steel was wrapped around the glass wall. The tubes were wrapped with five layers of .015"

silicon steel, but note that the steel could not extend beyond the photocathode. The front plate of the counter was 1/16" aluminum to which were glued eight layers of 0.015" silicon steel.

This shielding proved to be inadequate. The gains of the tubes were sensitive to the presence of the field. The addition of a "window frame" of 1/2" X 6" steel just outside the front of the hodoscope helped by drawing some of the flux from inside the counter, but the gain of the tubes was still field dependent and the effect of the field varied from tube to tube depending on its location inside the box. It was decided that the counter would be calibrated with the C-magnet on and the main field of the cyclotron in its normal polarity (i.e., the standard operating conditions).

The photo tubes were Amperex XP1040's and 58 AVP's. These were run at positive high voltage. The rate was not expected to be high and with our construction limitations it was more convenient to have the photocathode at ground potential. The basic electronics pertaining to the hodoscope is shown in Fig. 5. A constant fraction discriminator was chosen for the gamma sum signal for maximum timing accuracy. A variable attenuator was used at the input of the amplifier since the different calibrations and tests varied in light amplitude. The discriminator was set for a 100mv threshold and the amplifier at a gain of 10.

Each block had its own fiber-optic light pipe attached to the front plate of the counter. The input ends of these fibers were attached to the "light pulser wheel" shown in Fig. 21. The light

pulser could rotate on the disc and thus illuminate each of the fibers one at a time. Once the relative transmission of the fibers was determined, this provided an easy means of monitoring the gain without having to worry about light pulser drift. An AR-4 lamp was used for amplitude measurements.[48]

We did not attempt to measure the photon energy; we were only concerned with knowing the detection efficiency. To do this we set the gains of all the tubes to the same value during the experiment and calibrated the counter afterwards. The discriminator threshold was set as high as possible in order to reduce the background due to random counts in the photon counter without seriously lowering the sensitivity to γ. The threshold was set to give an efficiency of about 50% at 20 Mev.

The primary calibration standard was cosmic rays. This test could be done only with blocks in the second row. The procedure was to require coincidence between row 1 (the top row) and row 4 and look at the pulse height in row 2. A typical pulse height spectrum is shown in Fig. 22a. This was done one column at a time. Row 3 served as a "beam hardener." If the coincidence was instead done between row 1 and row 3, the resulting spectrum was no longer symmetric but was skewed on the low energy end. By using a 50 MeV electron beam at the cyclotron we determined that the pulse height of a vertical cosmic ray was equivalent to a 120 MeV electron entering through the front face of the counter. If we assumed that the width of the cosmic ray pulse height spectrum was dominated by photo-statistics, then we would have expected 47

photo-electrons from a 120 MeV electron. We would then have about 7.7 photo-electrons at 20 MeV. From the electron detection efficiency of lead-glass counters similar to ours, Sober et al.[49] determined that a 20 MeV electron should produce about 6.6 photo-electrons.

Cosmic rays provided a means of calibrating row 2, but some other means was needed for the other three rows. The light pulser alone was not sufficient because of differences in light transmission among the fibers. We used a constant amplitude light source which could be moved from block to block. This source, which we called the "plunger source," consisted of ^{207}Bi embedded in a 1/4" cube of plastic scintillator. The scintillator was mounted in a 1/2" diameter metal cup attached to a rod, so that it could be pushed through a hole in the front plate of the counter and up against the face of the block. The metal cup provided an air gap between the block and the scintillator for uniform light transmission. A typical pulse height spectrum is shown in Fig. 22b. We also glued a small piece of ^{207}Bi embedded scintillator to one of the blocks in row 2 (block #22) to provide a fixed light source.

We used cosmic rays to set the gain of tube #22. We measured the coincidence ratio $\frac{1.2.4}{1.4}$ where the numbers refer to row number. The discriminators for the tubes in rows 1 and 4 and the two coincidence units are not shown in Fig. 5; they were used only for the purposes of this measurement. However, for the row 2 signal, we used the photon counter electronics shown in Fig. 5 with, of course, all tubes but #22 disconnected from the "row" fan-in's. A 15 db attenuator was placed at

the input of the gamma sum discriminator to bring the cosmic ray signal down to 21.2 Mev equivalent amplitude. The voltage on tube #22 was adjusted until this "3/2" coincidence ratio was about 50%.

The amplitude of the light pulser and the plunger source was then measured. The voltage on all the other tubes was adjusted to put the peak of the ^{207}Bi spectrum from the plunger source in the same pulse height analyzer channel as tube #22. The light pulser was also measured for each block. The photo multiplier tube high voltage was adjustable in 20 volt steps. Using the light pulser and plunger source data, we calculated the transmission of each fiber relative to fiber #22. With these transmission values it was possible to do the subsequent monitoring of the calibration with the light pulser. On a weekly basis the voltage was adjusted for tube #22 using the fixed ^{207}Bi source. Cosmic rays were checked. The light pulser permitted adjustment of the voltages on the other tubes. In general the voltage did not change more than 10 volts over the course of the experiment.

In order to determine the detection efficiency we used the annihilation beam of the electron linac at Lawrence Livermore Laboratory to calibrate block #22. The set-up is shown in Fig. 23. The positron beam struck a thin berylium target producing photons from both bremsstrahlung and annihilation. Charged particles were swept away by the broom magnet. The photon flux was measured by the ionization chamber. The lead-glass was mounted in a light-tight box with a front plate identical to the one on the hodoscope. In order to subtract the bremsstrahlung the experiment was repeated for electrons.

The efficiency of the detector was given by:

$$\varepsilon = \left(\left(\frac{C \cdot B}{IC^*} \right)_{e^+} - K \left(\frac{C \cdot B}{IC^*} \right)_{e^-} \right) \frac{Q}{A} \times \left(\frac{1}{18.09} \right) \cdot \qquad \text{(B1)}$$

Here C·B is the coincidence between the detector and the beam burst, IC* is the ion chamber counts with background subtracted, K is an energy dependent factor which normalizes the ion chamber response for electrons to that of positrons. Q/A is an energy dependent factor which is the number of IC counts per annihilation photon. The term $\frac{1}{18.09}$ is a correction for solid angle.

The values of K and Q/A had been previously measured by the Linac staff. Since we were detecting the primary photon beam, we were required to run at a very low beam current to reduce pile up in our detector. The ionization chamber was counting at a rate of 2 to 3 times background. The data taking was done in 4 runs over a period of 2 months and 1 run 3 months later. The results are shown in Table B-I. The data at 25 MeV shows reasonable consistency over 3 different runs. We do not understand what happened at 45-65 Mev. Because of the limited amount of time available, we were not able to investigate the effect further. We hoped for a definitive measurement at 37 Mev for the last run but the value for that run seems low.

In order to fix the efficiency at the high energy end and determine the shape of the efficiency curve, a Monte Carlo program NEMCASP[48] was used to study the production of Cherenkov light from electromagnetic showers in lead-glass. For each generated event the program calculated the amount of Cherenkov light produced in each 1" layer of the glass.

Four hundred events each were run for photon energies of 25, 30, 40, 50, and 70 Mev and 200 events each for 15, 20, and 35 Mev. The efficiency ε for detecting an amount of light E is given by

$$\varepsilon = \sqrt{\frac{2}{\pi}} \frac{1}{\sigma_o} \int_o^E e^{\frac{-(E_o - t)^2}{2\sigma_o^2}} dt . \qquad (B2)$$

There are 2 free parameters: a threshold E_o and a resolution at that energy, σ_o. The resolution σ_o was estimated by assuming that a 20 Mev photon produces an average of n = 7 photo-electrons when it deposits the full energy in the block. The results were not very sensitive to the value of n between 5 and 10. The threshold of the counter was related through the cosmic ray calibration to the pulse height of a 50 Mev electron. From the distribution of Cherenkov light obtained by running NEMCASP for 50 Mev electrons, it was possible to calibrate the scale of the Cherenkov light produced by NEMCASP and set a threshold E_o corresponding to 21 Mev. By determining the probability of detection for each generated event, the detection efficiency for that energy was obtained. Fig. 12 shows the resulting efficiency curve. The center line corresponds to a threshold of 21 Mev. The outside curves represent the error. The uncertainty on the rising part of the curve comes from a ±10% error on the threshold. The error for the high energy points is due to the statistics on the number of generated Monte Carlo cascades.

One question remaining to be answered is the justification for calibrating only one tube. This was answered by raising the voltage on the tube by 20 volts during the linac measurement at 25 MeV. The change

in efficiency was only 2%. The gains of all the tubes were set well within this tolerance. The distribution of gains should be symmetric about the value for tube #22.

The efficiency discussed so far is for normally incident photons which have a potential path length through the Pb-glass of 6 inches. It is necessary to correct for photons which strike at oblique angles, thus potentially traversing more or less (at the edges of the array) lead-glass. This correction was determined by Monte Carlo technique. Using the value $\gamma = .3$, radiative decay events were generated under the constraint that the photon energy was the value under study. The path length t of each photon through the Pb-glass was determined. Using the results from NEMCASP the detection probability for that photon was obtained. Table B-II gives the results showing the average path length and average detection efficiency relative to the efficiency for traversing the full block length for all generated events which strike the counter and also for the accepted events. The standard deviation of the mean for the detection probability of the accepted events is quite small, thus producing a small error on the final efficiency. The error on γ due to the path length correction uncertainty is $\pm .005$.

The position of the shower is determined by averaging the energy deposited in each row and column. The pulse area for each row and column was measured by charge to time (QT) convertors which produced an output pulse whose width was proportional to the input pulse area. This pulse was differentiated and digitized by scalers similarly to the pulses from the magnetostrictive wands. If R_i is the number of scaler

counts above pedestal for the i^{th} row, then the vertical position is

$$Y = \frac{\sum_{i=1}^{4} i\, R_i}{\sum_{i=1}^{4} R_i} . \qquad \text{(B3)}$$

The size of the block is the unit of length. Most of the time the shower is completely contained in one block, but because of noise on the QT's most showers look like a sharing between adjacent blocks. We want to reject events where a significant amount of energy is shared between non-adjacent blocks. To accomplish this we require that the blocks which appear to be sharing the shower contain 81% of the total row or column energy.

If the photon and positron were always generated in a horizontal plane running through the center of a block, the resolution function would be essentially flat with a width of $\pm 8^{o}$. The actual case requires a Monte Carlo calculation. The assumption is made that energy sharing between blocks can be ignored, so the measured shower position will always be the center of the block. We can analyze the data to determine the amount of shower sharing. If the position of the photon is more than .5 inches from the center of the block, then at least 10% energy sharing has occurred. The fraction of events for which this is true of the horizontal coordinate is .166 ± .027 and .267 ± .022, radiative decay and background events respectively. For the vertical coordinate the fractions are .162 ± .03 and .253 ± .023. We clearly see that less sharing

occurs for the radiative decay events. (Part of this difference may be due to photons from electron bremsstrahlung in the beam which strike the counter at an oblique angle, thus possibly traversing two blocks.) For those events with photon position more than .5 inches from the center of the block, the average position is 1.2 inches from center. Thus it is a reasonable approximation to determine the resolution assuming complete containment within the block.

The final question that should be discussed is the energy resolution of the Pb-glass counter. The total pulse height from all the blocks is measured; it is used for normalization in the subroutine which calculates the shower location. We do not use this energy information in the analysis. Heusch et al.[50] have measured the energy resolution of a lead-glass Cherenkov counter for 150 MeV photons. They found FWHM = .33 at this energy. The Particle Data Group gives for the energy resolution of Pb-glass shower detectors the formula

$$\text{FWHM} = \frac{(8 - 12)\%}{\sqrt{E}}$$

where E is in Gev. At 150 Mev one would expect the FWHM to be in the range .2-.31.

From the measured opening angle and electron momentum, we can calculate the photon energy. We require momentum less than 70 MeV in order to avoid negative photon energies. We can then compare this calculated photon energy with the measured one. The Monte Carlo program was used to simulate this. The photon energy was smeared with a gaussian resolution, $\sigma = \frac{.05}{\sqrt{E}}$. The measured opening angle was again determined by

assuming that the shower location is referred to the center of the block. This angle and the positron momentum smeared by energy loss and resolution were used to calculate the predicted photon energy. In Fig. 24a we histogram the quantity $\frac{k-E}{k}$, where k is the predicted photon energy and E is the measured value, for the radiative decay events. The dots are the results of the Monte Carlo program normalized to the data. The error bars are statistical and include both the statistics on the data and on the number of events generated by the Monte Carlo. The agreement is very good, fortuitous considering the size of the error bars. Fig. 24b shows the same histogram for the out-of-time events showing poor agreement between the Monte Carlo results and the data. The fact that there is a peak at all is due to the phase space being limited to 56-70 MeV and 132^{o}-180^{o} and that the measured photon energy is required to be above 20 MeV by the discriminator threshold.

Table B-I. Table of data for the photon detection efficiency calibration using a positron annihilation beam. Terms are described in Appendix B.

Run	Energy (Mev)	$\left(\frac{C \cdot B}{IC^*}\right)_{e^+}$	$\left(\frac{C \cdot B}{IC^*}\right)_{e^-}$	K	Q/A	Target Thickness (mil)	Efficiency
1	25.	1630.	1229.	.9153	.0172	10	.480
	25.	1613.	1157.	.9153	.0179	5	.548
	37.	2931.	2633.	.938	.0249	10	.633
	37.	3015.	2665.	.938	.026	5	.739
2	25.	1860.	1430.	.9153	.0172	10	.523
	25.	1780.	1418.	.9153	.0172	5	.477
3	45.	3426.	3291.	.9523	.0296	10	.477
	45.	3512.	3389.	.9523	.0308	5	.485
	55.	3795.	3793.	.9709	.0358	5	.232
	65.	3992.	3983.	.9894	.042	10	.119
	65.	4118.	4120.	.9894	.0437	5	.111
4	25.	1866.	1398.	.9153	.0172	10	.557
	25.	1821.	1361.	.9153	.0179	5	.569
	35.	2714.	2280.	.9338	.0234	10	.756
	35.	2735.	2376.	.9338	.0244	5	.696
	20.	1345.	971.	.9064	.0141	10	.362
	20.	1306.	898.	.9064	.0142	5	.386
5	37.	2826.	2505.	.938	.0249	10	.655
	37.	2833.	2564.	.938	.0260	5	.615

Table B-II. Results of path length correction to the photon efficiency

Photon Energy (MeV)	All Events		Accepted Events	
	Path length (inches)	Average detection probability Normalized to unit probability for 6 inches	Path length (inches)	Average detection probability
25	5.7 ± 1.4	.92 ± .16	5.7 ± 1.4	.92 ± .18
35	5.7 ± 1.4	.93 ± .15	5.8 ± 1.2	.94 ± .14
45	5.7 ± 1.4	.94 ± .15	5.8 ± 1.2	.9 ± .14
55	5.7 ± 1.4	.96 ± .14	5.9 ± 1.0	.98 ± .101
65	5.7 ± 1.4	.96 ± .15	6.1 ± 0.4	1.00 ± .050

Table B-II. Results of path length correction to the photon efficiency

Photon Energy (MeV)	All Events		Accepted Events	
	Path length (inches)	Average detection probability Normalized to unit probability for 6 inches	Path length (inches)	Average detection probability
25	5.7 ± 1.4	.92 ± .16	5.7 ± 1.4	.92 ± .18
35	5.7 ± 1.4	.93 ± .15	5.8 ± 1.2	.94 ± .14
45	5.7 ± 1.4	.94 ± .15	5.8 ± 1.2	.9 ± .14
55	5.7 ± 1.4	.96 ± .14	5.9 ± 1.0	.98 ± .101
65	5.7 ± 1.4	.96 ± .15	6.1 ± 0.4	1.00 ± .050

C. Maximum Likelihood Method

The basis of the maximum likelihood method is the assumption that the observed distribution is in fact the most likely distribution. When the number of events is sufficiently large for gaussian statistics to be valid, this leads to the familiar χ^2 distribution. In this experiment the number of events per bin is small, so Poisson statistics must be used.

For simplicity let us assume we have a one-dimensional distribution; the method can easily be extended to two dimensions. Let n_i be the number of events in the i^{th} bin, $\bar{n}_i$ be the number of expected events in the i^{th} bin, and N be the number of bins. The probability of observing this distribution is given by

$$L = \prod_{i=1}^{N} \frac{e^{-\bar{n}_i} (\bar{n}_i)^{n_i}}{n_i !} \tag{C1}$$

We now make the likelihood assumption: the correct parent distribution is the one which maximizes L. Taking the natural log we have

$$\ell n\ L = \sum_{i=1}^{N} \left(-\bar{n}_i + n_i\ \ell n\ \bar{n}_i - \ell n\ (n_i\ !) \right) \tag{C2}$$

There is no analytic solution to this problem, so we solve it by varying the $\bar{n}_i$ in order to minimize $-\ell n\ L$. For our purposes with radiative decay we minimize

$$-\ell n\ L = \sum_i \sum_j \left(\bar{n}_{ij} - n_{ij}\ \ell n\ \bar{n}_{ij} + \ell n\ (n_{ij}!) \right) \tag{C3}$$

where i and j vary over bins in p and θ respectively,

$$\bar{n}_{ij} = \beta N_{\pi} \left(W'_{IB} + | \underline{a}(0) |^2 \left(F'_{ij} (1 + \gamma)^2 + H'_{ij} (1 - \gamma)^2 \right) \right) + B_{ij} \tag{C4}$$

and $n_{ij} = N_{ij}^{IT}$ with the definitions used in section IV.8.

The likelihood function, $L(\gamma)$, is a peculiar function. As defined above, $L(\gamma)$ is the probability of obtaining precisely the observed distribution of events if γ is the "true value." $L(\gamma)\, d\gamma$ is <u>not</u> the probability that γ is the true value. There are two questions of interest. First, how good is the fit? Second, what is the meaning of the ratio of the likelihood functions for the positive and the negative roots? Knowing only the value of the likelihood function for the two roots answers neither of these questions.

In the case of chisquare it is a simple matter to look in a table to find the probability of obtaining chisquare as large or larger than the observed value, and this provides a measure of the goodness of fit. In this case where Poisson statistics were used, such a table was not available. Instead a Monte Carlo technique was used to generate a number of experiments, and for each case the maximum likelihood method was used to determine the two roots. The number of events was not held constant but was allowed to vary statistically about the mean value. As discussed in the text, this procedure showed that the value of the likelihood function for the real data was consistent with a reasonable fit.

Of more interest is what can be learned about the ability of an experiment to determine which of the two roots is the correct value of γ. Suppose an experiment finds a ratio of the likelihood functions, $r_0 = L(+)/L(-)$, and that r_0 is larger than 1. Then the positive root is preferred and a measure of the "goodness of separation" is given by

$$\psi \equiv \frac{P_+(r_0)}{P_-(r_0)}$$

where $P_+(r_0)$ is the probability of observing a value $r \leq r_0$ if the positive root is the true value, and $P_-(r_0)$ is the probability of observing a value $r \geq r_0$ if the negative root is the true value.

To further investigate the properties of P(r), a series of three experiments was generated by the Monte Carlo method discussed above. All were generated assuming a value of $\gamma = .3$. The background generating function had the same shape as the observed background from the out-of-time region of the ΔT spectrum. Table C-I shows the number of radiative decay and background events and the number of experiments performed for each of the three series. Also shown in the table is $P_+(r_0)$, the probability of observing a value of $r \leq r_0$. The error quoted was determined from binomial statistics.

In the case of this experiment, $r_0 = .75$ gives a value of $\psi = .1/.3$ where we have interpolated between P(1.0) and P(1.5) and have made the reasonable assumption that $P_+(r) = P_-(1/r)$. The negative root seems to be about 3 times more probable than the positive value, although this is clearly not a conclusive separation of the roots.

The data in Table C-I shows what can be expected in terms of root separability for experiments with less than 500 events. For each case there is a significant probability of observing a value $r < 1$. This means that for r between 1 and 5 there is a good chance that the observed distribution was generated by a negative value of γ. But out of the 100 experiments generated there was no observation of a value of $r < .2$. Thus for $r > 5$ one could say with confidence that the observed distribution was indeed generated by the positive root. The probability of observing $r > 5$ is largest for the series with 400 events, and this is where the advantage of a larger number of events comes in.

It is clear that for an experiment with less than 500 events there is a serious possibility that a value of r will be produced that will make the roots indistinguishable. This probability will decrease as the number of events increases. This limited analysis does not indicate how many events would be required to separate the roots with 90% confidence. This would be the task of a new experimenter using the parameters of his apparatus. It is certainly more than 500 events.

Table C-I. Table of values for $P_+(r_0)$ as a function of r_0 for three different series of experiments.

r_0 \ $P_+(r_0)$	Series #1 40 experiments 110 radiative decay events 67 background events	Series #2 40 experiments 221 radiative decay events 137 background events	Series #3 20 experiments 440 radiative decay events 160 background events
.2	.0	.0	.0
.5	.05 ± .03	.025 ± .025	.05 ± .05
.75	.15 ± .06	.10 ± .05	.15 ± .08
1.0	.225 ± .07	.20 ± .06	.15 ± .08
1.5	.40 ± .08	.325 ± .07	.2 ± .09
2.0	.60 ± .08	.425 ± .08	.2 ± .09
3.0	.725 ± .07	.50 ± .08	.35 ± .11
4.0	.825 ± .06	.575 ± .08	.35 ± .11
5.0	.875 ± .05	.675 ± .07	.40 ± .11
6.0	.925 ± .04	.70 ± .07	.40 ± .11
8.0	.95 ± .03	.80 ± .06	.65 ± .11
10.0	.95 ± .03	.85 ± .06	.75 ± .10
12.0	.95 ± .03	.90 ± .05	.80 ± .09
16.0	.975 ± .02	.95 ± .03	.85 ± .08
20.0	1.00	.95 ± .03	.90 ± .07

D. Momentum Determination

As mentioned in the text, polynomial approximations were used to determine whether a combination of sparks merited orbiting and to provide an initial approximation for the free parameters. The polynomials are of the following form

$$P(r,s,t) = \sum_{i=0}^{2} \sum_{j=0}^{2} \sum_{k=0}^{2} A_{ijk}\, r^i s^j t^k \qquad \text{(D1)}$$

where r, s, and t are 3 spark chamber coordinates and A_{ijk} is the coefficient. P can be the momentum, the x position in chamber 1, the x position in the stopping hodoscope, or the starting angle. In order to determine the coefficients, 1000 tracks through the spectrometer were generated by Monte Carlo method. A variable metric minimization routine was used to fit the A_{ijk} using the known values of P, r, s, and t. The momentum polynomial is of the form $P_1(X_2,X_3,X_4)$ where X_i is the X coordinate of the i^{th} chamber. The X position in chamber 1 is given by $P_2(X_2,X_3,X_4)$, and the starting position is given by $P_3(X_1,X_2,X_3)$. The momentum must be between 40 and 90 MeV; the X_1 position must be within .5 inch of the measured location, and the starting position is required to be within the hodoscope or else the particular combination of sparks is rejected as a possible trajectory.

The Y (vertical) positions in chamber 1 and the hodoscope are predicted assuming the vertical path of the track is a straight line using the coordinates of chamber 2 and 4. The predicted position in chamber 1 is required to be within .6 inch of the actual value. The

requirement on the vertical coordinate at the hodoscope is very loose; the track may be as much as 1.5 inches above or below the edge of the hodoscope.

Figs. 25a and 25b show histograms of the difference between predicted and fitted values for the momentum polynomial and the X_1 polynomial. If the spark combination passes the above cuts, it is orbited.

The χ^2 for the orbit is written as

$$\chi^2 = \sum_{i=1}^{4} \frac{1}{\sigma^2} \left((SX_i - TX_i)^2 + (SY_i - TY_i)^2 \right) \qquad (D2)$$

where S_i and T_i are the spark location and the predicted orbit position in the i^{th} chamber. σ is the error in position determination and is equal to .1 inch for all chambers. The orbit is determined uniquely by 6 parameters: XO, YO, ZO and PX_0, PY_0, PZ_0 which are the starting position and momentum respectively. We can set ZO arbitrarily to be the plane through the center of the hodoscope, so we are left with 5 parameters. The initial guess for X_0,Y_0 and the momentum magnitude is obtained by using the approximations discussed above. All that remains is to determine the two starting angles:
azimuthal angle θ (from the vertical axis) and the polar angle ϕ (in the X-Z plane). The initial value of θ is determined by a simple linear approximation using the information in chambers 1 and 2. ϕ is determined by the polynomial $P_4(X_2,X_3,X_4)$.

If we relabel our 5 parameters as U_i i=1,5 then to minimize χ^2 we must solve the equations

$$0 = \frac{\partial \chi^2}{\partial Uj} = \sum_{i=1}^{4} \frac{1}{\sigma^2} \left(\Delta X_i \frac{\partial TX_i}{\partial U_j} + \Delta Y_i \frac{\partial TY_i}{\partial U_j} \right) \quad j = 1,5 \qquad \text{(D3)}$$

where $\Delta X_i = (SX_i - TX_i)$. A Newton-Raphson iteration process is used to find an approximate solution.

We briefly review this method for a one dimensional problem. Let a denote the approximate value of the desired root, and let h be the correction required to give the exact value of the root, x, so that

$$x = a+h$$

The equation $f(x) = 0$ becomes $f(a+h) = 0$. Expanding in a Taylor's series we have

$$f(a+h) - f(a) - hf'(a) - \frac{h^2}{2} f''(a + \theta h) = 0 \qquad \text{(D4)}$$

where $0 \leqslant \theta \leqslant 1$.

Since h is small we neglect second order terms and are left with

$$f(a) + hf'(a) = 0 \ . \qquad \text{(D5)}$$

This leads to the simple relation $h_1 = - \frac{f(a)}{f'(a)}$. The improved value of the root is $a_1 = a+h_1$.

Adapting this method to our multi-parameter problem we have the 5 equations

$$\frac{\partial \chi^2 \ (U^{k-1})}{\partial U_i} + \sum_{j=1}^{5} h_j \frac{\partial}{\partial U_i} \left(\frac{\partial \chi^2 \ (U^{k-1})}{\partial U_i} \right) = 0 \qquad \text{(D6)}$$

where i varies from 1 to 5.

The superscript k-1 is to indicate that for the k^{th} iteration we use the values of U_j obtained from the previous iteration or the

initial guess in the case k = 1. We have 5 equations in 5 unknowns and it is straightforward to solve for h_i. First let us examine the problem of calculating the derivatives.

$$\frac{\partial}{\partial U_j}\left(\frac{\partial \chi^2}{\partial U_i}\right) = \frac{1}{\sigma^2} \sum_{\ell=1}^{4} \left(-\frac{\partial TX_\ell}{\partial U_j}\frac{\partial TX_\ell}{\partial U_i} + \Delta X_\ell \frac{\partial^2 TX_\ell}{\partial U_j \partial U_i} - \frac{\partial TY_\ell}{\partial U_j}\frac{\partial TY_\ell}{\partial U_i} + \Delta Y_\ell \frac{\partial^2 TY_\ell}{\partial U_j \partial U_i} \right) . \qquad (D7)$$

The derivative with respect to U_i is calculated numerically by repeating the orbit with U_j replaced by $U_j + dU_j$. Six orbits are required to calculate the 5 first derivatives. The major cost in this program is the orbiting; the cost would become prohibitive if it was necessary to compute the second derivatives $\frac{\partial^2 TX_\ell}{\partial U_i \partial U_j}$ for all i and j. To first order the track position in the i^{th} chamber will be linearly related to the starting position and to the starting momentum since the Lorentz equation is linear in P. We neglect the second derivatives and are left with the 5 equations

$$\frac{1}{\sigma^2} \sum_{\ell=1}^{4} \left(\Delta X_\ell \frac{\partial TX_\ell}{\partial U_i} + \Delta Y_\ell \frac{\partial TY_\ell}{\partial U_i} \right) + \frac{1}{\sigma^2} \sum_{j=1}^{5} h_j \sum_{\ell=1}^{4} \left(-\frac{\partial TX_\ell}{\partial U_j}\frac{\partial TY_\ell}{\partial U_i} - \frac{\partial TY_\ell}{\partial U_j}\frac{\partial TY_\ell}{\partial U_i} \right) = 0 \qquad (D8)$$

where i = 1,5.

For each track a maximum of 5 iterations are performed. The program will exit early if χ^2 is less than 0.5, if χ^2 has not changed

from the previous iteration, or if a track crosses one of the boundaries of the apparatus.

The actual orbiting is done by the subprogram ORBIT.[41] The equations of motion are integrated using a fourth order Adams-Bashforth method. Since this method is not self-starting, a fourth order Runge-Kutta method is used for the first 4 steps.

E. Monte Carlo Calculation of Acceptance

The Monte Carlo program was used to determine the acceptance of the apparatus and to observe the effect of the acceptance and π-decay kinematic distribution on the measured parameters. The exact form of the program depended on the problem under study, but the basic structure remained the same.

I. Event generation

1. Choose a vertex position in the stopping hodoscope.

2. Choose a photon direction. If it does not hit the photon counter, it is a nonaccepted event, and the program returns to step 1.

3. Choose photon energy and electron energy using theoretical distribution (equation 6) and the input value of γ.

4. Calculate the photon-electron opening angle from the photon and electron energy.

5. Determine electron energy loss due to depth in the stopper.

6. Compute the "measured" value of the electron momentum based on the input value of momentum resolution.

7. Determine "measured" value of opening angle assuming that the shower will be placed at the center of the block that was hit.

8. Using subprogram ORBIT,[41] trace the path of the electron through the spark chambers. If the positron hits no boundaries and hits E1 and either E2 or E3, it is considered an accepted event.

II. The acceptance

The above event generation determines the overall acceptance for a particular value of γ. It is the sequence used to determine the edge effects in the Cherenkov counter and to study its energy resolution. For the analysis program we need the acceptance for each bin in the p,θ plane. For this purpose step 3 is eliminated since p and θ are fixed values. Steps 5, 6, and 7 are also eliminated. The energy loss is handled separately by the analysis program as is the momentum and angular resolution. For each bin 100 events are generated; using this value of the acceptance the program calculates how many more events it needs for a statistical error of 2%.

III. Stopping distribution

The parent distribution used as input to step 1 was determined in two parts. The Winnow program was used to look at muon decay; in particular to determine the position of the muon in the stopping hodoscope. The muons were selected by requiring that positron momentum be between 40 and 50 MeV and χ^2 for the momentum fit less than 4. This gave a large number of events with essentially no background. The resultant distribution was the image of the true spectrum as seen by the spectrometer.

We still needed to unfold the muon decay acceptance. To do this we used the Monte Carlo program to measure the acceptance for muon decay as a function of position in the stopper. We found that there was a 5% difference in the overall acceptance for radiative decay when the

stopping distribution is used with and without the muon acceptance correction.

IV. Errors

Here we discuss only the version used to determine acceptance as a function of P and θ. The statistical error of 1% per bin is completely negligible compared to other errors. Another source of error is the photon counter path length calculation. This is discussed in Appendix B. The error in the acceptance due to the uncertainty of the spatial distribution of stopping pions was determined by studying the effect of using distributions obtained from different samples of the data. This error was found to be $\pm$ 1.%.

ACKNOWLEDGMENTS

I wish to express my appreciation to all who contributed to the completion of this study.

I am especially grateful to my research advisor, Professor Victor Perez-Mendez, for the instruction and guidance I enjoyed as his student.

I am indebted to Drs. Al Stetz and Jim Carroll for their work in the design and running of this experiment and their guidance during the data analysis and writing of this thesis.

The help of Dr. Barry Berman, Lawrence Livermore Laboratory, in calibrating the photon counter is gratefully acknowledged.

I wish to thank my fellow graduate students from UCLA, Mohamed Nasser and Dr. Nara Chirapatpimol, for their assistance while on the floor of the cyclotron, Dr. M. Dixit for his help during the early stages of this experiment, and Dr. George Igo for collaborating with our group on this work.

I also thank Jimmy Vale and the 184-inch cyclotron crew for their efficient operation of the machine, Joe Love and Lloyd Belknap for maintaining the data buffer, Alpha-63, and the staff of the Technical Information Division for inking the drawings and typing the final manuscript.

Finally, I am sincerely grateful to my wife, Mary, for her patience and support during my years as a graduate student.

This report was done with support from the U. S. Energy Research and Development Administration.

REFERENCES AND FOOTNOTES

1. S. Lokanathan and J. Steinberger, Phys. Rev. 98, 240(A) (1955).

2. S. B. Treiman and H. W. Wyld Jr., Phys. Rev. 101, 1552 (1956).

3. V. G. Vaks and B. L. Ioffe, Nuovo Cimento 10, 342 (1958).

4. R. P. Feynmann and M. Gell-Mann, Phys. Rev. 109, 193 (1958).

5. N. Cabibbo, Nuovo Cimento 11, 837 (1959).

6. D. Neville, Phys. Rev. 124, 2037 (1961).

7. P. Depommier, J. Heintze, C. Rubbia, and V. Soergel, Phys. Lett. 7, 285 (1963); V. Soergel, Proceedings of the SIN Summer School, Leysin (1969). There has been some confusion as to whether these authors include the Cabibbo angle in their expressions for the weak hadronic currents. An analysis of their numerical values shows that they include the Cabibbo angle in their value for G.

8. M. Gell-Mann, Phys. Rev. 125, 1067 (1962).

9. S.L. Adler, Phys. Rev. 140B, 736 (1965).

10. S. Weinberg, Phys. Rev. Lett. 18, 507 (1967).

11. Because of the controversy concerning the existence of the A_1 meson, the Particle Data Group[18] quotes no error on the mass of the A_1. This ratio and error were obtained by averaging the twenty experimental measurements of the A_1 mass included in the Data Card Listings by the Particle Data Group.

12. M. Gell-Mann and Y. Ne'eman, The Eightfold Way, Benjamin (1964).

13. W. Kummer and J. Kuti, Nuovo Cimento 45, 242 (1966).

14. P.S.L. Boothe, L.J. Carroll, G.R. Court, R.G. Johnson and J.R. Wormald, Proc. Phys. Soc. 86, 1317 (1965).

15. S. Bludman and J. Young, Phys. Rev. 118, 602 (1960); S. Brown and S. Bludman, Phys. Rev. 136, B1160 (1964); M.G. Smoes, Nucl. Phys. B20, 237 (1970); D. Bardin and S. Bilen'kii, Yad Fiz 16, 557 (1972) [Sov. J. of Nucl. Phys. 16, 311 (1972)]; see Refs. 3, 6.

16. R.E. Marshak, Riazuddin, C.P. Ryan, Theory of Weak Interactions in Particle Physics, Wiley, Rochester (1969); Riazuddin and Fayyazuddin, Phys. Rev. 171, 1428 (1968).

17. V. F. Muller, Z. Phys. 173, 438 (1963), P. de Baenst and J. Pestieau, Nuovo Cimento, 53A, 137 (1968). See also Reference 5.

18. Rosenfeld et al, Rev. of Mod. Phys. 48 1 (1976).

19. N. J. Carron and R. L. Schult, Phys. Rev. D1, 3171 (1970).

20. K. Kawarabayashi and M. Suzuki, Phys. Rev. Lett. 16, 255 (1966); Riazuddin and Fayazuddin, Phys. Rev. 147, 1071.

21. P. De Baenst and J. Pesteau, Nuovo Cimento 53A, 407 (1968); N. Cabibbo, L. Maiani, and G. Preparata, Phys. Lett. 25B, 31 (1967).

22. J. Gregor, Ph.D. Thesis, Columbia University, (1974), (unpublished).

23. T. Das, V. S. Mathur, S. Okubo, Phys. Rev. Letters 19, 1067, (1967).

24. H. Schitzer and S. Weinberg, Phys. Rev. 164, 1828 (1967).

25. J. S. Vaishya, Phys. Rev. 173, 1757, (1968); the results of Refs. 25, 26, 27, and 29 have been recalculated using $T_{\pi}o = 0.828 \times 10^{-16}$ sec.

26. T. Das, V. S. Mathur, S. Okubo, Phys. Rev. Letters 19, 859, (1967).

27. S. Brown and G. West, Phys. Rev. 168, 1605 (1968), S. Brown and G. West, Phys. Rev. Letters 19, 812, (1967), S. Brown, private communication (1973).

28. Fayyazuddin and Riazuddin, Nuovo Cimento 54, 520 (1968).

29. V. S. Berezinskii, Yad. Fiz. 8, 1208 (1968). (Sov. J. Nucl. Phys. 8, 700, (1969)).

30. C. W. Akerlof et al., Phys. Rev. 163, 1482 (1967).

31. R. Diebold, XVI International Conference on High Energy Physics, Batavia, Vol. 3 (1972).

32. R. T. Deck, Phys. Rev. Letters 13, 169 (1964).

33. G. Ascoli et al, Phys. Rev. D 7, 669 (1973).

34. D. D. Brayshaw, Phys. Rev. Lett. 36, 73 (1976).

35. F. Scheck and A. Wullschleger, Nucl. Phys. B67, 504, (1973).

36. S. L. Adler, Phys. Rev. 177, 2426 (1969).

37. M. Moreno and J. Pestieau, Phys. Rev. D 13, 175 (1976), M. Moreno, Ph.D. Thesis, Universidad Nacional Autonoma de Mexico, 1976 (unpublished), J. Pestieau, Private communication (1976), M. Moreno, Private communication (1976).

38. M. Gell-Mann and M. Levy, Nuovo Cimento 16, 705 (1960).

39. V. Perez-Mendez and J. M. Pfab, NIM 33, 141 (1965); R. L. Grove, V. Perez-Mendez and R. Van Tuyl, NIM 70, 306 (1969).

40. F. Gey, Program SPARKY, Lawrence Berkeley Laboratory Computer Center Report (1972) unpublished.

41. D. C. Snyder, Program ORBIT, Lawrence Berkeley Laboratory Computer Center Report (1966) unpublished.

42. D. R. Edgington, K. McDonald, M. L. Griss, and G. C. Fox, California Institute of Technology, CTSL Internal Report No. 63 (1972) unpublished.

43. C. Orth, Program NEWCASP, University of California Sciences Laboratory Internal Memo NFD No. 234 (1976) unpublished.

44. K. McDonald, CALT-68-321, California Institute of Technology (1971) unpublished .

45. J. D. Bjorken and S. D. Drell, Relativistic Quantum Mechanics, McGraw-Hill (1965).

46. J. D. Bjorken and S. D. Drell, Relativistic Quantum Fields, McGraw-Hill (1965).

47. General Electric RTV Type 615 A and B.

48. Q. A. Kerns and R. F. Tusting, Lawrence Radiation Laboratory Report UCRL-10895 (1963).

49. Sober et al, NIM 108, 573 (1973); D. I. Sober, Group Notes GN 72-2, Department of Physics, UCLA (1972).

50. C. A. Heusch, R.V. Kline, C. Y. Prescott, S. J. Yellin, Presented at International Conference on Instrumentation for High Energy Physics, Dubna (1970).

FIGURE CAPTIONS

1. Feynmann diagrams for radiative decay.

2. Feynmann diagram for the vector contribution of the ρ-dominance model.

3. Experimental layout. The coordinate system is indicated.

4a. Differential rate with respect to electron energy for the IB term and the SD term for 3 different values of γ. The kink in the curves at 65 Mev is due to the presence of a 20 Mev threshold for the photon energy.

4b. Differential rate with respect to opening angle for the IB term and the SD term for 3 different values of γ.

5. Electronic logic diagram. D means a discriminator; UD is an updating discriminator; the fan-in's are linear. The summing procedure for the rows and columns of the lead-glass hodoscope is indicated only for the first of each.

6. Spectrum of time differences, ΔT, between positron and photon signals.

7. Number of radiative decay events included as a function of the position of the in-time window. The bin size is .1 ns.

8a. Elapsed time (decay time after stop) distribution for radiative decay events. Smooth curve is a π decay curve with the amplitude fitted to the experimental data.

b. Elapsed time distribution for the background, scaled by R (the ratio of in-time and out-of-time intervals for the ΔT spectrum).

9. Momentum distribution of electrons from muon decay. Smooth curve is the calibration fit. Momentum scales for before and after calibration are shown.

10. Elapsed time spectrum for determining muon contamination in the stopping beam. Data in the peak at T = 0 (between -2ns and 4ns) is not included in the fit.

11. Distribution of the χ^2 of the momentum reconstruction fit for the radiative decay events.

12. Photon detection efficiency of the Cherenkov counter. The outer curves represent the estimated error. The points are the annihilation beam data.

13. Momentum spectrum of electrons from muon decay. The histogram is the observed distribution, while the points are the results of a Monte Carlo calculation.

14. Positron momentum spectrum for the out-of-time events, scaled by R.

15. Opening angle spectrum for the out-of-time events, drawn as for Fig. 14.

16. Positron momentum spectrum of the radiative decay events. Solid curve is a fit for $\gamma = .44$; dashed curve is for $\gamma = -2.38$.

17. Opening angle distribution for the radiative decay events. Curves drawn as for Fig. 16.

18. Likelihood function for the two roots normalized to value at peak of the curve for the positive root.

19. Relationship between γ' as determined from our data and the assumed values of the π^0 lifetime. Data points are measurements of the lifetime with the year performed indicated. Particle Data Group no longer uses the three largest values of T_{π^0} in computing the world average.

20. Photograph showing the construction of the lead-glass hodoscope.

21. Photograph of the light pulser distribution wheel. Both barium titinate and AR-4 lamps are shown.

22a. Pulse height spectrum from cosmic rays for the lead-glass counter.

b. Pulse height spectrum from the "plunger source." The upper trace is the bismuth spectrum, while the lower trace is the AR-4 light pulser spectrum.

23. Experimental layout for photon efficiency calibration.

24a. A histogram of $(k - E)/k$ for the radiative decay events where k is the photon energy predicted by the observed electron momentum and opening angle and E is the photon energy as determined from the pulse height in the Cherenkov counter. The points are the result of a Monte Carlo calculation normalized to the data.

b. Same histogram as for Fig. 24a for the background events.

25a. Difference histogram for the momentum polynomial.

25b. Difference histogram for the X_1 polynomial.

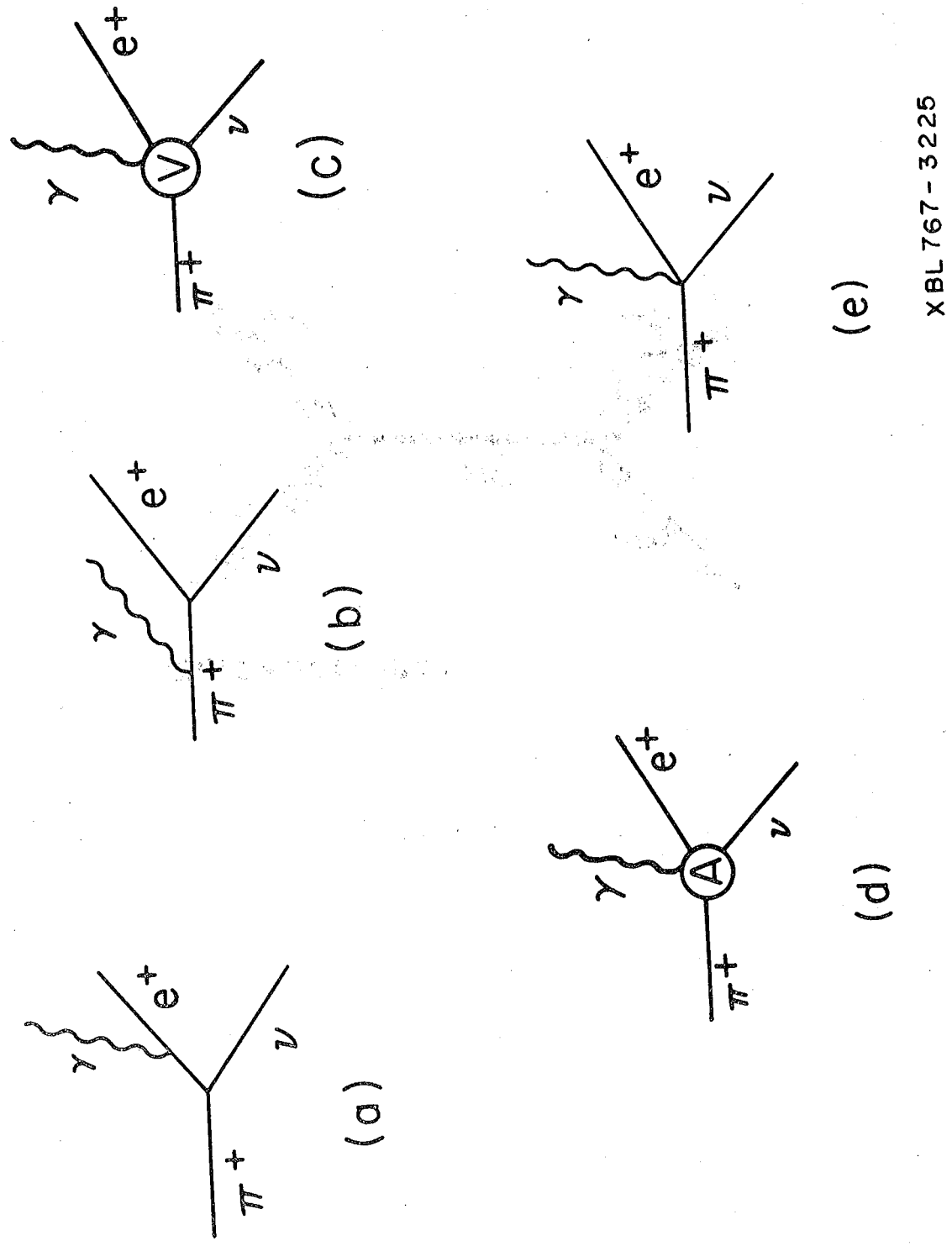

XBL 767-3225

Fig. 1

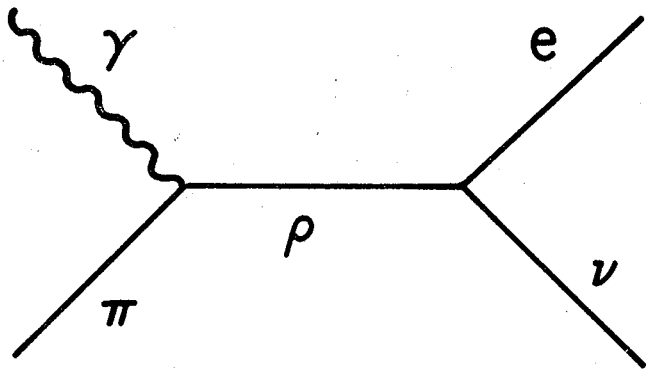

XBL767-3226

Fig. 2

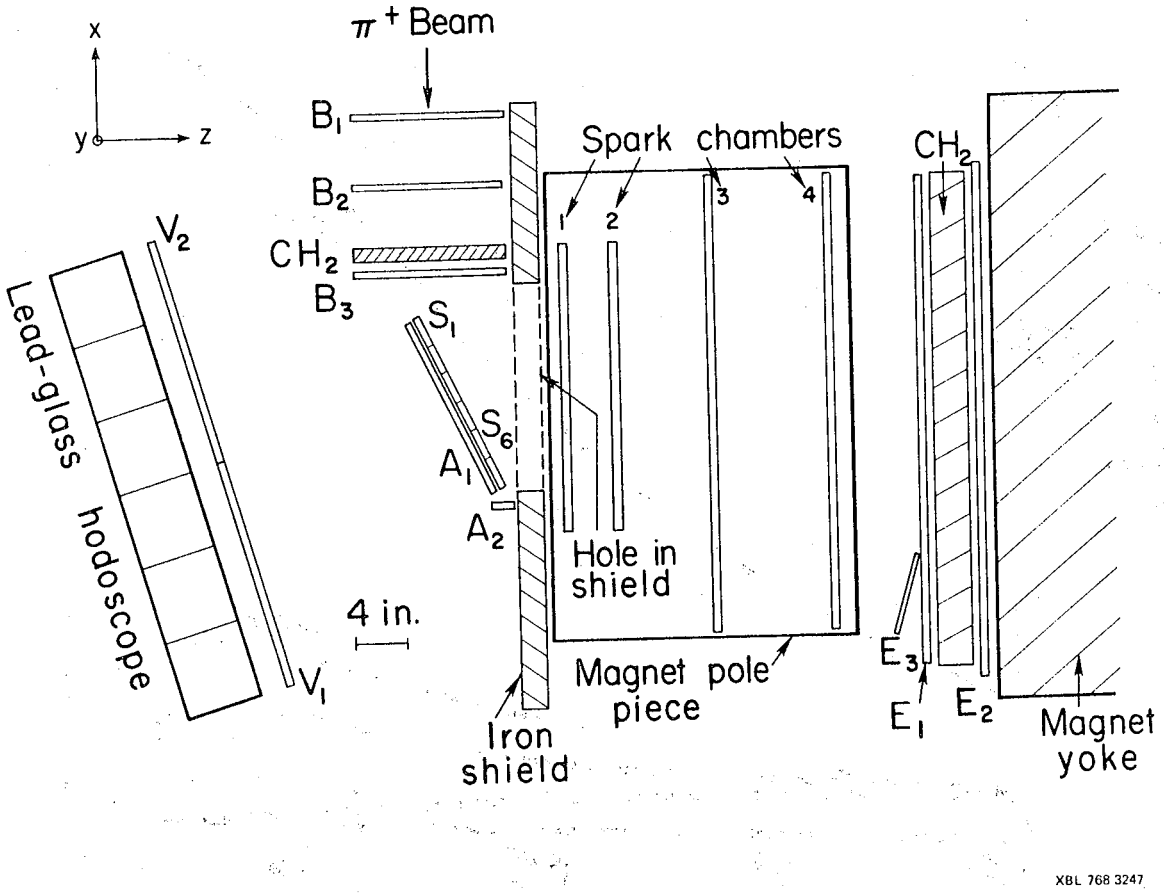

Fig. 3

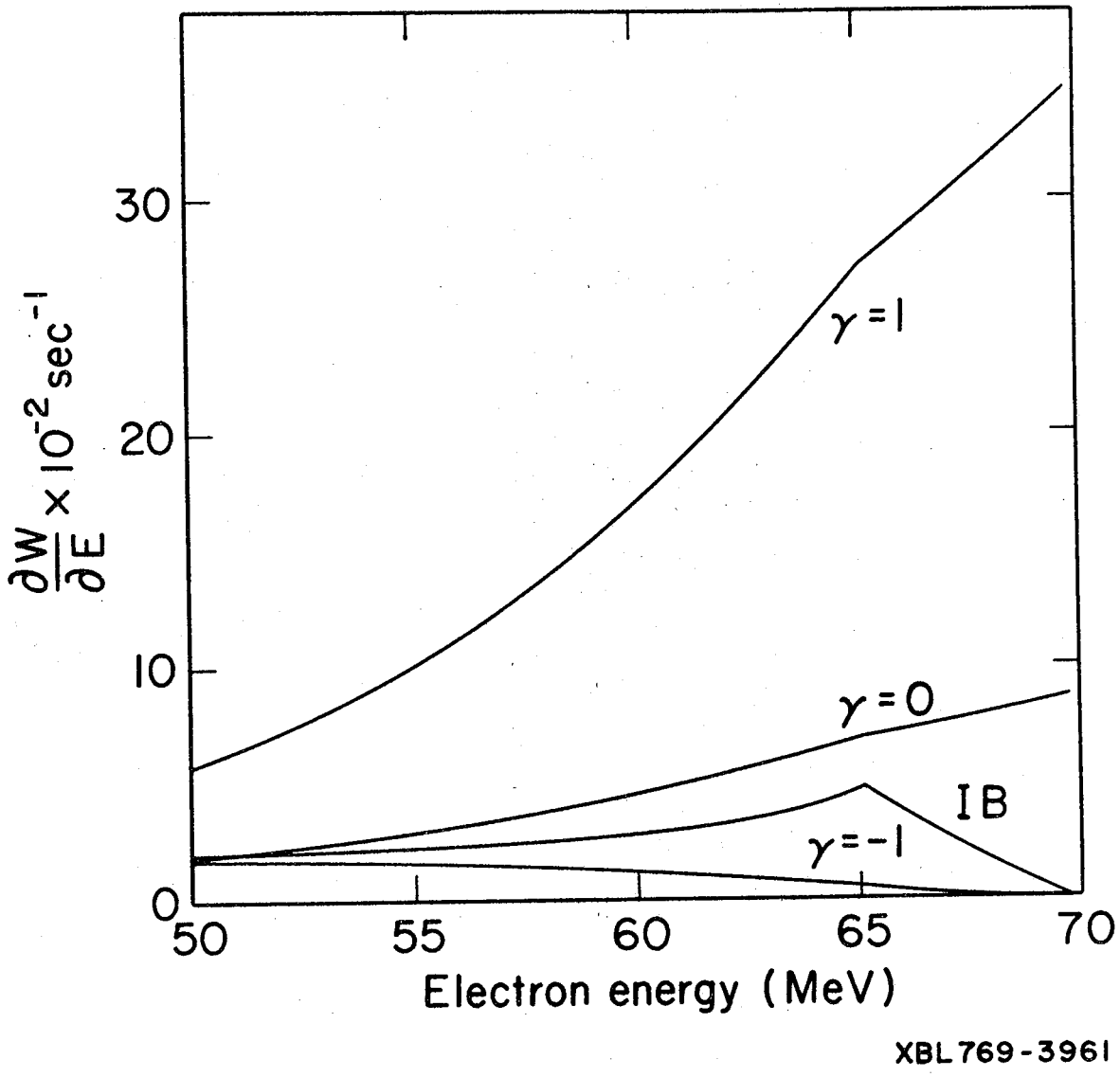
$\frac{\partial W}{\partial E} \times 10^{-2}$ sec^{-1}
30
20
10
0
50
55
60
65
70
Electron energy (MeV)
γ=1
γ=0
IB
γ=-1
XBL769-3961

Fig. 4a

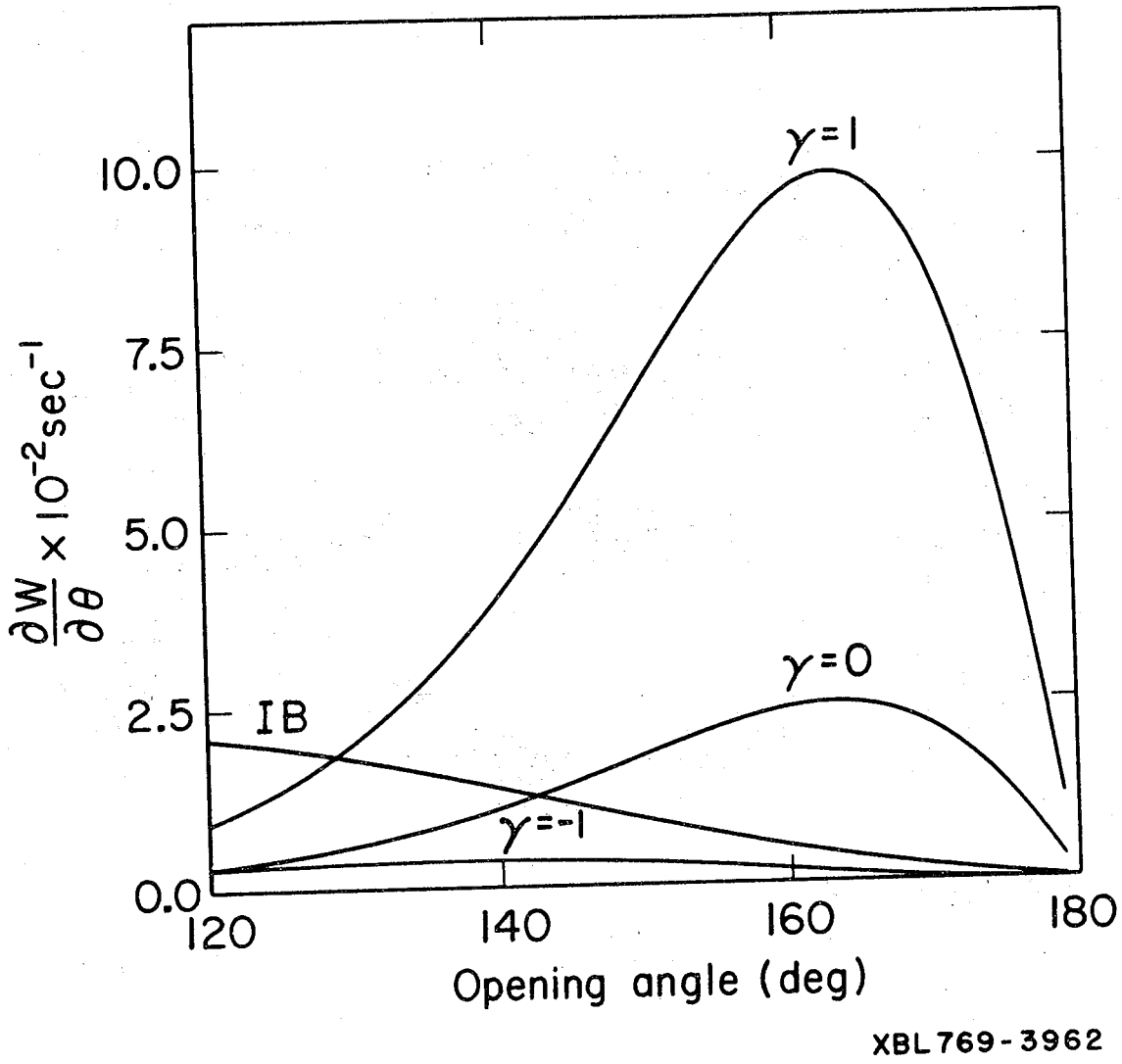

Fig. 4b

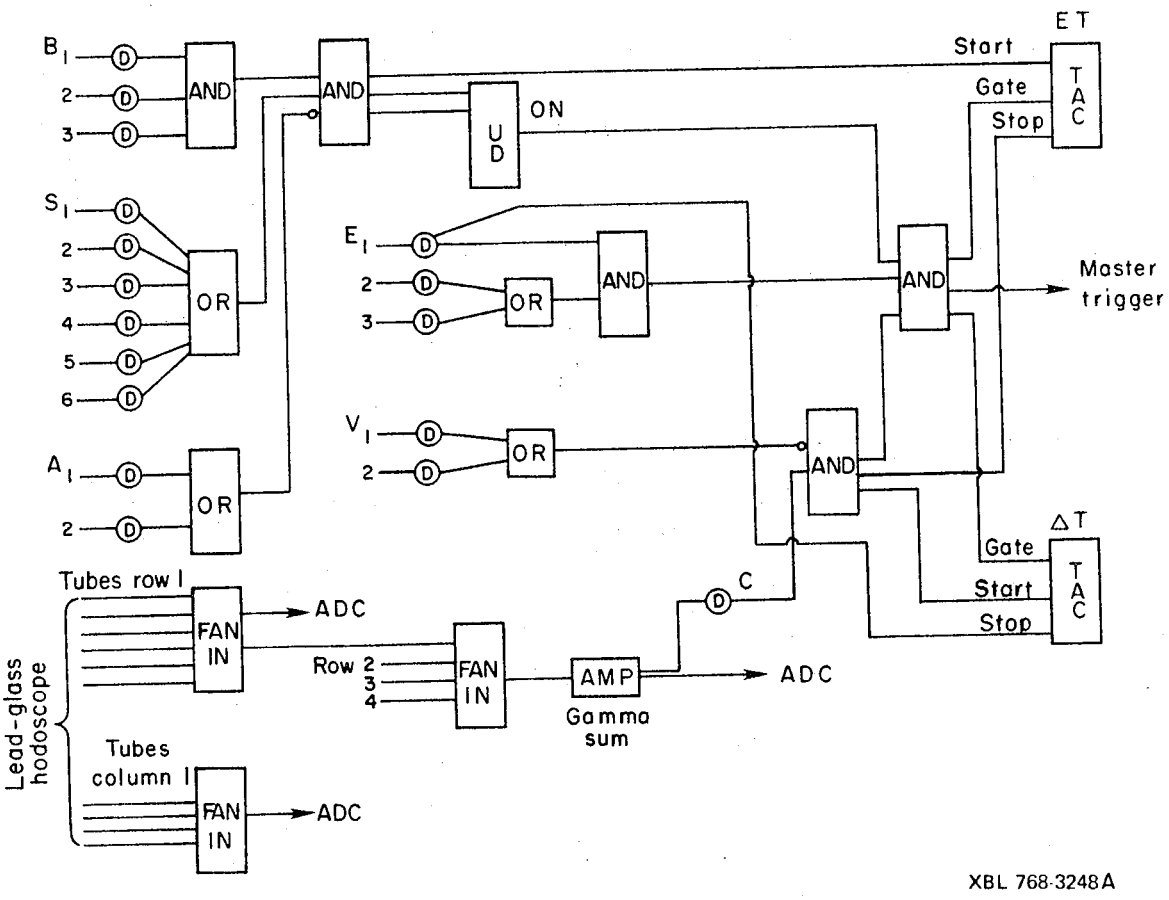
B 1
2
3
AND
AND
U D
ON
Start
Gate
Stop
E T
T A C
S 1
2
3
4
5
6
OR
E 1
2
3
OR
AND
AND
Master trigger
V 1
2
OR
AND
A 1
2
OR
Gate
Start
Stop
Δ T
T A C
Tubes row 1
FAN IN
ADC
C
Row 2
3
4
FAN IN
AMP
ADC
Gamma sum
Lead-glass hodoscope
Tubes column 1
FAN IN
ADC
XBL 768-3248A

Fig. 5

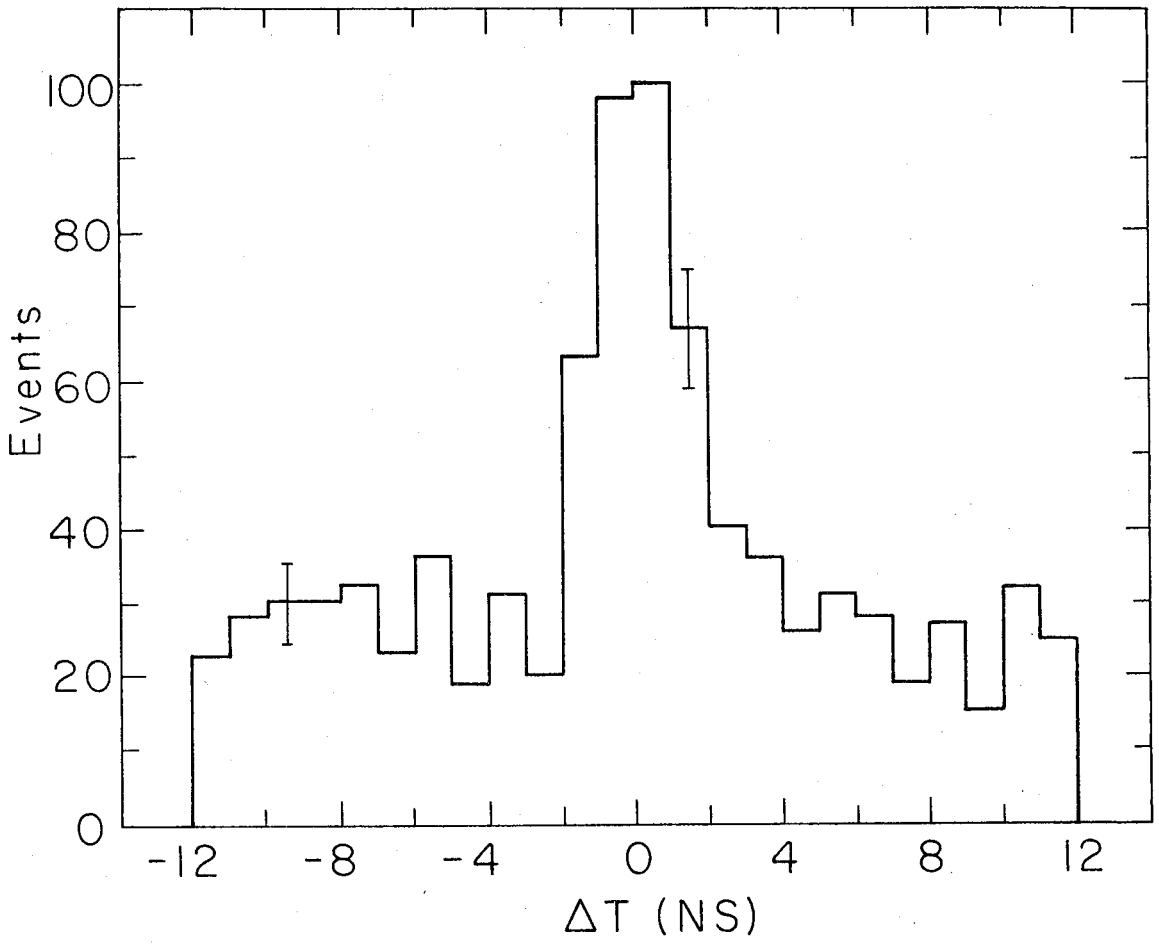

XBL 764-2812

Fig. 6

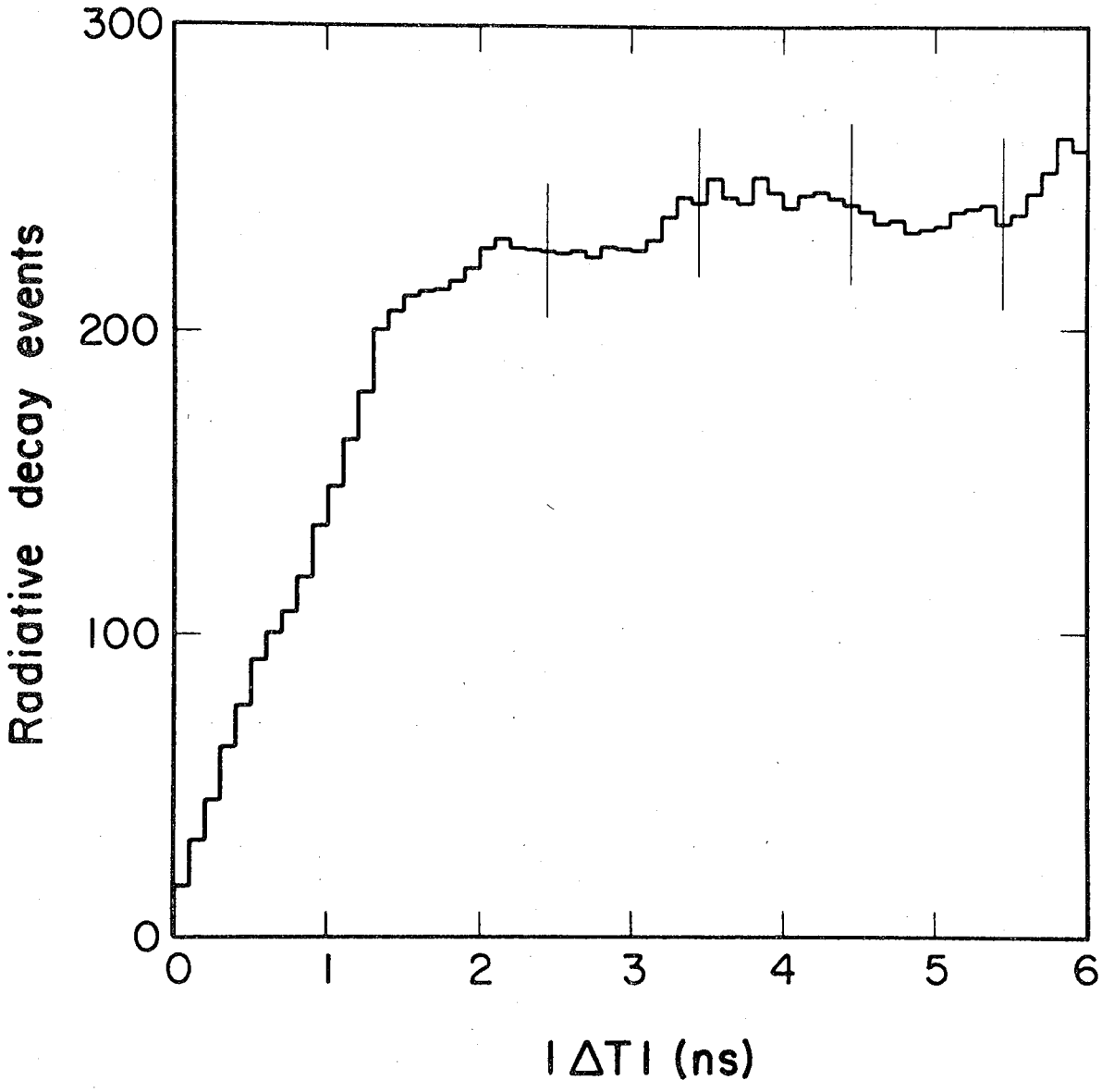

XBL 7612-11137

Fig. 7

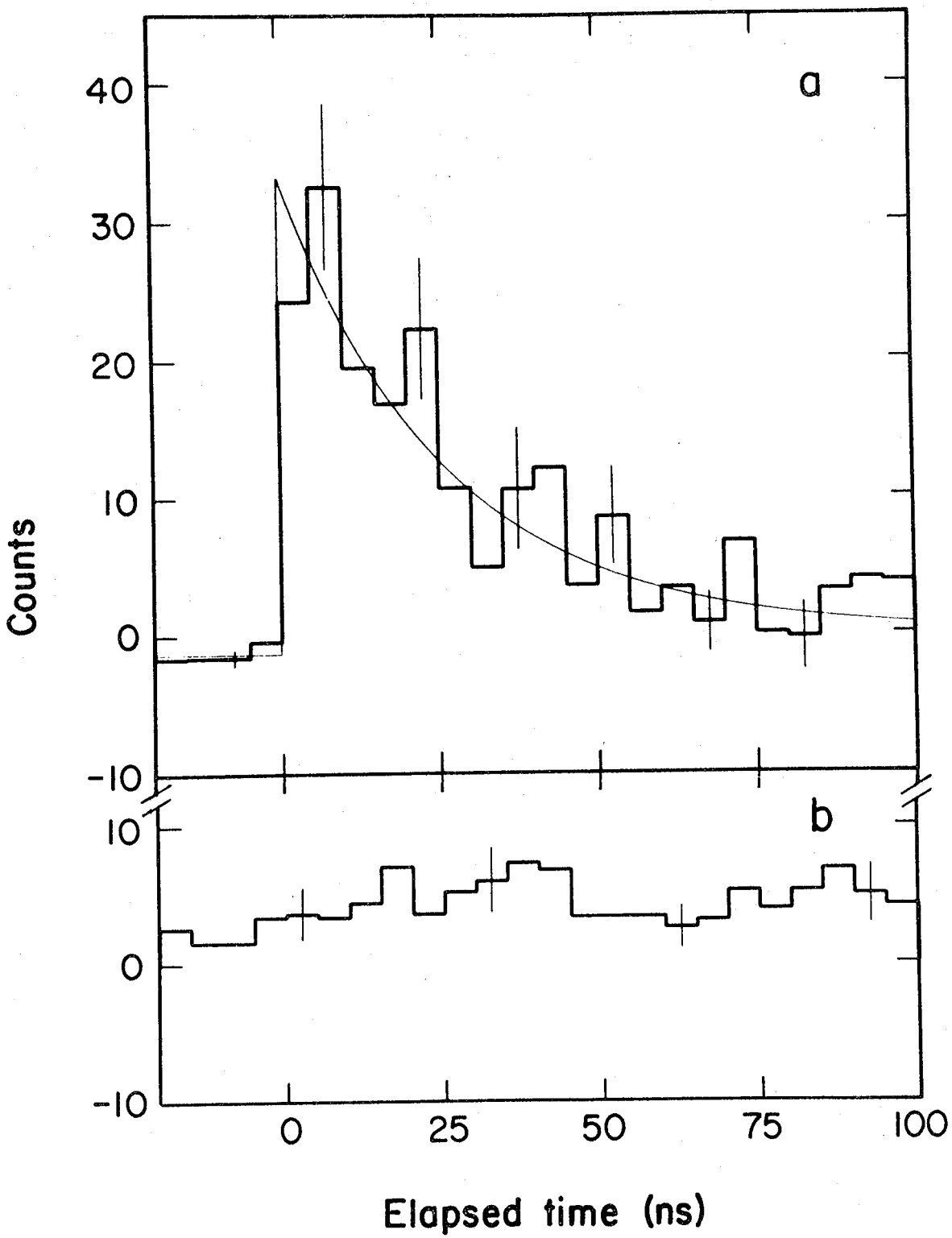

Fig. 8

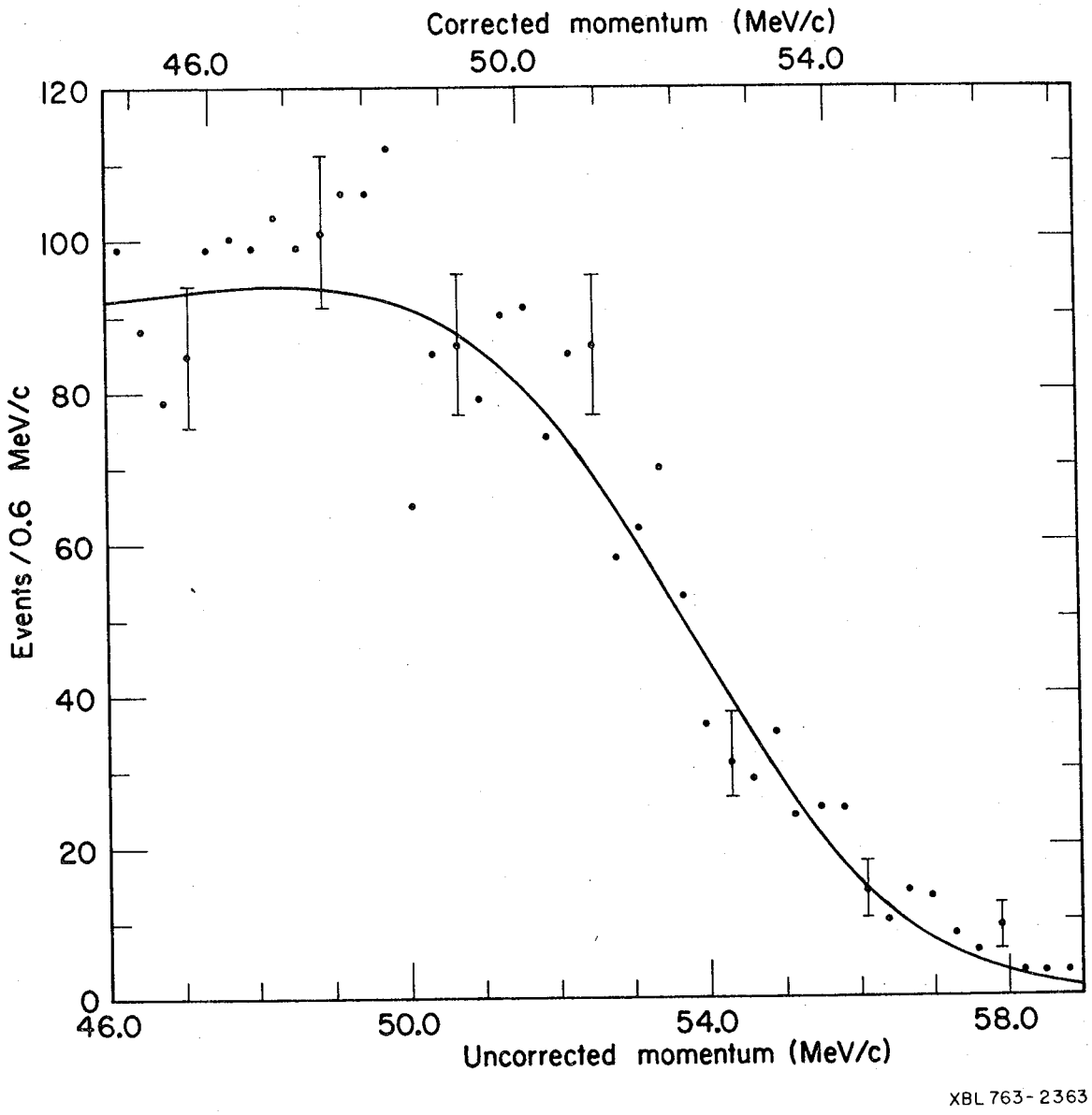
Corrected momentum (MeV/c)
46.0
50.0
54.0
120
100
80
60
40
20
0
Events /0.6 MeV/c
46.0
50.0
54.0
58.0
Uncorrected momentum (MeV/c)
XBL 763-2363

Fig. 9

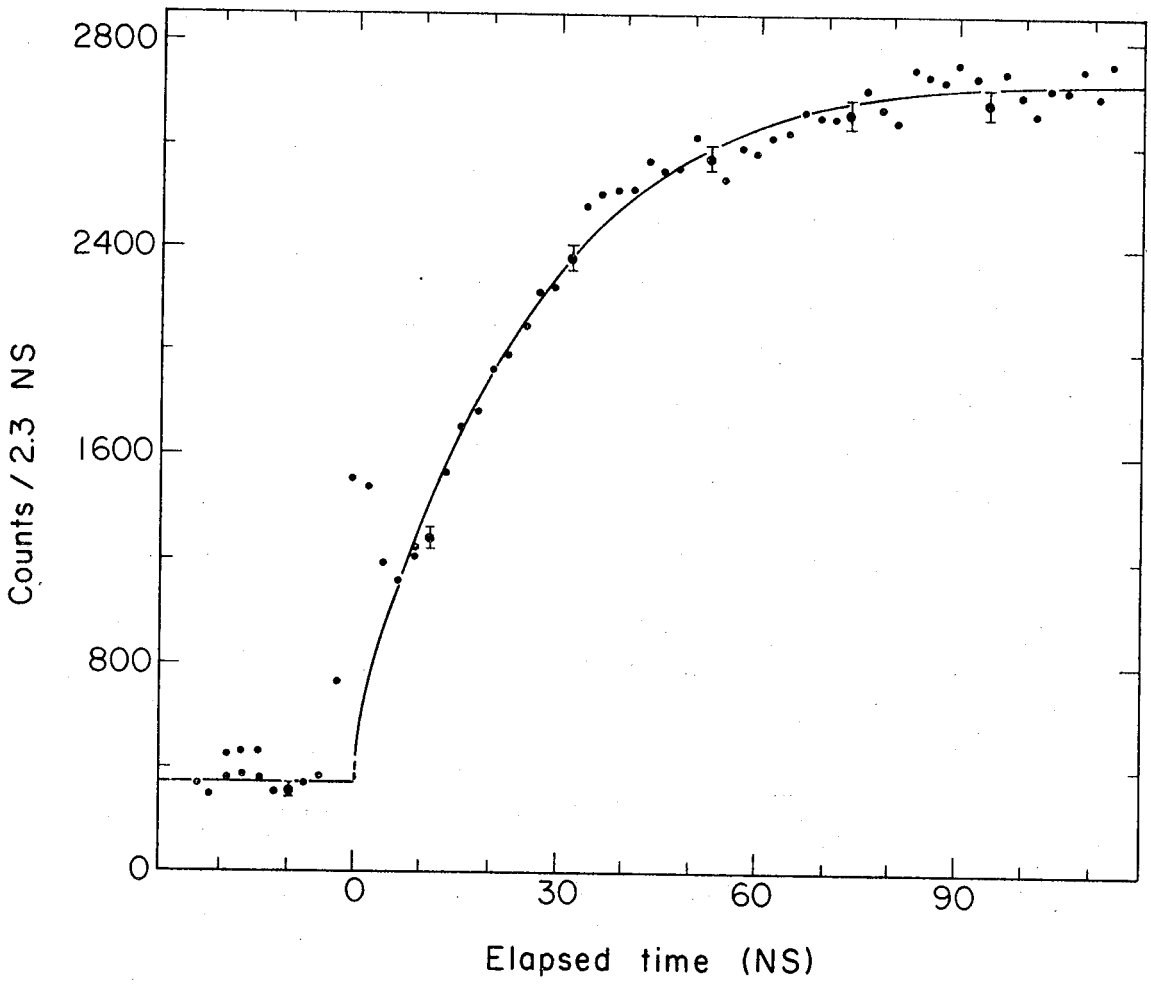

Fig. 10

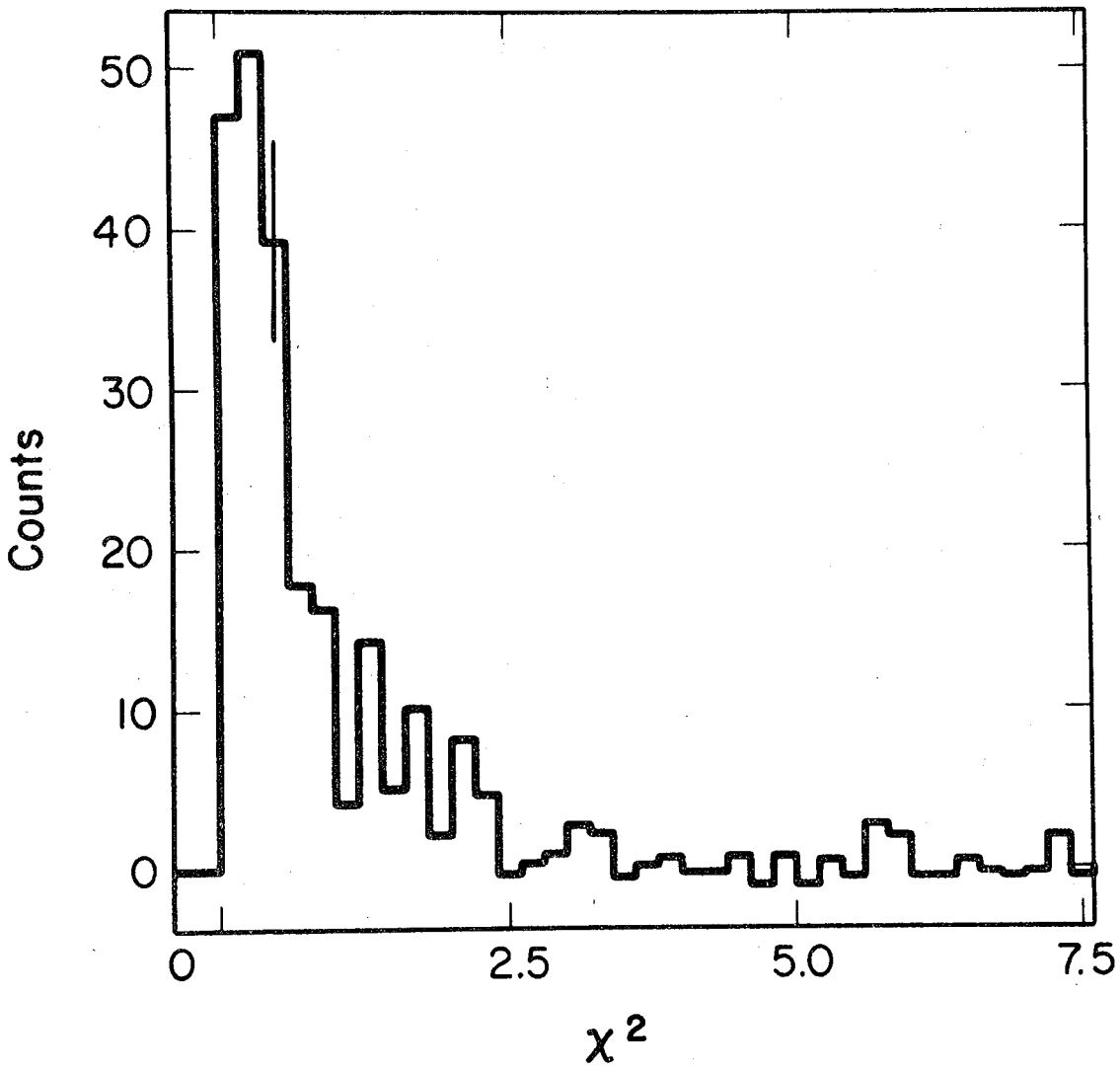

Fig. 11

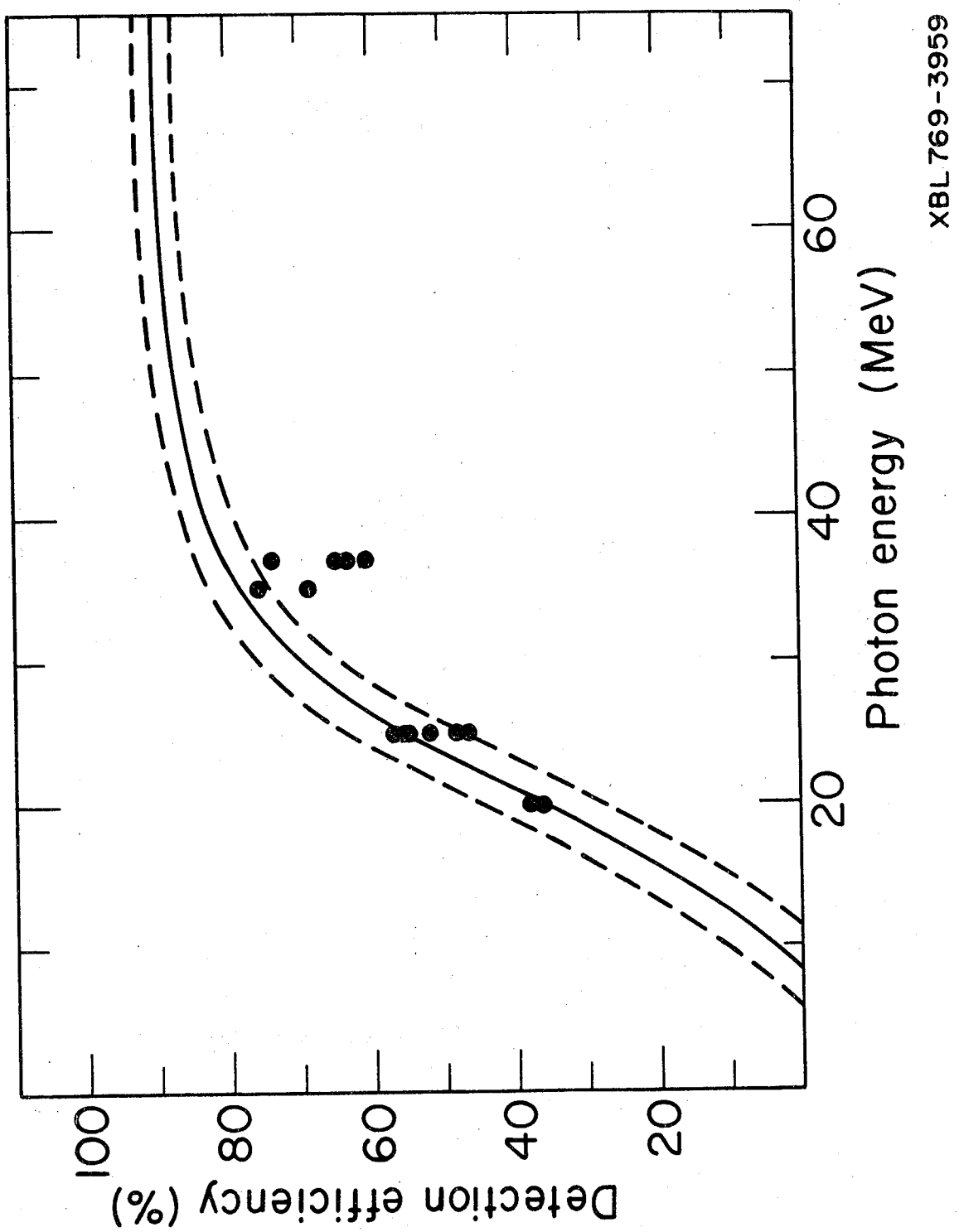

Fig. 12

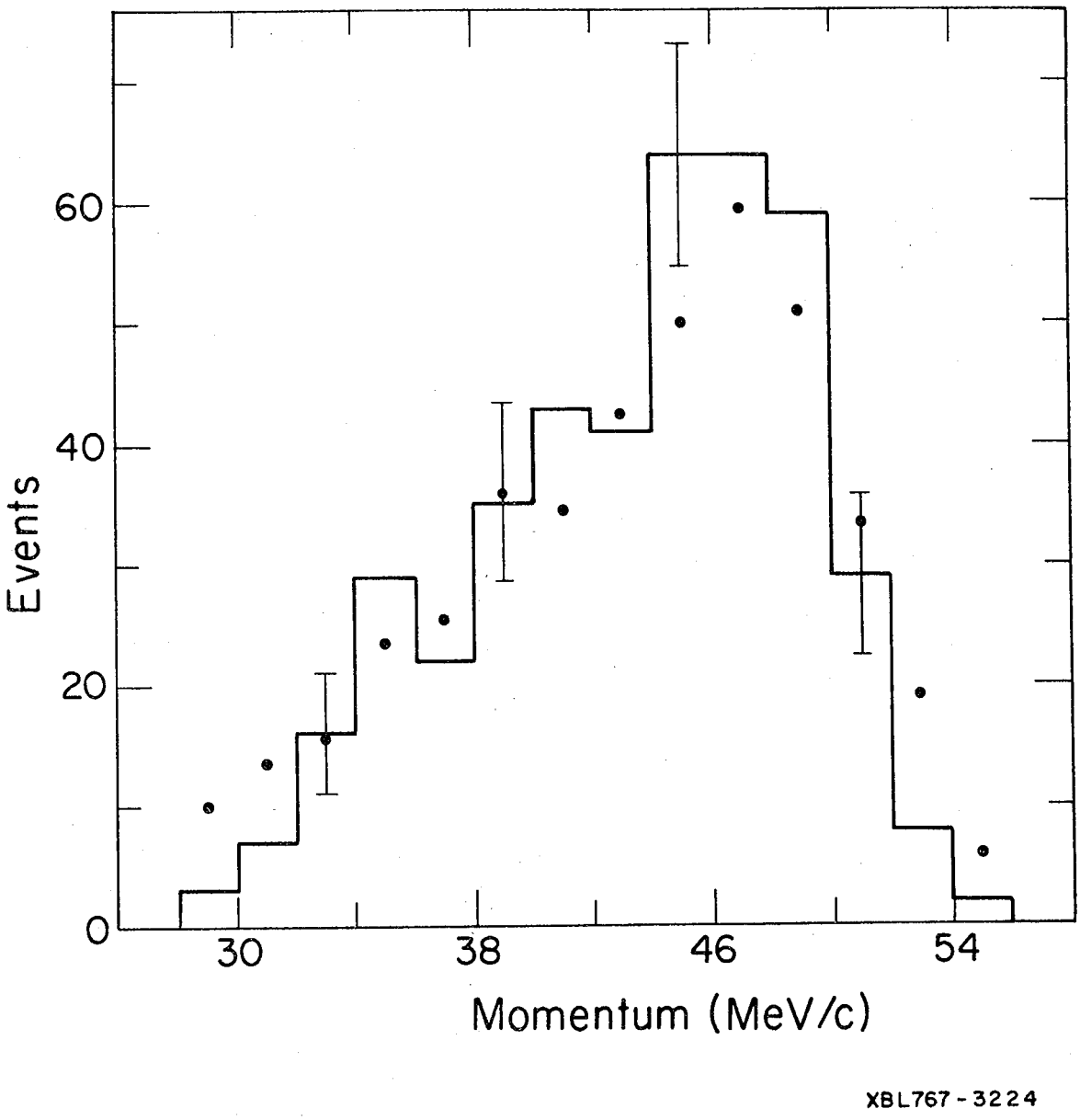

Fig. 13

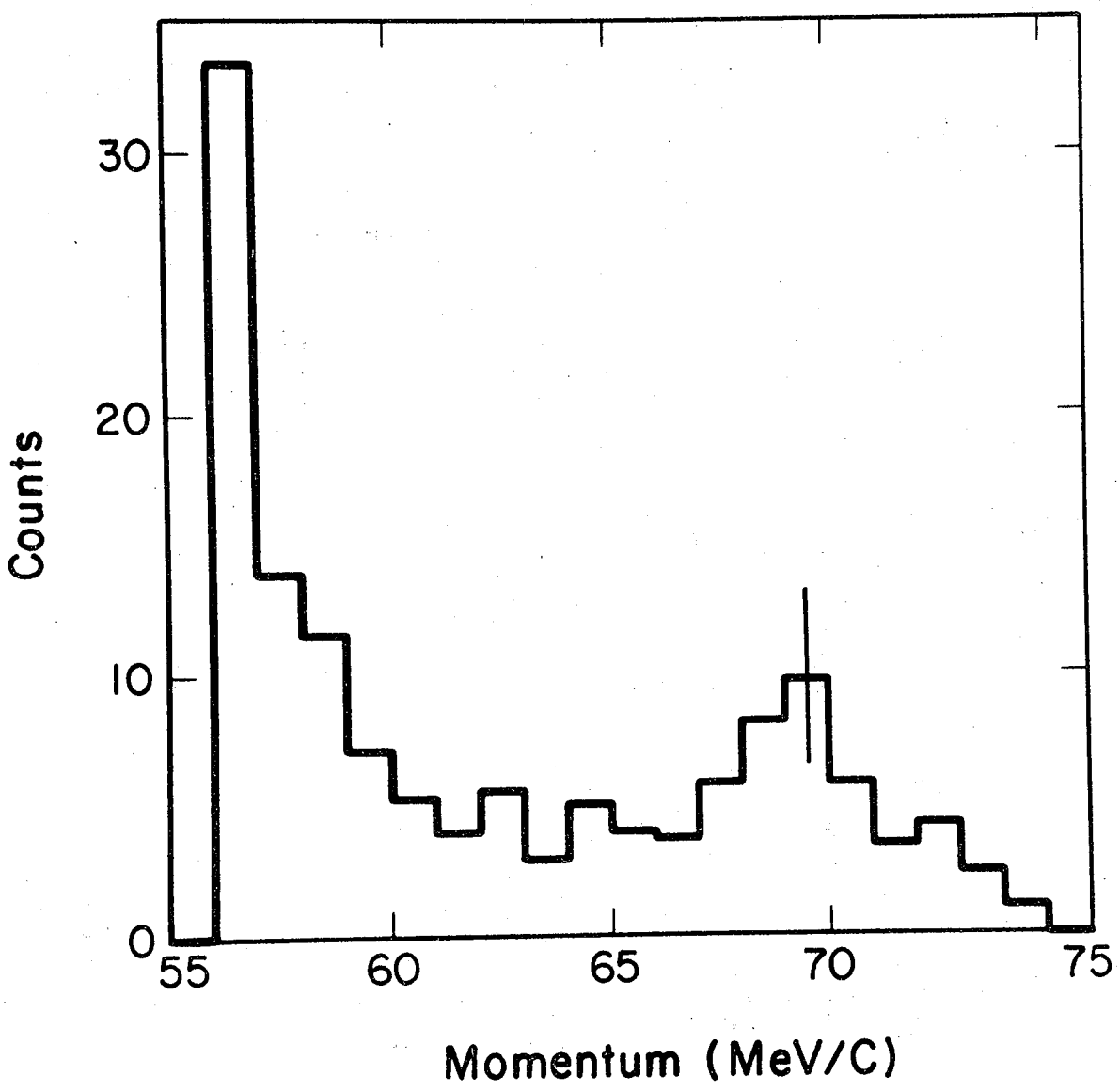

XBL 7612-11141

Fig. 14

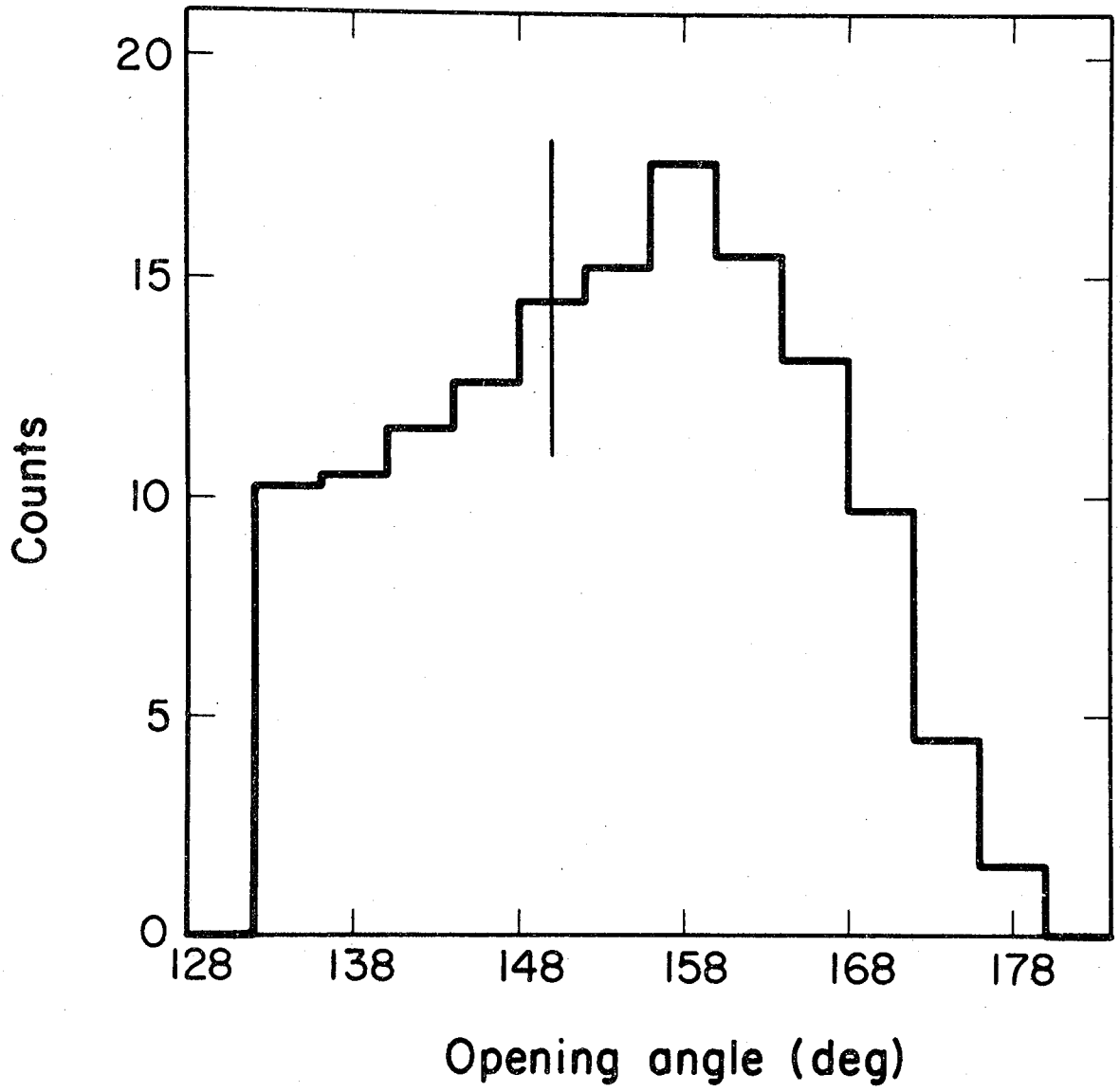
20
15
10
5
0
Counts
128
138
148
158
168
178
Opening angle (deg)
XBL 7612 - 11140

Fig. 15

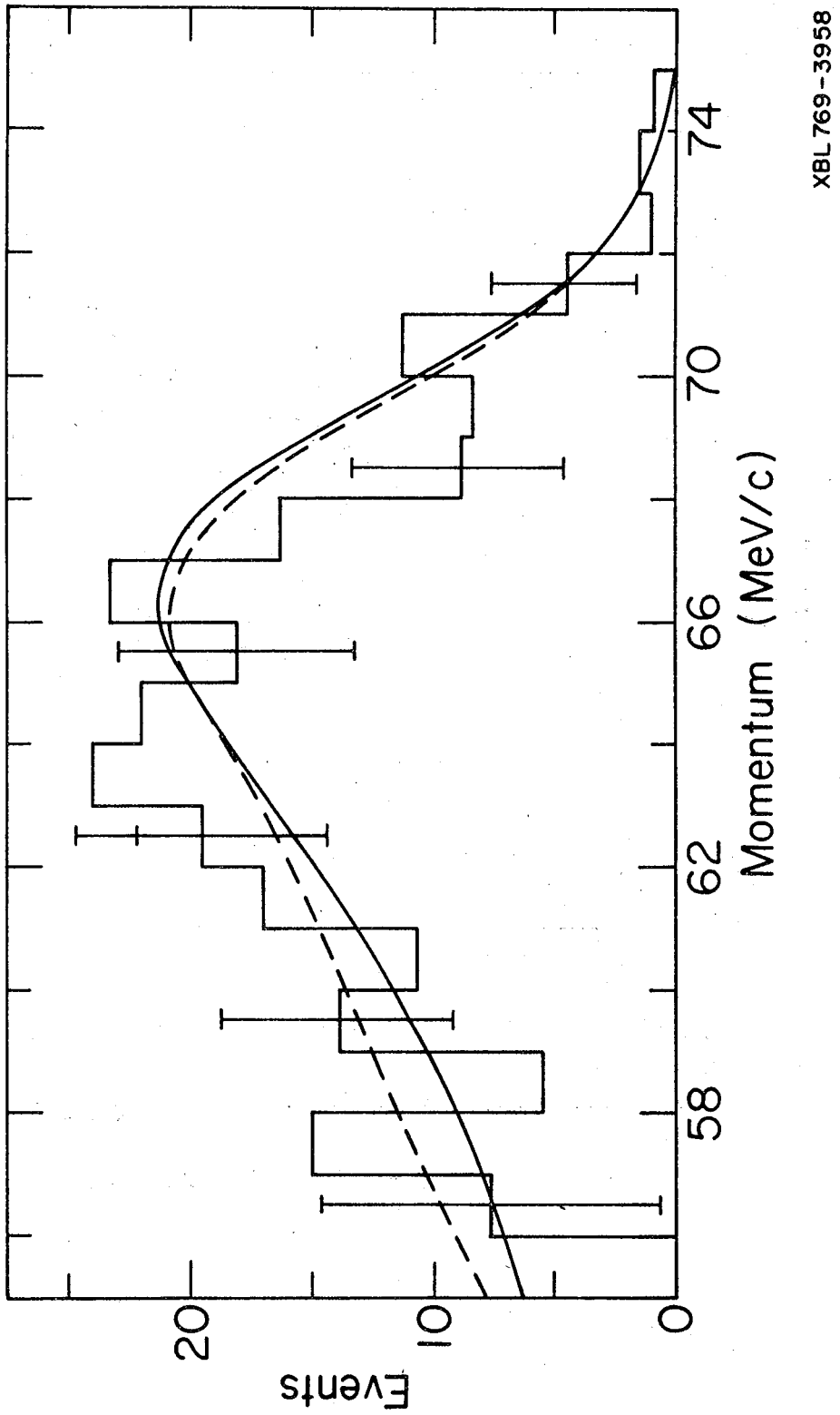

Fig. 16

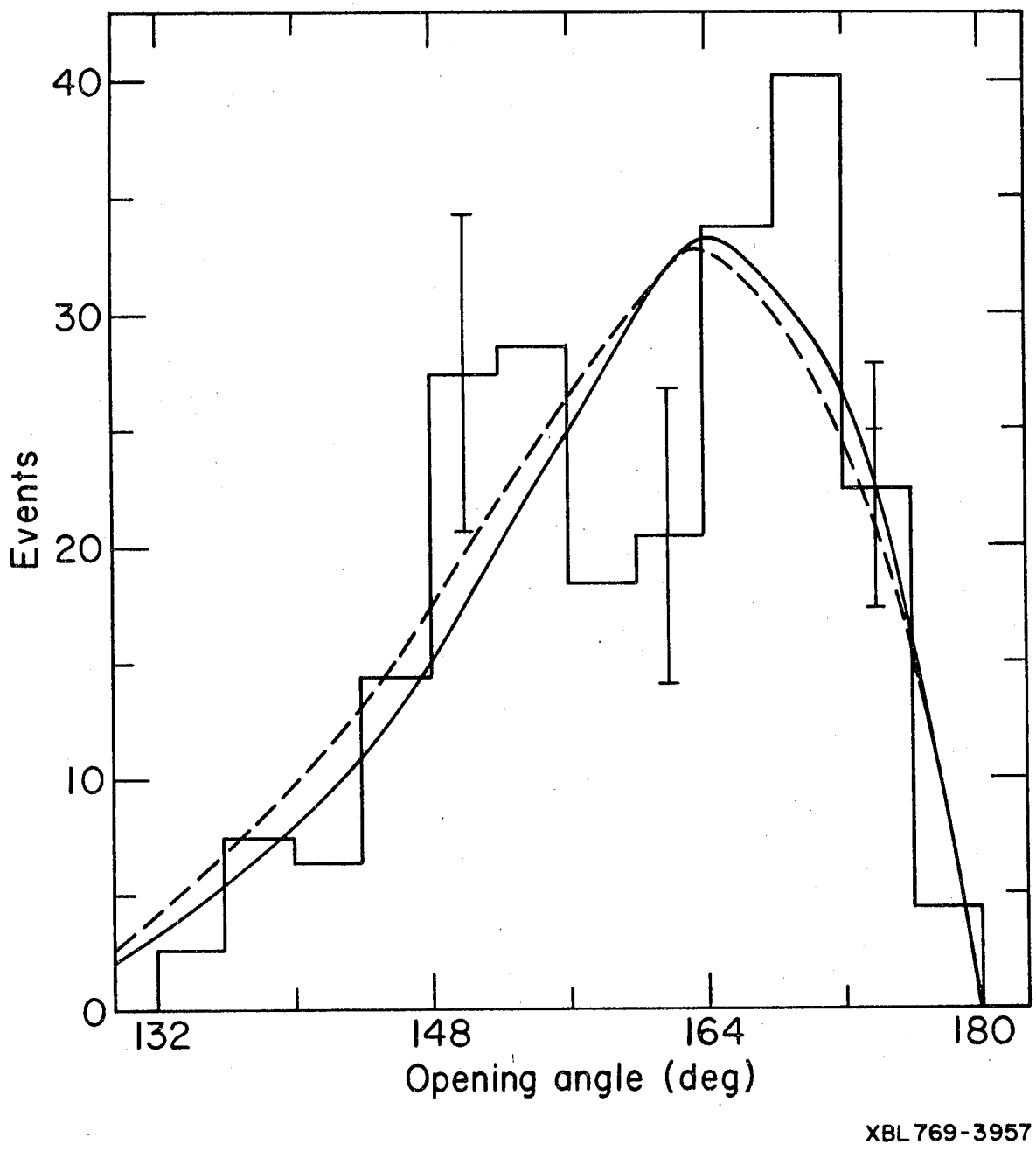
40
30
20
10
0
Events
132
148
164
180
Opening angle (deg)
XBL 769-3957

Fig. 17

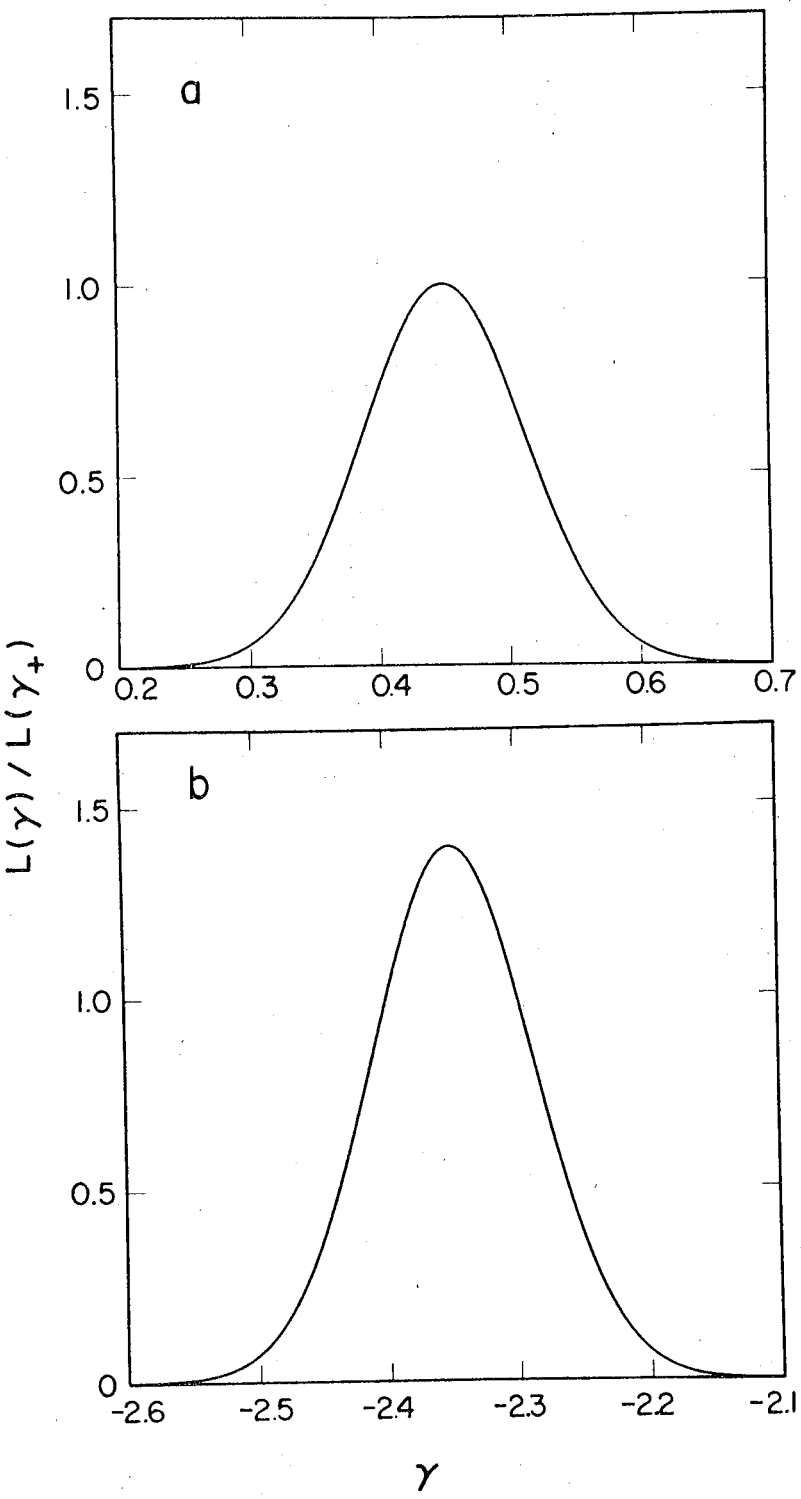

Fig. 18

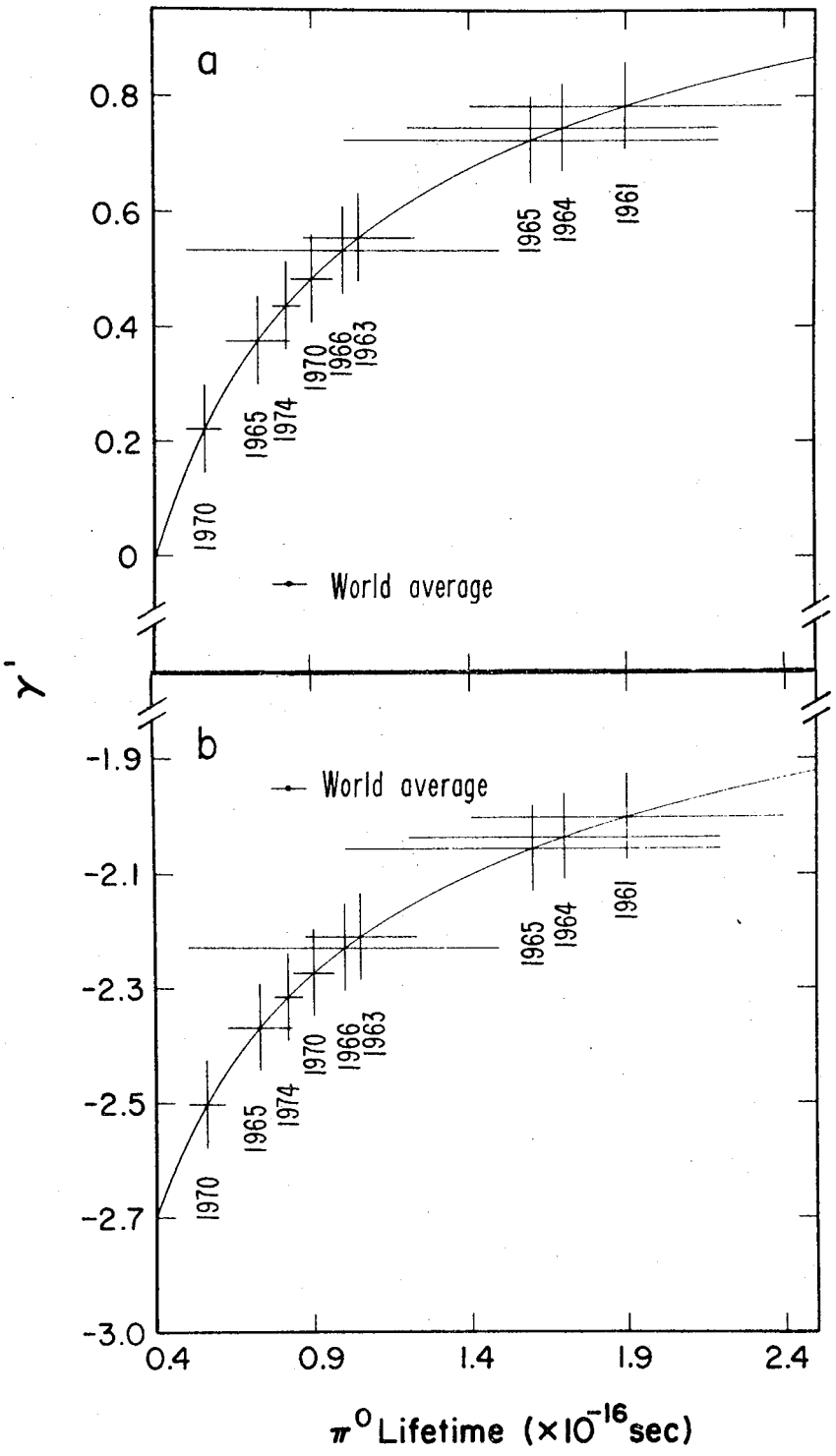
a
b
0.8
0.6
0.4
0.2
0
-1.9
-2.1
-2.3
-2.5
-2.7
-3.0
0.4
0.9
1.4
1.9
2.4
γ'
World average
World average
1970
1965
1974
1970
1966
1963
1965
1964
1961
π⁰ Lifetime (×10⁻¹⁶sec)
XBL 7612-11142

Fig. 19

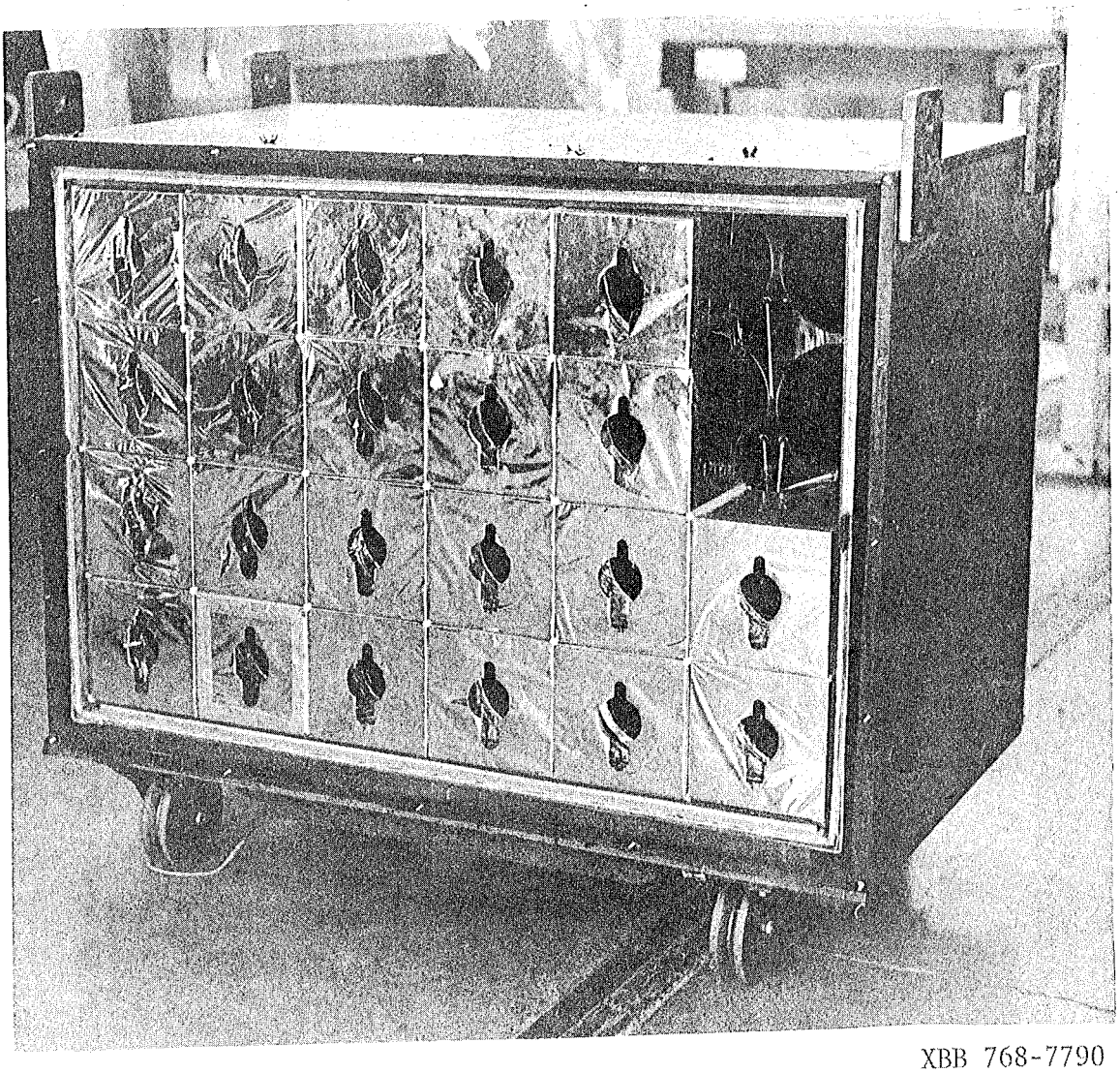

XBB 768-7790

Fig. 20

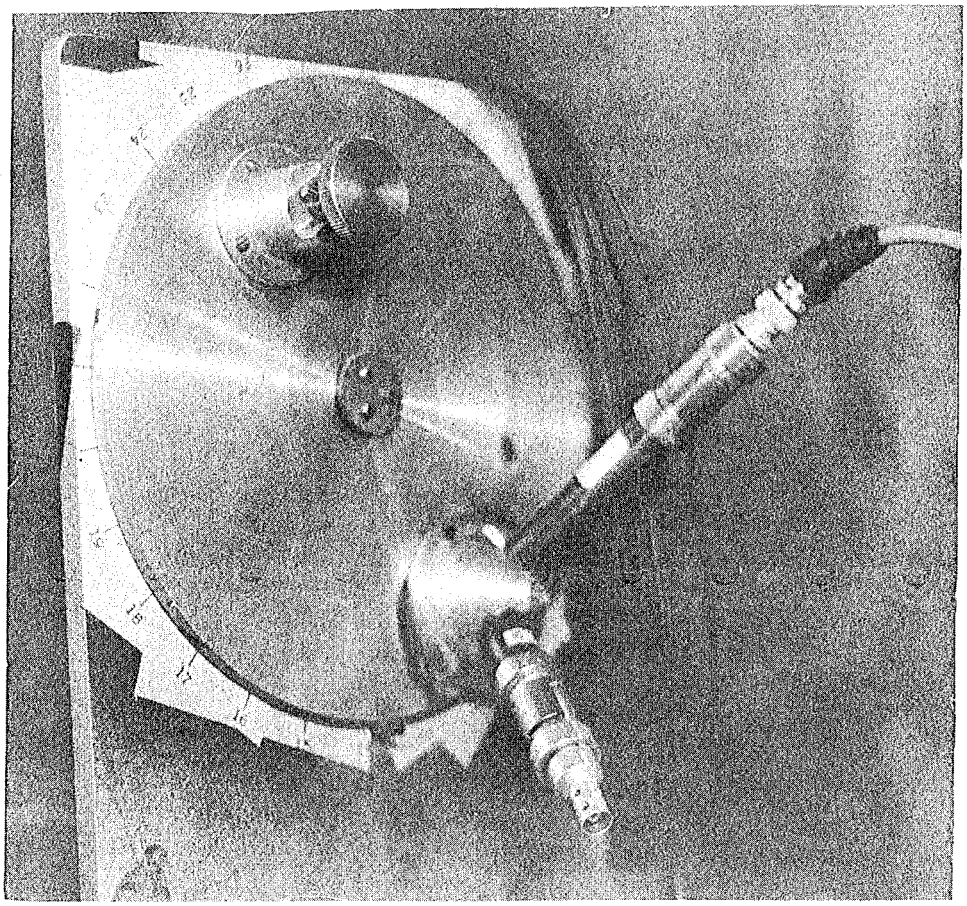

XBB 768-7789

Fig. 21

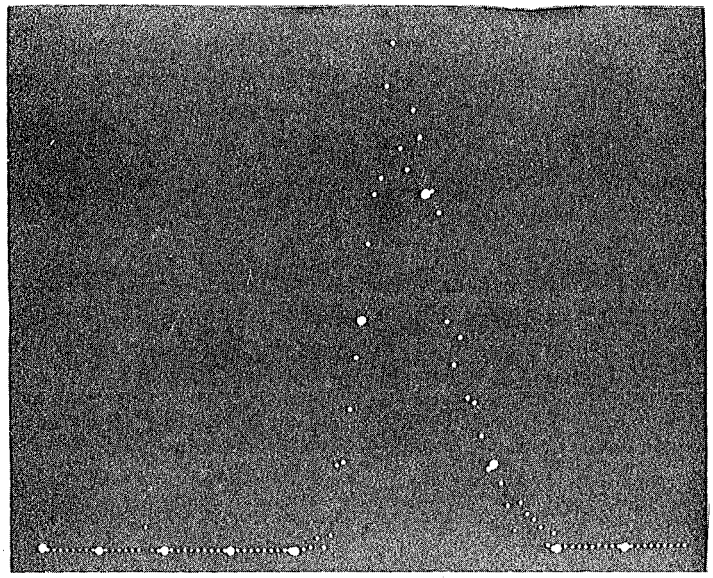

a

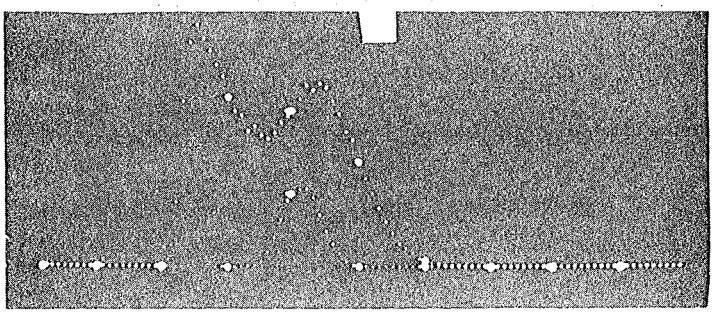

b

XBB 760-11118

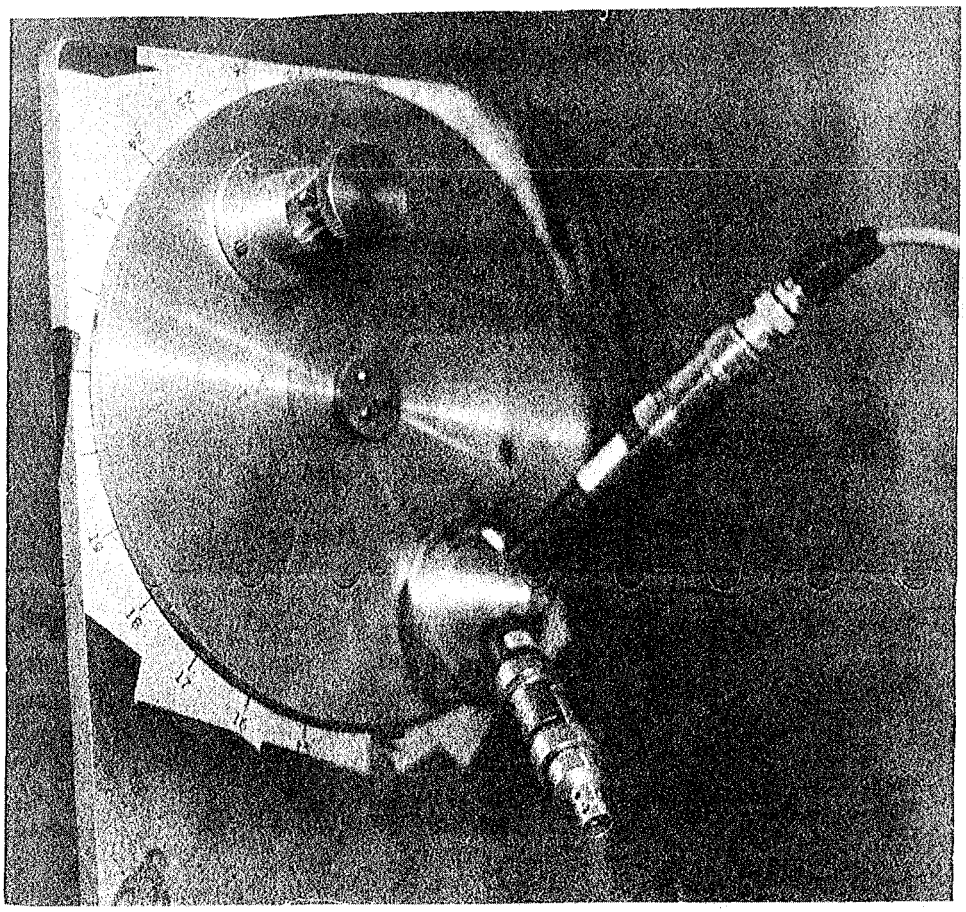

XBB 768-7789

Fig. 21

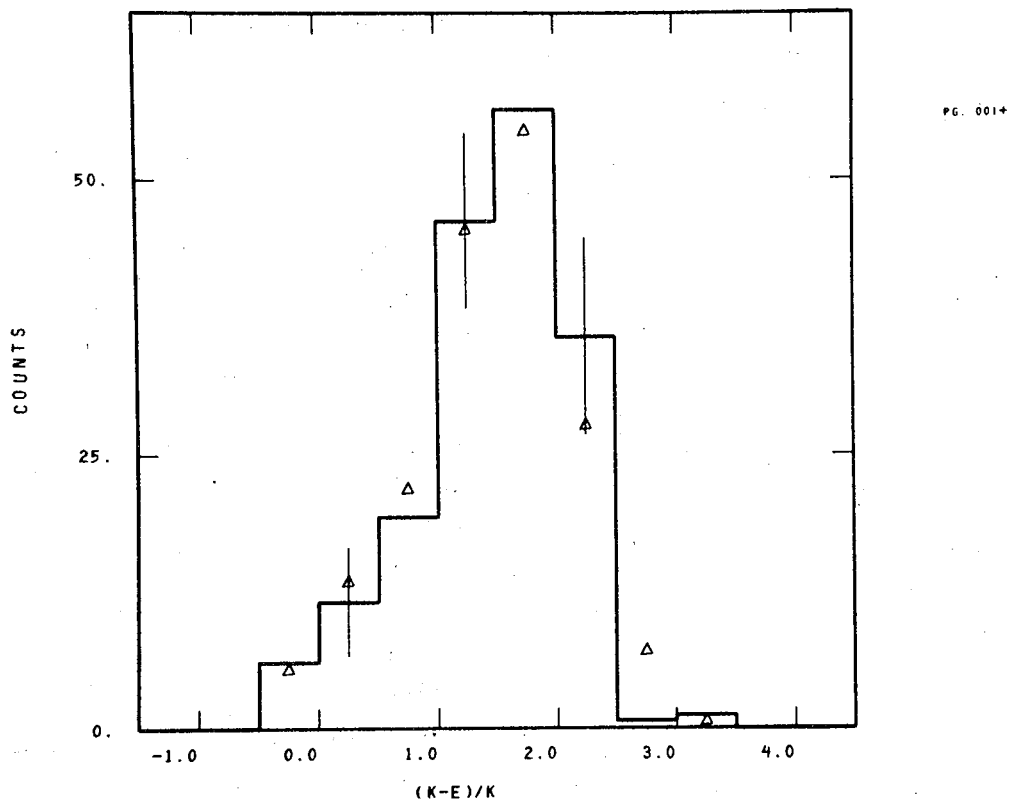

Fig. 24a

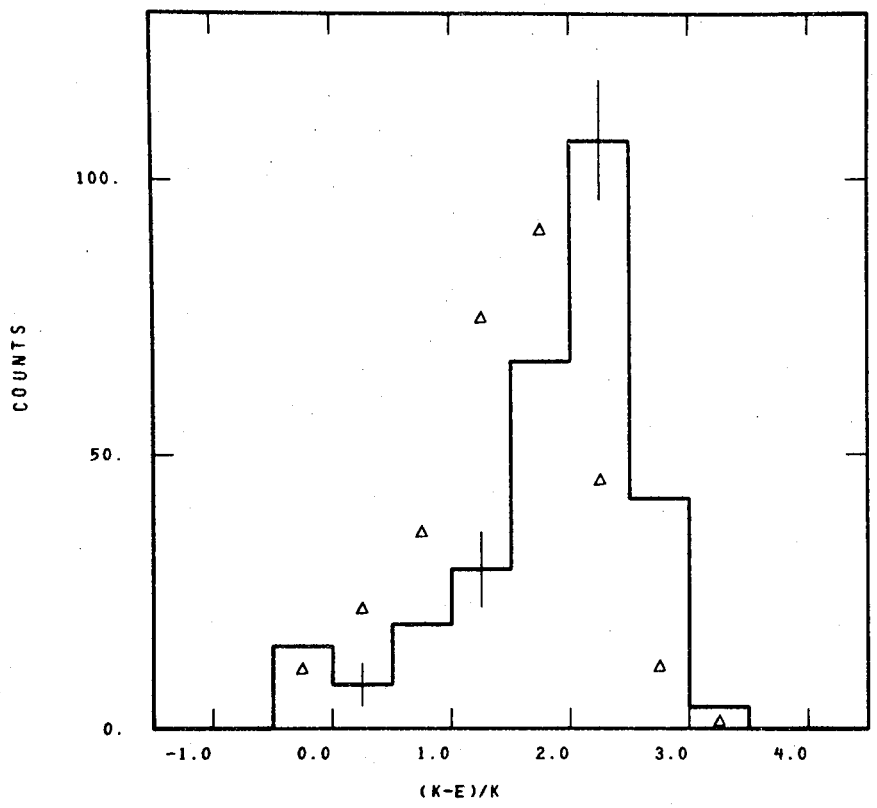

Fig. 24b

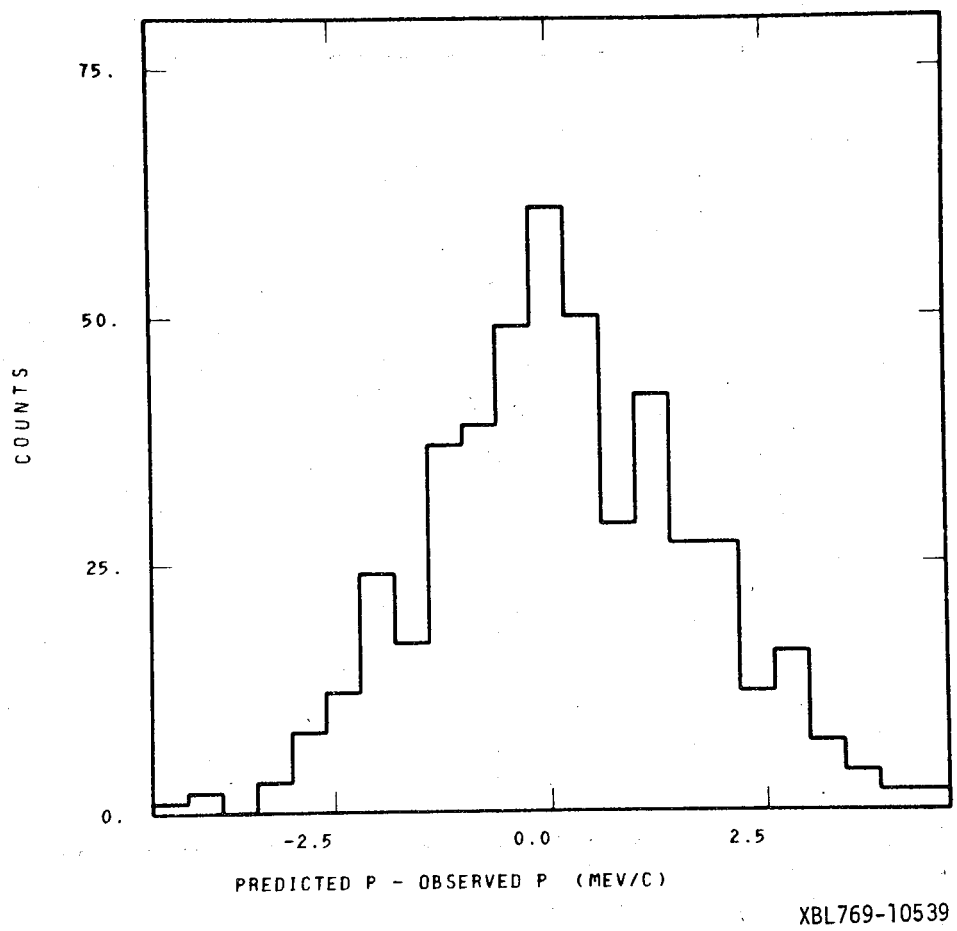

Fig. 25a

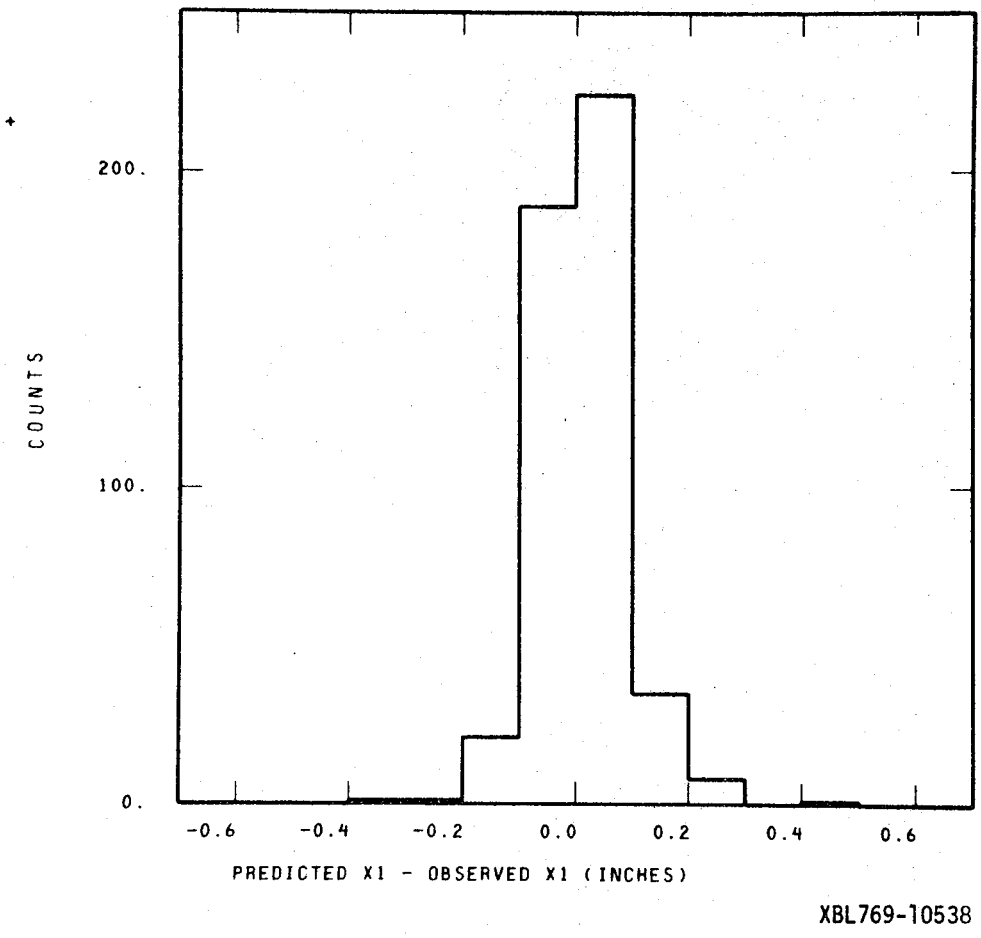
PG. 001+
200.
100.
0.
COUNTS
-0.6
-0.4
-0.2
0.0
0.2
0.4
0.6
PREDICTED X1 - OBSERVED X1 (INCHES)
XBL769-10538

Fig. 25b

This report was done with support from the United States Energy Research and Development Administration. Any conclusions or opinions expressed in this report represent solely those of the author(s) and not necessarily those of The Regents of the University of California, the Lawrence Berkeley Laboratory or the United States Energy Research and Development Administration.